

Thermal properties in mesoscopics: physics and applications from thermometry to refrigeration

Francesco Giazotto,^{1,2,*} Tero T. Heikkilä,^{1,3,†} Arttu Luukanen,^{4,5} Alexander M. Savin,¹ and Jukka P. Pekola¹

¹*Low Temperature Laboratory, Helsinki University of Technology, P.O. Box 2200, FIN-02015 HUT, Finland*

²*NEST-INFM and Scuola Normale Superiore, I-56126 Pisa, Italy*

³*Department of Physics and Astronomy, University of Basel, Klingelbergstr. 82, CH-4056 Basel, Switzerland*

⁴*National Institute of Standards and Technology, Quantum Electrical Metrology Division, 325 Broadway, Boulder CO 80305 USA*

⁵*Millimetre-wave Laboratory of Finland - MilliLab, VTT, P. O. Box 1000, FIN-02044 VTT, Finland*

(Dated: February 2, 2008)

This review presents an overview of the thermal properties of mesoscopic structures. The discussion is based on the concept of electron energy distribution, and, in particular, on controlling and probing it. The temperature of an electron gas is determined by this distribution: refrigeration is equivalent to narrowing it, and thermometry is probing its convolution with a function characterizing the measuring device. Temperature exists, strictly speaking, only in quasiequilibrium in which the distribution follows the Fermi-Dirac form. Interesting nonequilibrium deviations can occur due to slow relaxation rates of the electrons, e.g., among themselves or with lattice phonons. Observation and applications of nonequilibrium phenomena are also discussed. The focus in this paper is at low temperatures, primarily below 4 K, where physical phenomena on mesoscopic scales and hybrid combinations of various types of materials, e.g., superconductors, normal metals, insulators, and doped semiconductors, open up a rich variety of device concepts. This review starts with an introduction to theoretical concepts and experimental results on thermal properties of mesoscopic structures. Then thermometry and refrigeration are examined with an emphasis on experiments. An immediate application of solid-state refrigeration and thermometry is in ultra-sensitive radiation detection, which is discussed in depth. This review concludes with a summary of pertinent fabrication methods of presented devices.

Contents

I. Introduction	2	D. Thermometry based on the temperature dependent conductance of p	
II. Thermal properties of mesoscopic scale hybrid structures at sub-K temperatures		E. Anderson-insulator thin film thermometry	23
A. Boltzmann equation in a diffusive wire	3	IV. Thermal detectors and their characteristics	24
B. Boundary conditions	4	A. Effect of operating temperature on the performance of thermal detect	
C. Collision integrals for inelastic scattering	5	B. Bolometers: Continuous excitation	25
1. Electron-electron scattering	5	1. Hot electron bolometers	28
2. Electron-phonon scattering	6	2. Hot phonon bolometers	28
D. Quasiequilibrium limit	7	C. Calorimeters: Pulsed excitation	30
E. Observables	8	D. Future directions	31
1. Currents	8	V. Electronic refrigeration	32
2. Noise	9	A. General principles	32
F. Examples on different systems	10	B. Peltier refrigerators	32
1. Normal-metal wire between normal-metal reservoirs	10	C. Superconducting electron refrigerators	34
2. Superconducting tunnel structures	11	1. (SI)NIS structures	34
3. Superconductor-normal-metal structures with transparent contacts	12	2. S ₁ IS ₂ (IS ₁) structures	37
G. Heat transport by phonons	15	3. SSmS structures	39
H. Heat transport in a metallic reservoir	16	4. SF systems	39
III. Thermometry on mesoscopic scale	17	5. HT _c NIS systems	40
A. Hybrid junctions	18	6. Application of (SI)NIS structures to lattice refrigeration	41
1. NIS thermometer	18	7. Josephson transistors	42
2. SIS thermometer	19	D. Perspective types of refrigerators	44
3. Proximity effect thermometry	20	1. Thermionic refrigerators	44
B. Coulomb blockade thermometer, CBT	20	2. Application of low-dimensional systems to electronic refrigeration	46
C. Shot noise thermometer, SNT	22	VI. Device fabrication	46
		A. Structure typologies and material considerations	46
		B. Semiconductor growth techniques	46
		C. Thin-film metals deposition methods	47
		1. Thermal evaporation	47
		2. Sputter deposition	47
		D. Thin film insulators	48

*Electronic address: F.Giazotto@sns.it

†Electronic address: Tero.T.Heikkila@hut.fi

- E. Lithography and etching techniques
- F. Tunnel barriers
 1. Oxide barriers
 2. Schottky barriers

VII. Future prospects

Acknowledgments

References

I. INTRODUCTION

Solid state mesoscopic electronic systems provide a micro-laboratory to realize experiments on low temperature physics, to study quantum phenomena such as fundamental relaxation mechanisms in solids, and a way to create advanced cryogenic devices. In a broad sense, mesoscopic here refers to micro- and nanostructures, whose size falls in between atomic and macroscopic scales. The central concept of this Review is the energy distribution of mesoscopic electron systems, which in thermal equilibrium (Fermi-Dirac distribution) determines the temperature of the electron gas. The non-Fermi distributions are discussed in depth, since they are often encountered and utilized in mesoscopic structures and devices. This Review aims to discuss the progress mainly during the past decade on how electron distributions can be controlled, measured and made use of in various device concepts. When appropriate, earlier developments are reviewed as well. The central devices and concepts to be discussed are electronic refrigerators, thermometers, radiation detectors, and distribution-controlled transistors. Typically the working principles or resolution of these detectors rely on phenomena that show up only at cryogenic temperatures, i.e., at temperatures of the order of a few kelvin and below. A practical threshold in terms of temperature is set by liquefaction of helium at 4.2 K. This also sets the emphasis in this Review: the devices and principles working mostly at temperatures above 4.2 K are at times mentioned only for reference.

Section II of this Review introduces formally the central ingredients; the relevant theoretical results are either derived or given there. We also review some of the new developments concerning the thermoelectric effects in mesoscopic systems. Although the theoretical analysis of the effects in the later sections is based on Sec. II, the main messages can be understood without reading it in detail. Section III explains how the electronic temperature is typically measured and what is required of an electronic thermometer. Accurate and fast thermometers can be utilized for thermal radiation detection as explained in Sec. IV, which reviews such detectors. The resolution of these devices is ultimately limited by the thermal noise, which can be lowered by refrigeration. In Sec. V, we show how the electron temperature can be lowered via electronic means, and discuss the direct applications of this refrigeration. Section VI explains the

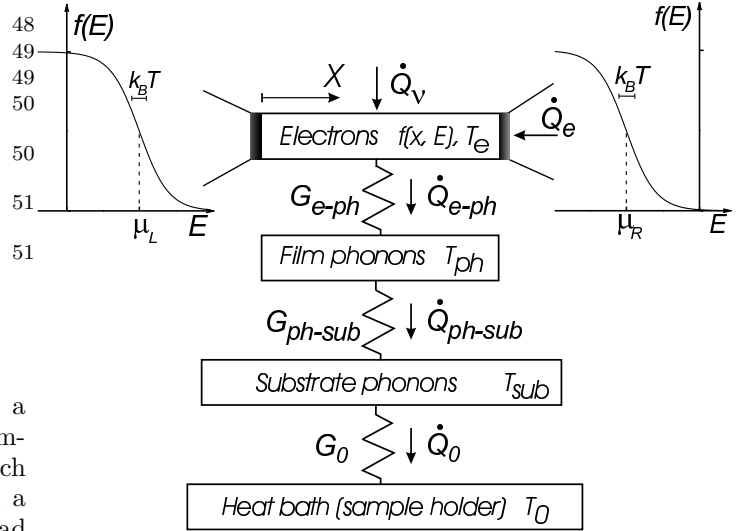


FIG. 1 Schematic picture of the system considered in this review. We describe an electron system in a diffusive wire, connected to two normal-metal or superconducting reservoirs via contacts of resistance R_N . The reservoirs are further connected to the macroscopic measurement apparatus (see Subs. II.H). The heat flows and thermal conductances between the studied electron system and the external driving, the electromagnetic environment, and the phonons in the lattice (Subs. II.C and II.D) are indicated with the arrows. The description of phonons in the lattice can further be divided in the film phonons, substrate phonons and finally the heat bath on which the substrate resides (Subs. II.G). If the system is used as a radiation detector, it also couples to the radiation field, typically via some matching circuit (Sec. IV).

main methods used in the fabrication of mesoscopic electronic devices, and in Sec. VII we briefly discuss some of the main open questions in the field and the prospects of practical instruments based on electronic refrigeration and using the peculiar out-of-equilibrium energy distributions.

II. THERMAL PROPERTIES OF MESOSCOPIC SCALE HYBRID STRUCTURES AT SUB-KELVIN TEMPERATURES

The schematic picture of a setup studied in typical experiments described in this Review is shown in Fig. 1. The main object is a diffusive metal or heavily-doped semiconductor wire connected to large electrodes acting as reservoirs where electrons thermalize quickly to the surroundings. The electrons in the wire interact between themselves, and are coupled to the phonons in the film and to the radiation and the fluctuations in the electromagnetic environment. The temperature T_{ph} of the film phonons can, in a non-equilibrium situation, differ from that of the substrate phonons, T_{sub} and this can even differ from the phonon temperature T_0 in the sample holder that is externally cooled. Under the applied voltage, the energy distribution function $f(E)$ of electrons depends

on each of these couplings, and on the state (e.g., superconducting or normal) of the various parts of the system. In certain cases detailed below, $f(E)$ is a Fermi function

$$f_{\text{eq}}(E; T_e, \mu) = \frac{1}{\exp[(E - \mu)/(k_B T_e)] + 1}, \quad (1)$$

characterized by an electron temperature T_e and potential μ . One of the main goals of this review is to explain how T_e , and in some cases also T_{ph} , can be driven even much below the lattice temperature T_0 , and how this low T_e can be exploited to improve the sensitivity of applications relying on the electronic degrees of freedom. We also detail some of the out-of-equilibrium effects, where $f(E)$ is not of the form of Eq. (1). In some setups, the specific form of $f(E)$ can be utilized for novel physical phenomena.

Throughout the Review, we concentrate on wires whose dimensions are large enough to fall in the quasi-classical diffusive limit. This means that the Fermi wavelength λ_F , elastic mean free path ℓ_{el} and the length of the wire L have to satisfy $\lambda_F \ll \ell_{el} \ll L$. In this regime, the electron energy distribution function is well defined, and its space dependence can be described by a diffusion equation (Eq. (3)). In most parts of the Review, we assume the capacitances C of the contacts large enough, such that the charging energy $E_C = e^2/2C$ is less than any of the relevant energy scales and can thus be ignored.

Our approach is to describe the electron energy distribution function $f(\mathbf{r}, E)$ at a given position \mathbf{r} of the sample and then relate this function to the charge and heat currents and their noise. In typical metal structures in the absence of superconductivity, phase-coherent effects are weak and often it is enough to rely on a semiclassical description. In this case, $f(\mathbf{r}, E)$ is described by a diffusion equation, as discussed in Subs. II.A. The electron reservoirs impose boundary conditions for the distribution functions, specified in Subs. II.B. The presence of inelastic scattering due to electron-electron interaction, phonons or the electromagnetic environment can be described by source and sink terms in the diffusion equation, specified by the collision integrals and discussed in Subs. II.C. In the limit when these scattering effects are strong, the distribution function tends to a Fermi function $f_{\text{eq}}(E; T_e(\mathbf{r}), \mu(\mathbf{r}))$ throughout the wire, with a position dependent potential $\mu(\mathbf{r})$ and temperature $T_e(\mathbf{r})$. In this quasiequilibrium case, detailed in Subs. II.D, it thus suffices to find these two quantities. Finally, with the knowledge of $f(\mathbf{r}; E)$, one can obtain the observable currents and their noise as described in Subs. II.E.

In many cases, it is not enough to only describe the electrons inside the mesoscopic wire, assuming that the surroundings are totally unaffected by the changes in this electron system. If the phonons in the film are not well coupled to a large phonon bath, their temperature is influenced by the coupling to the electrons. In this case, it is important to describe the phonon heating or cooling in detail (see Subs. II.G). Often also the electron reservoirs

may get heated due to an applied bias voltage, which has to be taken into account in the boundary conditions. This heating is discussed in Subs. II.H.

At the temperature range considered in this Review, many metals undergo a transition to the superconducting state (Tinkham, 1996). This gives rise to several new phenomena that can be exploited, for example, for thermometry (see Sec. III), for radiation detection (Sec. IV) and for electron cooling (Sec. V). The presence of superconductivity modifies both the diffusion equation (inside normal-metal wires through the proximity effect, see Subs. II.A) and especially the boundary conditions (Subs. II.B). Also the relations between the observable currents and the distribution functions are modified (Subs. II.E).

Once the basic equations for finding $f(\mathbf{r}, E)$ are outlined, we detail its behavior in different types of normal-metal – superconductor heterostructures in Subs. II.F.

A. Boltzmann equation in a diffusive wire

The semiclassical Boltzmann equation (Ashcroft and Mermin, 1976; Smith and Jensen, 1989) describes the average number of particles, $f(\mathbf{r}, \mathbf{p}) d\mathbf{r} d\mathbf{p} / (2\pi)^3$, in the element $\{d\mathbf{r}, d\mathbf{p}\}$ around the point $\{\mathbf{r}, \mathbf{p}\}$ in the six-dimensional position-momentum space. The kinetic equation for $f(\mathbf{r}, \mathbf{p})$ is a continuity equation for particle flow,

$$\left(\frac{\partial}{\partial t} + \mathbf{v} \cdot \partial_{\mathbf{r}} + e\mathbf{E} \cdot \partial_{\mathbf{p}} \right) f(\mathbf{r}, \mathbf{p}; t) = I_{\text{el}}[f] + I_{\text{in}}[f]. \quad (2)$$

Here \mathbf{E} is the electric field driving the charged particles and the elastic and inelastic collision integrals I_{el} and I_{in} , functionals of f , act as source and sink terms. They illustrate the fact that scattering breaks translation symmetries in space and time — the total particle numbers expressed through the momentum integrals of f still remain conserved.

In the metallic diffusive limit, Eq. (2) may be simplified as follows (Nagaev, 1992; Rammer, 1998; Sukhorukov and Loss, 1999). The electric field term can be absorbed in the space derivative by the substitution $E = \varepsilon_{\mathbf{p}} + \mu(\mathbf{r})$ in the argument of the distribution function, such that E describes both the kinetic $\varepsilon_{\mathbf{p}}$ and the potential energy μ of the electron. Therefore, we are only left with the full \mathbf{r} -dependent derivative $\mathbf{v} \cdot \nabla f = \mathbf{v} \cdot \partial_{\mathbf{r}} f + e\mathbf{E} \cdot \partial_{\mathbf{p}} f$ on the left-hand side of Eq. (2). In the diffusive regime, one may concentrate on length scales much larger than the mean free path ℓ_{el} . There, the particles quickly lose the memory of the direction of their initial momentum, and the distribution functions become nearly isotropic in the direction of \mathbf{v} . Therefore, we may expand the distribution function f in the two lowest spherical harmonics in the dependence on $\hat{\mathbf{v}} \equiv \mathbf{v}/v$, $f(\hat{\mathbf{v}}) = f_0 + \hat{\mathbf{v}} \cdot \delta f$, and make the relaxation-time approximation to the elastic collision integral with the elastic scattering time τ , i.e., $I_{\text{el}} = -\hat{\mathbf{v}} \cdot \delta f / \tau$. In

the limit where the time dependence of the distribution function takes place in a much slower scale than τ , this yields the diffusion equation with a source term,

$$(\partial_t - D\nabla_{\mathbf{r}}^2)f_0(\mathbf{r}; E, t) = I_{\text{in}}[f_0]. \quad (3)$$

Here we assume that the particles move with the Fermi velocity, i.e., $\mathbf{v} = v_F \hat{\mathbf{v}}$. As a result, their diffusive motion is characterized by the diffusion constant $D = v_F^2 \tau / 3$. In what follows, we will mainly concentrate on the static limit, i.e., assume $\partial_t f_0(\mathbf{r}; E, t) = 0$ and lift the subscript 0 from the angle-independent part f_0 of the distribution function.

Equation (3) can also be derived rigorously from the microscopic theory through the use of the quasiclassical Keldysh formalism (Rammer and Smith, 1986). With such an approach, one can also take into account superconducting effects, such as Andreev reflection (Andreev, 1964b) and the proximity effect (Belzig *et al.*, 1999). In the diffusive limit, one obtains the Usadel equation (Usadel, 1970), which in the static case is

$$\frac{D}{\sigma A} \nabla \cdot \tilde{I} = [-iE\tilde{\tau}_3 + \tilde{\Delta}(\mathbf{r}) + \tilde{\Sigma}_{\text{in}}(\mathbf{r}), \tilde{G}(\mathbf{r}; E)]. \quad (4)$$

Here $\tilde{G}(\mathbf{r}; E)$ is the isotropic part of the Keldysh Green's function in the Keldysh \otimes Nambu space, A and σ are the cross section and the normal-state conductivity of the wire, $\tilde{\tau}_3 = \hat{1} \otimes \hat{\tau}_3$ is the third Pauli matrix in Nambu space, $\tilde{\Delta} = \hat{1} \otimes \hat{\Delta}$ is the pair potential matrix, and $\tilde{\Sigma}_{\text{in}}$ describes the inelastic scattering that is not contained in $\tilde{\Delta}$. Usadel equation describes the matrix current $\tilde{I} = \sigma A \tilde{G} \nabla \tilde{G}$ (Nazarov, 1999), whose components integrated over the energy yield the physical currents. In the Keldysh space, \tilde{G} is of the form

$$\tilde{G} = \begin{pmatrix} \hat{G}^R & \hat{G}^K \\ 0 & \hat{G}^A \end{pmatrix},$$

where each component is a 2×2 matrix in Nambu particle-hole space. Equation (4) has to be augmented with a normalization condition $\tilde{G}^2 = 1$. This implies $(\hat{G}^{R/A})^2 = 1$ and allows a parametrization $\hat{G}^K = \hat{G}^R \hat{h} - \hat{h} \hat{G}^A$, where \hat{h} is a distribution function matrix with two free parameters. The equations for the retarded/advanced functions $\hat{G}^{R/A}$ ((1,1) and (2,2) - Keldysh components of Eq. (4)) describe the behavior of the pairing amplitude. The solutions to these equations yield the coefficients for the kinetic equations, i.e., the (1,2) or the Keldysh part of Eq. (4). This describes the symmetric and antisymmetric parts of the energy distribution function with respect to the chemical potential of the superconductors. The latter is assumed everywhere equal to allow a time-independent description. A common choice is a diagonal $\hat{h} = f^L + f^T \hat{\tau}_3$ (Schmid and Schön, 1975), where $f^L(E) = f(-E) - f(E)$ is the antisymmetric and $f^T(E) = 1 - f(E) - f(-E)$ the symmetric part of the energy distribution function $f(E)$. With this choice, inside the normal metals

where $\hat{\Delta} = 0$, we get two kinetic equations of the form (Belzig *et al.*, 1999; Virtanen and Heikkilä, 2004a)

$$D\nabla \cdot j^L = \Sigma_{\text{in}}^L, \quad j^L = \sigma A (\mathcal{D}_L \nabla f^L - \mathcal{T}^{\text{an}} \nabla f^T + j_S f^T), \quad (5a)$$

$$D\nabla \cdot j^T = \Sigma_{\text{in}}^T, \quad j^T = \sigma A (\mathcal{D}_T \nabla f^T + \mathcal{T}^{\text{an}} \nabla f^L + j_S f^L). \quad (5b)$$

Here $j^L \equiv \frac{1}{4} \text{Tr} [(\tau_1 \otimes \hat{1}) \tilde{I}]$ describes the spectral energy current, and $j^T \equiv \frac{1}{4} \text{Tr} [(\tau_1 \otimes \hat{\tau}_3) \tilde{I}]$ the spectral charge current. The inelastic effects are described by the collision integrals $\Sigma_{\text{in}}^L \equiv \frac{1}{4} \text{Tr} [(\tau_1 \otimes \hat{1}) [\tilde{\Sigma}_{\text{in}}, \tilde{G}]]$ and $\Sigma_{\text{in}}^T \equiv \frac{1}{4} \text{Tr} [(\tau_1 \otimes \hat{\tau}_3) [\tilde{\Sigma}_{\text{in}}, \tilde{G}]]$. The kinetic coefficients are

$$\begin{aligned} \mathcal{D}_L &\equiv \frac{1}{4} \text{Tr} [1 - \hat{G}^R \hat{G}^A] \\ \mathcal{D}_T &\equiv \frac{1}{4} \text{Tr} [1 - \hat{G}^R \hat{\tau}_3 \hat{G}^A \hat{\tau}_3] \\ \mathcal{T}^{\text{an}} &\equiv \frac{1}{4} \text{Tr} [\hat{G}^A \hat{G}^R \hat{\tau}_3] \\ j_S &\equiv \frac{1}{4} \text{Tr} [(\hat{G}^R \nabla \hat{G}^R - \hat{G}^A \nabla \hat{G}^A) \hat{\tau}_3]. \end{aligned}$$

Here, \mathcal{D}_L and \mathcal{D}_T are the spectral energy and charge diffusion coefficients, and j_S is the spectral density of the supercurrent-carrying states (Heikkilä *et al.*, 2002). The cross-term \mathcal{T}^{an} is usually small but not completely negligible. In a normal-metal wire in the absence of a proximity effect, $\hat{G}^R = \hat{\tau}_3$ and $\hat{G}^A = -\hat{\tau}_3$. Then we obtain $\mathcal{D}_L = \mathcal{D}_T = 1$, $\mathcal{T}^{\text{an}} = j_S = 0$ and the kinetic equations (5b) reduce to Eq. (3) in the static limit.

B. Boundary conditions

The quasiclassical kinetic equations cannot directly describe constrictions whose size is of the order of the Fermi wavelength, such as tunnel junctions or quantum point contacts. However, such contacts can be described by the boundary conditions derived by Nazarov (1999),

$$\tilde{I}_L = \tilde{I}_R = Z \left(\frac{1}{2} [\tilde{G}_L, \tilde{G}_R]_+ \right) [\tilde{G}_R, \tilde{G}_L]_-, \quad (6)$$

where

$$Z(x) = \frac{2e^2}{h} \sum_n \frac{\mathcal{T}_n}{2 + \mathcal{T}_n(x-1)}.$$

Here, $[\tilde{G}_L, \tilde{G}_R]_{\pm} \equiv \tilde{G}_L \tilde{G}_R \pm \tilde{G}_R \tilde{G}_L$, and $\tilde{I}_{L(R)}$ and $\tilde{G}_{L(R)}$ are the matrix current and the Green's function at the left (right) of the constriction, evaluated at the interface and flowing towards the right. The constriction is described by a set $\{\mathcal{T}_n\}$ of transmission eigenvalues through the function $Z(x)$. For large constrictions, it is typically enough to transform the sum over the eigenvalues to an integral over the transmission probabilities \mathcal{T} , weighted by their probability distribution $\rho(\mathcal{T})$. In the case of a tunnel barrier, $\mathcal{T}_n \ll 1$,

and thus $Z(x) = e^2 \sum_n \mathcal{T}_n / h \equiv G_N / 2$. For a ballistic contact $\mathcal{T}_n \equiv 1$ and $Z(x) = G_N / (x + 1)$. For other types of contacts, it is typically useful to find the observable for arbitrary \mathcal{T} and weight it with $\rho(\mathcal{T})$, e.g., $\rho(\mathcal{T}) = \hbar \pi G_N / [(2e^2) \mathcal{T} \sqrt{1 - \mathcal{T}}]$ for a diffusive contact (Nazarov, 1994), $\rho(\mathcal{T}) = \hbar G_N / [e^2 \mathcal{T}^{3/2} \sqrt{1 - \mathcal{T}}]$ for a dirty interface (Schep and Bauer, 1997) or $\rho(\mathcal{T}) = 2 \hbar G_N / [e^2 \sqrt{\mathcal{T}(1 - \mathcal{T})}]$ for a chaotic cavity (Baranger and Mello, 1994). This way, the observables can be related to the normal-state conductance G_N of the junction.

Equation (6) yields a boundary condition both for the "spectral" functions $\hat{G}^{R/A}$ and for the distribution functions. In the absence of superconductivity, we simply have $\hat{G}^{R/A} = \pm \hat{\tau}_3$, and the boundary condition for the distribution functions becomes independent of the type of the constriction,

$$j^{L/T} = G_N (f_R^{L/T} - f_L^{L/T}). \quad (7)$$

In this case, the two currents can be included in the same function by defining $j(\pm E) = (j^L(E) \pm j^T(E))/2$. This yields the spectral current through the constriction

$$j(E) = G_N (f_L(E) - f_R(E)), \quad (8)$$

where $f_{L/R}$ is the energy distribution function on the left/right side of the constriction.

Another interesting yet tractable case is the one where a superconducting reservoir (on the "left" of the junction) is connected to a normal metal (on the "right") and the proximity effect into the latter can be ignored. The latter is true, for example, if we are interested in the distribution function at energies far exceeding the Thouless energy of the normal-metal wire, or in the presence of strong depairing. In this case, the spectral energy and charge currents are

$$j^L = \frac{2e^2}{h} \sum_n \mathcal{T}_n M_L(\mathcal{T}_n) \theta(\bar{E}) (f_R^L - f_L^L) \quad (9a)$$

$$j^T = \frac{2e^2}{h} \sum_n \mathcal{T}_n [M_T^1(\mathcal{T}_n) \theta(-\bar{E}) + M_T^2(\mathcal{T}_n) \theta(\bar{E})] f_R^T. \quad (9b)$$

Here $\bar{E} = |E| - \Delta$ and $\theta(E)$ is the Heaviside step function, and the energy-dependent coefficients are

$$M_L(\mathcal{T}) = \frac{2((2 - \mathcal{T})|E|\Omega + \mathcal{T}\Omega^2)}{((2 - \mathcal{T})\Omega + \mathcal{T}|E|)^2} \quad (10a)$$

$$M_T^1(\mathcal{T}) = \frac{2\mathcal{T}\Delta^2}{4(\mathcal{T} - 1)E^2 + (\mathcal{T} - 2)^2\Delta^2} \quad (10b)$$

$$M_T^2(\mathcal{T}) = \frac{2|E|}{(2 - \mathcal{T})\Omega + \mathcal{T}|E|} \quad (10c)$$

Here we defined $\Omega \equiv \sqrt{E^2 - \Delta^2}$. In the tunneling limit $\mathcal{T} \ll 1$, we get

$$j^{L/T} = G_N N_S(E) (f_R^{L/T} - f_L^{L/T}), \quad (11)$$

where

$$N_S(E) = \left| \text{Re} \left[\frac{E + i\Gamma}{\sqrt{(E + i\Gamma)^2 - \Delta^2}} \right] \right| \xrightarrow{\Gamma \rightarrow 0} \theta(\bar{E}) |E| / \Omega \quad (12)$$

is the reduced superconducting density of states (DOS). The first form of Eq. (12) assumes a finite pair-breaking rate Γ , which turns out to be relevant in some cases discussed in Sec. V.C.1 Unless specified otherwise, we assume that the superconductors are of the conventional weak-coupling type and the superconducting energy gap Δ at $T = 0$ is related to the critical temperature T_c by $\Delta \approx 1.764 k_B T_c$ (Tinkham, 1996).

C. Collision integrals for inelastic scattering

The collision integral I_{in} in Eq. (3) is due to electron-electron, electron-phonon interaction and the interaction with the photons in the electromagnetic environment.

1. Electron-electron scattering

For the electron-electron interaction, the collision integral is of the form

$$\mathcal{I}_{\text{coll}}^{e-e} = \kappa_{e-e}^{(d)} \int d\omega dE' \omega^\alpha \left(\tilde{f}_{\text{coll}}^{\text{in}}(\omega, E, E') - \tilde{f}_{\text{coll}}^{\text{out}}(\omega, E, E') \right), \quad (13)$$

where α and $\kappa_{e-e}^{(d)}$ depend on the type of scattering and the "in" and "out" collisions are

$$\tilde{f}_{\text{coll}}^{\text{in}} = [1 - f(E)][1 - f(E')] f(E - \hbar\omega) f(E' + \hbar\omega) \quad (14a)$$

$$\tilde{f}_{\text{coll}}^{\text{out}} = f(E) f(E') [1 - f(E - \hbar\omega)] [1 - f(E' + \hbar\omega)]. \quad (14b)$$

Electron-electron scattering can be either due to the direct Coulomb interaction (Altshuler and Aronov, 1985), or mediated through magnetic impurities which can flip their spin in a scattering process (Kaminski and Glazman, 2001) or other types of impurities with internal dynamics. In practice, both of these effects contribute to the energy relaxation (Anthore *et al.*, 2003; Pierre *et al.*, 2000). Assuming the electron-electron interaction is local on the scale of the variations in the distribution function, the direct interaction yields (Altshuler and Aronov, 1985) Eq. (13) with $\alpha = -2 + d/2$ for a d -dimensional wire. In a diffusive wire, the effective dimensionality of the wire is determined by comparing the dimensions to the energy-dependent length $L_E \equiv \sqrt{\hbar D / E}$. The prefactor $\kappa_{e-e}^{(d)}$ for a d -dimensional

sample is

$$\kappa_{e-e}^{(1)} = \frac{1}{\pi\sqrt{2D}\hbar^2\nu_F A}, \quad (\text{Huard } et al., 2004) \quad (15a)$$

$$\kappa_{e-e}^{(2)} = \frac{1}{8E_F\tau}, \quad (\text{Rammer and Smith, 1986}) \quad (15b)$$

$$\kappa_{e-e}^{(3)} = \frac{1}{8\pi^2\sqrt{2}\hbar^2\nu_F D^{3/2}}, \quad (\text{Rammer, 1998}) \quad (15c)$$

where $\nu_F = \nu(E_F)$ is the density of states at the Fermi energy E_F and A is the wire cross-section.

In the case of relaxation due to magnetic impurities, one expects (Kaminski and Glazman, 2001) $\alpha = -2$ and $\kappa_{e-e} = \frac{\pi}{2} \frac{c_m}{\hbar\nu_F} S(S+1) \left[\ln \left(\frac{eV}{k_B T_K} \right) \right]^{-4}$. Here c_m is the concentration, S is the spin, and T_K is the Kondo temperature of the magnetic impurities responsible for the scattering. This form is valid for $T > T_K$. For a more detailed account of the magnetic-impurity effects, see (Göppert *et al.*, 2002; Göppert and Grabert, 2001, 2003; Kroha and Zawadowski, 2002; Ujsaghy *et al.*, 2004) and the references therein.

For $d = 3$, and for small deviations δf from equilibrium, the collision integral can be approximated (Rammer, 1998) by $-\delta f/\tau_{e-e}$, where $\tau_{e-e} = 3\sqrt{3}\pi(\sqrt{8}-1)\zeta(3/2)(k_B T)^{3/2}/(16k_F\ell_{el}\sqrt{\hbar\tau}E_F)$ is the relaxation time ($\zeta(3/2) \approx 2.612$), $\tau = \ell_{el}/v_F$ is the elastic scattering time and k_F is the Fermi momentum. In the case when $\alpha < -1/2$, the usual relaxation-time approach does not work for the electron-electron interaction as the expression for the relaxation time has an infrared divergence (Altshuler and Aronov, 1985; Rammer, 1998). Therefore, one has to solve the full Boltzmann equation with the proper collision integrals. To obtain an estimate for the length scale at which the electron-electron interaction is effective, we can proceed differently. Introducing dimensionless position $\tilde{x} \equiv x/L$ and energy variables $\tilde{E}' \equiv E'/E^*$ and $\tilde{\omega} \equiv \hbar\omega/E^*$, we get

$$\partial_{\tilde{x}}^2 f = -K_{e-e} \tilde{I}_{\text{coll}}.$$

Here the dimensionless integral \tilde{I}_{coll} characterizes the deviation in the shape of the distribution function from the Fermi function and K_{e-e} depends on the specific system. For a quasi-1d wire with bare Coulomb interaction,

$$K_{e-e} = \frac{1}{\sqrt{2}} \frac{R_D}{R_K} \sqrt{\frac{E^*}{E_T}}, \quad (16)$$

where $R_K = h/(2e^2)$, $R_D = L/(\sigma A)$ is the resistance of the wire and $E_T = \hbar D/L^2$ is the Thouless energy. In the case when the wire terminates in a point contact with resistance R_T , the resistance R_D in Eq. (16) should be replaced with the total resistance $R_D + R_T$ (Pekola *et al.*, 2004a). Typically the energy scale characterizing the deviation from (quasi)equilibrium is $E^* = eV$. At $eV \gg k_B T$, electron-electron collisions start to be ef-

fective when $K_{e-e} \approx 1$. This yields a length scale

$$\ell_{e-e}^* = \sqrt{R_K A \sigma \sqrt{\frac{2\hbar D}{eV}}}, \quad (17)$$

where A is the cross section of the wire and σ its conductivity. Using a wire with resistance $R_D = 10 \Omega$ and $E_T \approx 10 \mu\text{eV}$ for $L = 1 \mu\text{m}$ (close to the values in (Huard *et al.*, 2004)), and a voltage $V = 100 \mu\text{V}$, we get $\ell_{e-e}^* \approx 24 \mu\text{m}$. Increasing the temperature, \tilde{I}_{coll} becomes smaller, and this effective length also decreases. The experimental results of Huard *et al.* (2004) indicate at least an order of magnitude larger κ_{e-e} and thus smaller ℓ_{e-e}^* than predicted by this theory. At present, the reasons for this discrepancy have not been found.

2. Electron-phonon scattering

Another source of inelastic scattering is due to phonons, for which the collision integral is of the form (Rammer, 1998; Wellstood *et al.*, 1994)

$$\mathcal{I}_{\text{coll}}^{e-\text{ph}} = 2\pi \int_0^\infty d\omega \alpha^2 F(\omega) \left[\tilde{I}_{\text{coll}}^{\text{in}}(E, \omega) - \tilde{I}_{\text{coll}}^{\text{out}}(E, \omega) \right]. \quad (18)$$

Here

$$\begin{aligned} \tilde{I}_{\text{coll}}^{\text{in}}(E, \omega) &= f(E + \hbar\omega)[1 - f(E)][1 + n_{\text{ph}}(\omega)] \\ &\quad + [1 - f(E)]f(E - \hbar\omega)n_{\text{ph}}(\omega) \\ \tilde{I}_{\text{coll}}^{\text{out}}(E, \omega) &= f(E)[1 - f(E - \hbar\omega)][1 + n_{\text{ph}}(\omega)] \\ &\quad + f(E)[1 - f(E + \hbar\omega)]n_{\text{ph}}(\omega). \end{aligned} \quad (19)$$

The kernel $\alpha^2 F(\omega)$ (the *Eliashberg function*) of the interaction depends on the type of considered phonons (longitudinal or transverse), on the relation between the phonon wavelength λ_{ph} and the electron mean free path ℓ_{el} , on the dimensionality of the electron and phonon system (Sergeev *et al.*, 2005), and on the characteristics of the Fermi surface (Pruunila *et al.*, 2005). At sub-kelvin temperatures and low voltages, the optical phonons can be neglected, and one can only concentrate on the acoustic phonons. In what follows, we also neglect phonon quantization effects which may be important in restricted geometries. Moreover, the phonon distribution function $n_{\text{ph}}(\omega)$ is considered to be in (quasi)equilibrium, i.e., described by a Bose distribution function $n_{\text{ph}}(\omega) = n_{\text{eq}}(\omega) \equiv [\exp(\hbar\omega/(k_B T)) - 1]^{-1}$ (for phonon relaxation processes, see Subs. II.G).

When the phonon temperature T_{ph} is much lower than the Debye temperature T_D , the phonon dispersion relation is linear and one can estimate the phonon wavelength using $\lambda_{\text{ph}} = \hbar v_S/k_B T_{\text{ph}}$. For typical metals, the speed of sound is $v_S \sim 3 \dots 5 \text{ km/s}$, which yields a wavelength $\lambda_{\text{ph}} \sim 100 \dots 200 \text{ nm}$ at $T_{\text{ph}} = 1 \text{ K}$ and $\lambda_{\text{ph}} \sim 1 \dots 2 \mu\text{m}$ at $T_{\text{ph}} = 100 \text{ mK}$. In the clean limit $\lambda_{\text{ph}} \ll \ell_{el}$, approximating the electron-phonon coupling with a scalar deformation potential, only the longitudinal phonons are coupled to the electrons. In this case for $\omega \ll k_B T_D/\hbar, k_F v_S$

	T_e (mK)	T_{ph} (mK)	Σ ($\text{W m}^{-3}\text{K}^{-5}$)	Measured in
Ag	50...400	50...400	$0.5 \cdot 10^9$	(Steinbach <i>et al.</i> , 1996)
Al	35...130	35	$0.2 \cdot 10^9$	(Kautz <i>et al.</i> , 1993)
	200...300	200	$0.3 \cdot 10^9$	(Meschke <i>et al.</i> , 2004)
Au	80...1200	80...1000	$2.4 \cdot 10^9$	(Echternach <i>et al.</i> , 1992)
AuCu	50...120	20...120	$2.4 \cdot 10^9$	(Wellstood <i>et al.</i> , 1989)
Cu	25...800	25...320	$2.0 \cdot 10^9$	(Roukes <i>et al.</i> , 1985)
	100...500	280...400	$0.9...4 \cdot 10^9$	(Leivo <i>et al.</i> , 1996)
	50...200	50...150	$2.0 \cdot 10^9$	(Meschke <i>et al.</i> , 2004)
Mo	980	80...980	$0.9 \cdot 10^9$	(Savin and Pekola, 2005)
$n^{++}\text{Si}$	120...400	175...400	$0.1 \cdot 10^9$	(Savin <i>et al.</i> , 2001)
	173...450	173	$0.04 \cdot 10^9$	(Prunnila <i>et al.</i> , 2002)
	320...410	320...410	$0.1 \cdot 10^9$	(Buonomo <i>et al.</i> , 2003)
Ti	300...800	500...800	$1.3 \cdot 10^9$	(Manninen <i>et al.</i> , 1999)

TABLE I Measured electron-phonon coupling constant Σ for different materials. The second and third columns indicate the temperature ranges (electron and phonon temperatures, respectively) of the measurements.

(Rammer, 1998; Wellstood *et al.*, 1994)

$$\alpha^2 F(\omega) = \frac{|M|^2}{4\pi^2 \hbar^2 v_S^3 \nu_F} \omega^2, \quad (20)$$

where $|M|^2$ is the square of the matrix element for the deformation potential. Generally this is inversely proportional to the mass density of the ions, but its precise microscopic form depends on the details of the lattice structure. Therefore it is useful to present $|M|$ in terms of a separately measurable quantity, e.g., the prefactor Σ of the power $P = \Sigma V T^5$ dissipated to the lattice of volume V in the quasiequilibrium limit (see Table I and Subs. II.D): $|M|^2 = \pi \hbar^5 v_S^3 \Sigma / (12 \zeta(5) k_B^5)$, where $\zeta(5) \approx 1.0369$.

In the dirty limit $\lambda_{ph} \gg \ell_{el}$, the power of ω in the Eliashberg function can be either 1 or 3, for the cases of static or vibrating disorder, respectively. For further details about the dirty limit, we refer to (Belitz, 1987; Rammer and Schmid, 1986; Sergeev and Mitin, 2000).

The relaxation rate for electron-phonon scattering is given by $1/\tau_{e-ph} = -\{\delta I_{e-ph}[f(E)]/\delta f(E)\}|_{f(E)=f_{eq}(E)}$, where $f_{eq}(E)$ now is a Fermi function at the lattice temperature. With this definition at $E = E_F$, (Rammer, 1998)

$$\frac{1}{\tau_{e-ph}} = 4\pi \int_0^\infty d\omega \frac{\alpha^2 F(\omega)}{\sinh\left(\frac{\hbar\omega}{k_B T}\right)}. \quad (21)$$

Thus, in the clean case for $k_B T \ll 2\hbar k_F v_S$ we obtain $1/\tau_{e-ph} = \alpha T^3$, $\alpha = 7\zeta(3)\Sigma/(24\zeta(5)k_B^2 \nu_F) \approx 0.34\Sigma/(k_B^2 \nu_F)$. With typical values for Cu, $\Sigma = 2 \cdot 10^9 \text{ WK}^{-5}\text{m}^{-3}$ and $\nu_F = 1.6 \cdot 10^{47} \text{ J}^{-1}\text{m}^{-3}$, we get $\tau_{e-ph} = 45$

ns at $T = 1 \text{ K}$. Assuming $\lambda_F \ll \ell_{el} \ll \ell_{e-ph}$, the electron-phonon scattering length is $\ell_{e-ph} = \sqrt{D\tau_{e-ph}}$. For the above values and a typical diffusion constant $D = 0.01 \text{ m}^2/\text{s}$, $\ell_{e-ph} \approx 21 \mu\text{m}$ at $T = 1 \text{ K}$ and $\ell_{e-ph} \approx 670 \mu\text{m}$ at $T = 100 \text{ mK}$.

In the disordered limit $\lambda_{ph} \gg \ell_{el}$, the temperature dependence of the electron-phonon scattering rate is expected to follow either the T^2 or T^4 laws, depending on the nature of the disorder (Sergeev and Mitin, 2000).

It seems that although most of the experiments are done in the limit where the phonon wavelength at least slightly exceeds the electron mean free path, in majority of the cases the results have fitted to the clean-limit expressions, i.e., the scattering rate $\propto T_e^3$ and the heat current flowing into the phonon system $\propto T_e^5$, see Eq. (24) below (for an exception, see (Karvonen *et al.*, 2005)). Finding the correct exponent is not straightforward, as the film phonons are also typically affected by the measurement, and because of the reduced dimensionality of the phonon system (see Subs. II.G). In this Review, we concentrate on the clean-limit expressions.

D. Quasiequilibrium limit

The shape of the distribution function at a given position of the wire strongly depends on how the inelastic scattering length l_{in} compares to the length L of the wire. For $L \ll l_{in}$ (*nonequilibrium limit*), we may neglect the inelastic scattering altogether. In this case, the distribution function is a solution to either Eqs. (5) or Eq. (3), where the collision integrals/self energies for inelastic scattering can be neglected. As a result, the shape of the electron distribution functions inside the wire at a finite bias voltage $eV \gtrsim k_B T$ may strongly deviate from a Fermi distribution (Giazotto *et al.*, 2004b; Heikkilä *et al.*, 2003; Heslinga and Klapwijk, 1993; Pekola *et al.*, 2004a; Pierre *et al.*, 2001; Pothier *et al.*, 1997b). The nonequilibrium shape shows up in most of the observable properties of the system, including the $I - V$ characteristics, the current noise or the supercurrent. In general, it can only be neglected in the $I - V$ characteristics if the charge transport process is energy independent as in the case of purely normal-metal samples. Even in this case the form of $f(E)$ can be observed in the current noise.

The kinetic equations can be greatly simplified in the limit where l_{in} for one type of scattering is much smaller than L . In the *quasiequilibrium* limit, the energy relaxation length due to electron-electron scattering is much shorter than the wire, $\ell_{e-e} \ll L$ (Nagaev, 1995). In this case, the local distribution function is a Fermi function characterized by the temperature $T_e(\mathbf{r}, t)$ and potential $\mu(\mathbf{r}, t)$. Mathematically, this can be seen by considering the Boltzmann equation (3) with the electron-electron collision integral, Eq. (13) in the limit where the prefactor of the latter becomes very large. As the left-hand side of Eq. (3) is not strongly dependent on the form of

$f(E, \mathbf{r})$ as a function of energy, the equation can only be satisfied if the collision integral without the prefactor becomes small. It can be easily shown that the latter vanishes for $f(E) = f_{\text{eq}}(E)$. Thus, the deviations from the Fermi-function shape will be at most of the order of l_{in}/L , and can be neglected in the quasiequilibrium limit.

In this limit, we are still left with two unknowns, $T_e(\mathbf{r}, t)$ and $\mu(\mathbf{r}, t)$. Substituting $f(E, \mathbf{r}) = f_{\text{eq}}(E; T_e(\mathbf{r}, t), \mu(\mathbf{r}, t))$ in Eq. (3) yields

$$(\partial_t - D\nabla^2)f = (\partial_t - D\nabla^2)(T_e \partial_{T_e} f + \mu \partial_{\mu} f) - D[(\nabla\mu)^2 \partial_{\mu}^2 f + (\nabla T_e)^2 \partial_{T_e}^2 f + 2\nabla T_e \nabla \mu \partial_{T_e} \partial_{\mu} f] = I_{\text{coll}}[f],$$

where $I_{\text{coll}}[f]$ contains the other types of inelastic scatterings, e.g., those with the phonons. In the right hand side of the upper line, the differential operators ∂_t and ∇ act only on T_e and μ . Integrating this over the energy and multiplying by $\nu_F E$ and then integrating over E yields

$$(\partial_t - D\nabla^2)\mu(\mathbf{r}) = 0, \quad (22)$$

$$C_e(\mathbf{r}, t) \partial_t T_e - \nabla(\kappa(\mathbf{r}, t) \nabla T_e) - \sigma(\nabla\mu/e)^2 = \tilde{I}_{\text{coll}}. \quad (23)$$

We assumed that the energy integral over $I_{\text{coll}}[f]$ vanishes.¹ Here $C_e(\mathbf{r}, t) = \pi^2 \nu_F k_B^2 T_e(\mathbf{r}, t)/3$ is the electron heat capacity, $\sigma = D\nu_F e^2$ is the Drude conductivity, $\kappa(\mathbf{r}, t) = \sigma L_0 T_e(\mathbf{r}, t)$ is the electron heat conductivity, $L_0 = \pi^2 k_B^2 / (3e^2) \approx 2.45 \cdot 10^{-8} \text{ W}\Omega\text{K}^{-2}$ is the Lorenz number and $\tilde{I}_{\text{coll}}(T_e, \mu)$ contains the power per unit volume emitted or absorbed by other excitations, such as phonons or the electromagnetic radiation field. The last term on the left hand side of Eq. (23) describes the Joule heating due to the applied voltage. In what follows, we write the volume explicitly in the collision integral by averaging over a small volume \mathcal{V} around the point \mathbf{r} where $T(\mathbf{r})$ is approximately constant, thus defining $P_{\text{coll}}(\mathbf{r}) \equiv \mathcal{V} \tilde{I}_{\text{coll}}$.

For the electron-phonon scattering (Wellstood *et al.*, 1994), P_{coll} reads in the clean case (see also Table I)

$$P_{\text{coll}}^{e-ph} = \Sigma \mathcal{V} (T_e(\mathbf{r})^5 - T_{ph}(\mathbf{r})^5). \quad (24)$$

For the dirty limit specified below Eq. (20), the Eliashberg functions scaling with ω^n translate into temperature dependences scaling as T^{n+3} , i.e., T^4 and T^6 (Sergeev and Mitin, 2000).

The electrons can also be heated due to the thermal noise in their electromagnetic environment unless proper filtering is realized to prevent this heating. If one aims to detect the electromagnetic environment as discussed in Sec. IV, this discussion can of course be turned around to find the optimal coupling to the radiation to be observed. A model for such coupling in the quasiequilibrium limit

was considered by Schmidt *et al.* (2004a), who obtained an expression for the emitted/absorbed power due to the external noise in the form

$$P_{\text{coll}}^{e-em} = r \frac{k_B^2 \pi^2}{6h} (T_e^2 - T_{\gamma}^2). \quad (25)$$

Here $r = 4R_e R_{\gamma} / (R_e + R_{\gamma})^2$ is the coupling constant, T_{γ} is the (noise) temperature of the environment, and R_e and R_{γ} are the resistances characterizing the thermal noise in the electron system and the environment, respectively. This expression assumes a frequency independent environment in the relevant frequency range. For some examples on the frequency dependence, we refer to Schmidt *et al.* (2004a).

E. Observables

1. Currents

In the nonequilibrium diffusive limit, the charge current in a normal-metal wire in the absence of a proximity effect or any such interference effects as weak localization is obtained from the local distribution function by

$$I = -eA \int_{-\infty}^{\infty} dE D(E) \nu(E) \nabla f(x; E) \quad (26)$$

and the heat current from a reservoir with potential μ is

$$\dot{Q} = -A \int_{-\infty}^{\infty} dE (E - \mu) D(E) \nu(E) \nabla f(x; E). \quad (27)$$

Here we included the possible energy dependence of the diffusion constant $D(E)$ and of the density of states $\nu(E)$, due to the energy dependence of the elastic scattering time, or due to the nonlinearities in the quasiparticle dispersion relation. If the Kondo effect (Vavilov *et al.*, 2003) can be neglected, such effects are very small in good metals at temperatures of the order of 1 K or less.

In the quasiequilibrium limit, assuming $D(E) = \text{const.}$ and $\nu(E) = \nu_F$, Eqs. (26,27) can be simplified to

$$I = -\sigma A \nabla \mu / e \quad (28a)$$

$$\dot{Q} = -\kappa A \nabla T. \quad (28b)$$

When a diffusive wire of resistance R_D is connected to a reservoir through a point contact characterized by the transmission eigenvalues $\{\mathcal{T}_n\}$, the final distribution function is obtained after solving the Boltzmann equation (3) or Eqs. (5) with the boundary conditions given by Eq. (6), (8), or by (9). However, when R_D is much less than the normal-state resistance $1/G_N$ of the contact, we can ignore the wire and obtain the full current by a direct integration over Eq. (8) or Eq. (9). For example, for NIS or SIS tunnel junctions, the expressions for the

¹ In the diffusive limit where the inelastic scattering rates are lower than $1/\tau$, this is related to the particle number conservation and is thus generally valid.

charge and heat currents from the left side of the junction become

$$I = \frac{1}{eR_T} \int dE N_L(\tilde{E}) N_R(E) [f_L(E) - f_R(E)] \quad (29)$$

$$\dot{Q} = \frac{1}{e^2 R_T} \int dE \tilde{E} N_L(\tilde{E}) N_R(E) [f_L(E) - f_R(E)]. \quad (30)$$

Here $\tilde{E} = E - eV$, $R_T = 1/G_N$, $N_{L/R}(E) = \nu(E)/\nu_F$ is the reduced density of states for the left/right wire, $N(E) = 1$ for a normal metal and $N(E) = N_S(E)$ for a superconductor. Furthermore, if the two wires constitute reservoirs, $f_{L/R}$ are Fermi functions with potentials $\mu_L = -eV$, $\mu_R = 0$. The resulting NIS or SIS charge current is a sensitive probe of temperature and can hence be used for thermometry or radiation detection, as explained in Secs. III.A and IV, respectively. Moreover, analysis of the heat current Eq. (30) shows that the electrons can in certain situations be cooled in NIS/SIS structures, as discussed in Sec. V.C.1.

In the presence of a proximity effect, the equations for the charge and thermal currents in the quasiclassical limit, i.e., ignoring the energy dependence of the diffusion constant and the normal-metal density of states, are

$$I = \int dE j^T \quad (31a)$$

$$\dot{Q} = \int dE (E j^L - \mu j^T). \quad (31b)$$

Here μ is the potential of the reservoir from which the heat current is calculated. As in Eq. (5), these currents can be separated into quasiparticle, anomalous, and supercurrent parts.

2. Noise

Often one can express the zero-frequency current noise in terms of the local distribution function (Blanter and Büttiker, 2000). The noise is characterized by the correlator

$$S = 2 \int_{-\infty}^{\infty} dt' \langle \delta \hat{I}(t+t') \delta \hat{I}(t) \rangle,$$

where $\delta \hat{I} = \hat{I} - \langle \hat{I} \rangle$ and \hat{I} is the current operator. In a stationary system S is independent of t . In a normal-metal wire of length L in the nonequilibrium limit, the current noise S can be expressed as (Nagaev, 1992)

$$S = \frac{4eD\nu_F A}{L^2} \int_0^L dx \int_{-\infty}^{\infty} dE f(E, x) [1 - f(E, x)]. \quad (32)$$

In the quasiequilibrium regime, this equation simplifies to (Nagaev, 1995)

$$S = \frac{4eD\nu_F A k_B}{L^2} \int_0^L dx T_e(x). \quad (33)$$

When the resistance of a point contact dominates that of the wire, the noise power can be expressed through (Blanter and Büttiker, 2000)

$$S_{NN} = \frac{4e^2}{h} \sum_n \int dE \{ \mathcal{T}_n [f_L(1 - f_L) + f_R(1 - f_R)] + \mathcal{T}_n(1 - \mathcal{T}_n)(f_L - f_R)^2 \}$$

for a normal-metal contact and (de Jong and Beenakker, 1994)

$$S_{NS} = \frac{2e^2}{h} \sum_n \int dE \left\{ \frac{\mathcal{T}_n^2}{(2 - \mathcal{T}_n)^2} 2f_L(E)[1 - f_L(E)] + \frac{16\mathcal{T}_n^2(1 - \mathcal{T}_n)}{(2 - \mathcal{T}_n)^4} (f_L^T)^2 \right\}$$

for an incoherent NS contact at $E < \Delta$. Here $f^{L/R}$ are the distribution functions in the left/right (normal/superconducting in the latter case) side of the contact and $f_L^T(E) = 1 - f_L(E) - f_L(-E)$, the symmetric part w.r.t. the S potential. If the scattering probabilities are independent of energy and if the two sides are reservoirs with the same temperature, these expressions simplify to

$$S_{NN} = \frac{2e^2}{h} \sum_n [2k_B T \mathcal{T}_n^2 + eV \coth(v) \mathcal{T}_n(1 - \mathcal{T}_n)] \quad (34a)$$

$$S_{NS} = \frac{2e^2}{h} \sum_n \left[\frac{\mathcal{T}_n^2}{(2 - \mathcal{T}_n)^2} 2k_B T + \frac{16\mathcal{T}_n^2(1 - \mathcal{T}_n)}{(2 - \mathcal{T}_n)^4} (2eV \coth(v) - 4k_B T) \right], \quad (34b)$$

where $v = eV/(2k_B T)$. For $eV = 0$ (thermal Johnson-Nyquist noise), $S_{NN/S} = 4k_B T G_{N/S}$, where $G_{NRK} = \sum_n \mathcal{T}_n$ and $G_{SRK} = \sum_n \mathcal{T}_n^2/(2 - \mathcal{T}_n)^2$ are the conductances of the point contact in the NN and NS cases, respectively. In the opposite limit $eV \gg k_B T$ (shot noise), one obtains $S = 2eF_{N/S}I_{N/S}$, where $I_{N/S} = G_{N/S}V$ is the average current through the junction, and $F_{N/S}$ are the Fano factors: $F_N G_{NRK} = \sum_n \mathcal{T}_n(1 - \mathcal{T}_n)$ and $F_S G_{SRK} = \sum_n 16\mathcal{T}_n^2(1 - \mathcal{T}_n)/(2 - \mathcal{T}_n)^4$.

In the presence of the superconducting proximity effect, the expression for the noise becomes more complicated (Houzet and Pistolesi, 2004). In general, it can be found by employing the counting-field technique developed by Nazarov and coworkers, see (Nazarov and Bagrets, 2002) and the references therein. This technique can also be applied to study the full counting statistics of the transmitted currents through a given sample within a given measurement time (Nazarov, 2003).

Apart from the charge current, also the heat current in electric circuits fluctuates. For example, the zero-frequency heat current noise from the "left" of a tunnel

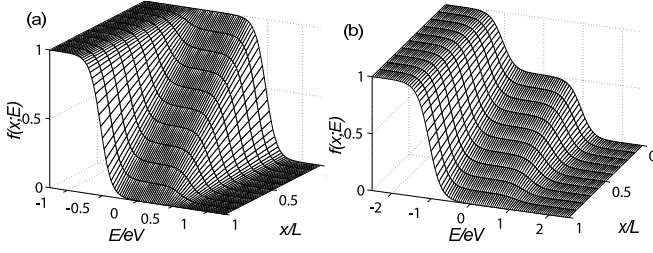


FIG. 2 Nonequilibrium quasiparticle energy distribution function in a diffusive normal-metal wire in the absence of inelastic scattering: (a) wire placed between two normal-metal reservoirs and (b) wire placed between a normal-metal ($x = L$) and a superconducting ($x = 0$) reservoir. In the latter picture, we assume $\hbar D/L^2 \ll eV \ll \Delta$, such that the proximity effect and the states above the gap can be neglected. In both pictures, the lattice temperature was fixed to $k_B T = eV/10$.

contact biased with voltage V is given by

$$S_Q = \frac{2}{e^2 R_T} \int dE E^2 N_L(E - eV) N_R(E) [f_R(1 - f_L) + f_L(1 - f_R)]. \quad (35)$$

At low voltages $V \ll k_B T/e$, the heat current noise obeys the fluctuation-dissipation result $S_Q = 4k_B T^2 G_{\text{th}}$, where G_{th} is the thermal conductance. This quantity is related to the noise equivalent power (NEP) discussed in the literature of thermal detectors by $S_Q = \text{NEP}^2$. The total NEP contains contributions not only from the electrical heat current noise, but also from other sources, such as the direct charge current noise and electron-phonon coupling. A detailed discussion of various NEP sources is presented in Sec. IV.

Another important quantity is the cross-correlator between the current and heat current fluctuations. At zero frequency, this is given by

$$S_{IQ} = -\frac{2}{e R_T} \int dE E N_L(E - eV) N_R(E) [f_R(1 - f_L) + f_L(1 - f_R)]. \quad (36)$$

These types of fluctuations have to be taken into account for example when analyzing the NEP of bolometers (Golubev and Kuzmin, 2001). Recently, also the general statistics of the heat current fluctuations have been theoretically addressed by Kindermann and Pilgram (2004).

F. Examples on different systems

Below, we detail the solutions to the kinetic equations, (3) or (5) in some example systems. The aim is first to provide an understanding of the general behavior of the distribution function in these systems, but also to show the generic features, such as the electron cooling in NIS junctions.

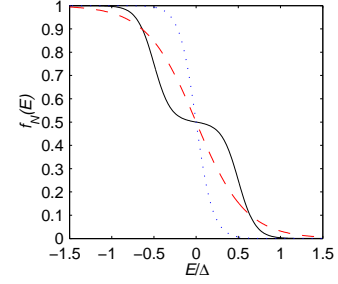


FIG. 3 (Color in online edition): Quasiparticle energy distribution function in the center of a normal-metal wire placed between two normal-metal reservoirs and biased with a voltage $eV = 10k_B T$. The three lines correspond to three extreme limits: $L \ll \ell_{e-e}, \ell_{e-ph}$ (nonequilibrium limit, black solid line), $\ell_{e-e} \ll L \ll \ell_{e-ph}$ (quasiequilibrium limit, red dashed line), and $\ell_{e-e}, \ell_{e-ph} \ll L$ (equilibrium limit, blue dotted line).

1. Normal-metal wire between normal-metal reservoirs

The simplest example is a quasi-one-dimensional normal-metal diffusive wire of resistance $R_D = L/(A\sigma)$, connected to two normal-metal reservoirs by clean contacts. In the full nonequilibrium limit, we find (see Fig. 2 (a); the coordinate x follows Fig. 1)

$$f(E, x) = f_L(E) + [f_R(E) - f_L(E)] \frac{x}{L}, \quad (37)$$

where f_L and f_R are the (Fermi) distribution functions in the left and right reservoirs with temperatures T_L and T_R and potentials μ_L and $\mu_R = \mu_L + eV$, respectively. The resulting two-step form illustrated in Fig. 2a was first measured by Pothier *et al.* (1997b).

In the quasiequilibrium limit, we get $f(E, x) = f_{\text{eq}}(E; \mu(x), T_e(x))$, where

$$\mu(x) = \mu_L + eV \frac{x}{L} \quad (38a)$$

$$T_e(x)^2 = T_L^2 + (T_R^2 - T_L^2) \frac{x}{L} + \frac{V^2}{L_0} \frac{x}{L} \left(1 - \frac{x}{L}\right). \quad (38b)$$

In both cases, the current is simply given by $I = V/R_D$ and the heat current in the limit $V = 0$ by $\dot{Q} = L_0(T_R^2 - T_L^2)/R_D$. For $V \neq 0$, the resistor dissipates power and \dot{Q} is not conserved. The electron distribution function in the center of the wire, $x = L/2$ is plotted in Fig. 3 for the nonequilibrium, quasiequilibrium and local equilibrium (strong electron-phonon scattering) limits.

To obtain estimates for the thermoelectric effects due to the particle-hole symmetry breaking, let us lift the assumption of energy independent diffusion constant and density of states, expanding them as $D(E) \approx D_0 + c_D \frac{E - E_F}{E_F}$ and $\nu(E) \approx \nu_F + c_N \frac{E - E_F}{E_F}$. For linear response, the resulting expressions for the charge and heat currents are (Cutler and Mott, 1969)

$$I = -GL \nabla \mu / e + GL \alpha \nabla T \quad (39a)$$

$$\dot{Q} = -\Pi GL \nabla \mu / e + G_{\text{th}} L \nabla T. \quad (39b)$$

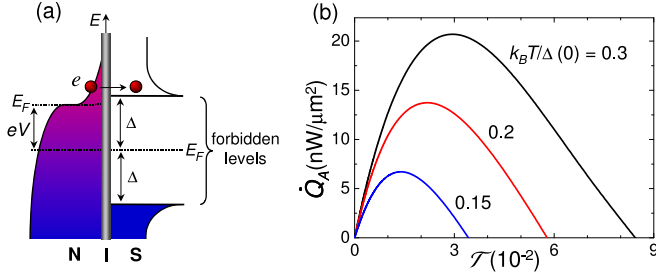


FIG. 4 Electron cooling at NIS junctions. (a) Sketch of the energy band diagram of a voltage biased NIS junction. Upon biasing the structure, the most energetic electrons (e) can most easily tunnel into the superconductor. As a result the electron gas in the N electrode is *cooled*. (b) Maximum cooling power surface density \dot{Q}_A vs interface transmissivity \mathcal{T} at different temperatures calculated for a NS contact.

Here $G = e^2 \nu_F D_0 A / L$ is the Drude conductance, $G_{\text{th}} = L_0 G T = \kappa A / L$ (Wiedemann-Franz law) is the heat conductance, $\alpha = e L_0 G' T / G$ (Mott law) is the Seebeck coefficient describing the thermoelectric power, $\Pi = \alpha T$ (Onsager relation) is the Peltier coefficient, and $G' = e^2 (c_D \nu_F + D_0 c_N) A / (L E_F)$ describes effects due to the particle-hole symmetry breaking. We see that the thermoelectric effects are in general of the order $k_B T / E_F$; in good metals at temperatures of the order of 1 K they can hence be typically ignored. Therefore, the Peltier refrigerators discussed in Subs. V.B rely on materials with a low E_F .

2. Superconducting tunnel structures

Consider a NIS tunnel structure, coupling a large superconducting reservoir with temperature $T_{e,S}$ to a large normal-metal reservoir with temperature $T_{e,N}$ via a tunnel junction with resistance R_T . Let us then assume a voltage V applied over the system. In this case, the heat current (cooling power) from the normal metal is given by Eq. (30) with $N_L(E) = 1$, $N_R(E) = N_S(E)$, $f_L(E) \equiv f_{\text{eq}}(E - eV, T_{e,N})$ and $f_R(E) \equiv f_{\text{eq}}(E, T_{e,S})$. For small pair breaking inside the superconductor, i.e., $\Gamma \ll \Delta$, \dot{Q}_{NIS} is positive for $eV < \Delta$, i.e., it *cools* the normal metal. It is straightforward to show that $\dot{Q}_{\text{NIS}}(V) = \dot{Q}_{\text{NIS}}(-V)$. This is in contrast with Peltier cooling, where the sign of the current determines the direction of the heat current. For $eV > \Delta$, the current through the junction increases strongly, resulting in Joule heating and making \dot{Q}_{NIS} negative. The cooling power is maximal near $eV \approx \Delta$.

In order to understand the basic mechanism for cooling in such systems, let us consider the simplified energy band diagram of a NIS tunnel junction biased at voltage V , as depicted in Fig. 4(a). The physical mechanism underlying quasiparticle cooling is rather simple: owing to the presence of the superconductor, in the tunneling

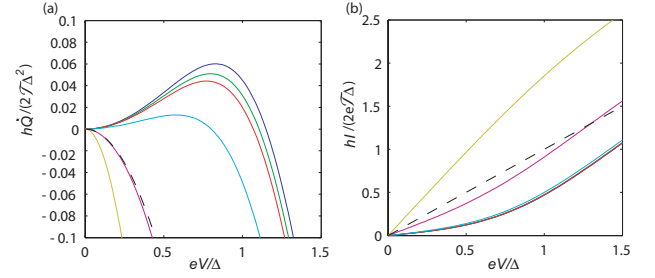


FIG. 5 NS point contact characteristics. (a) Heat current from the N side as a function of voltage for different transparencies \mathcal{T} (from top to bottom, tunneling limit $\mathcal{T} \rightarrow 0$, $\mathcal{T} = 0.005$, $\mathcal{T} = 0.01$, $\mathcal{T} = 0.05$, $\mathcal{T} = 0.5$ and $\mathcal{T} = 1$) at $k_B T = 0.3\Delta$. For $\mathcal{T} \lesssim 0.05$, the heat current is positive, corresponding to cooling. (b) Current-voltage characteristics for the same values of \mathcal{T} and \mathcal{T} as in (a) (now \mathcal{T} increases from bottom to top). The first four curves lie essentially on top of each other. The corresponding NIN curves are shown with the dashed lines.

process quasiparticles with energy $E < \Delta$ cannot tunnel inside the forbidden energy gap, but the more energetic electrons (with $E > \Delta$) are removed from the N electrode. As a consequence of this "selective" tunneling of hot particles, the electron distribution function in the N region becomes sharper: the NIS junction thus behaves as an electron cooler.

The role of barrier transmissivity in governing heat flux across the NIS structure was analyzed by Bardas and Averin (1995). They pointed out the interplay between single-particle tunneling and Andreev reflection (Andreev, 1964a) on the heat current. In the following it is useful to summarize their main results.

The cooling regime requires a tunnel contact. The effect of transmissivity is illustrated in Fig. 4(b), which shows the maximum of the heat current density (i.e., the specific cooling power) \dot{Q}_A versus interface transmissivity \mathcal{T} at different temperatures. This can be calculated for a generic NS junction using Eqs. (9), (10a) and (31b). The quantity \dot{Q}_A is a non-monotonic function of interface transmissivity, vanishing both at low and high values of \mathcal{T} . In the low transparency regime, \dot{Q}_A turns out to be linear in \mathcal{T} , showing that electron transport is dominated by single particle tunneling. Upon increasing barrier transmissivity, Andreev reflection begins to dominate quasiparticle transport, thus suppressing heat current extraction from the N portion of the structure. The heat current \dot{Q}_A is maximized between these two regimes at an optimal barrier transmissivity, which is temperature dependent. Furthermore, by decreasing the latter leads to a reduction of both the optimal \mathcal{T} and of the transmissivity window where the cooling takes place. In real NIS contacts used for cooling applications, the average \mathcal{T} is typically in the range $10^{-6} \dots 10^{-4}$ (Leivo *et al.*, 1996; Nahum *et al.*, 1994) corresponding to junction specific resistances R_c (i.e., the product of the junction normal state resistance and the contact area) from tens to sev-

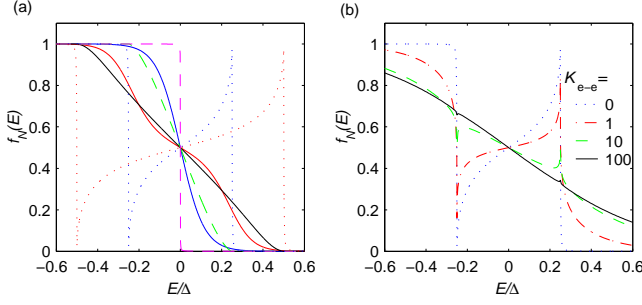


FIG. 6 Nonequilibrium distribution inside the SINIS island, calculated from Eq. (42): (a) No inelastic scattering, $\mathcal{I}_{\text{coll}} = 0$, $T = 0.1T_c$, and using a depairing strength $\Gamma = 10^{-4}\Delta$ inside the superconductors. The voltage runs from zero to $V = 3\Delta/e$ in steps of $\Delta/(2e)$ and spans three regimes: (i) anomalous heating regime ($eV = 0 \dots \Delta$, solid lines, widening with an increasing V) discussed in (Pekola *et al.*, 2004a), (ii) cooling regime ($eV = 1.5\Delta$ and $eV = 2\Delta$, dashed lines, narrowing with an increasing V) and the strong nonequilibrium heating regime ($eV = 2.5\Delta$ and $eV = 3\Delta$, dotted lines, widening with an increasing V). (b) Distribution at $eV = 2.5\Delta$ for different strengths of the electron–electron interaction, parametrized by the parameter K_{e-e} from Eq. (16) with R_D replaced by R_T and E^* by Δ , as in this case these describe the collision integral.

eral thousands $\Omega\mu\text{m}^2$. This limits the achievable \dot{Q}_A to some $\text{pW}/\mu\text{m}^2$. From the above discussion it appears that exploiting low- R_c tunnel contacts is an important requirement in order to achieve large cooling power through NIS junctions. However, in real low- R_c barriers, pinholes with a large T appear. They contribute with a large Joule heating (see Fig. 5, which shows the heat and charge currents through the NIS interface as functions of voltage for different T), and therefore tend to degrade the cooling performance at the lowest temperatures, and to overheat the superconductor at the junction region due to strong power injection. Barrier optimization in terms of both materials and technology seems to be still nowadays a challenging task (see also Sec. VI.F.1).

In a SINIS system in the quasiequilibrium limit, the temperatures $T_{e,N}$ and $T_{e,S}$ of the N and S parts may differ. If the superconductors are good reservoirs, $T_{e,S}$ equals the lattice temperature. In the experimentally relevant case when the resistance R_D of the normal-metal island is much lower than the resistances R_L and R_R of the tunnel junctions, the normal-metal temperature $T_{e,N}$ is determined from the heat balance equation

$$\dot{Q}_{\text{SINIS}}(V; T_{e,S}, T_{e,N}) = P_{\text{coll}}, \quad (40)$$

where $\dot{Q}_{\text{SINIS}} = 2\dot{Q}_{\text{NIS}}$ and P_{coll} describes inelastic scattering due to phonons (Eq. (24)) and/or due to the electromagnetic environment (Eq. (25)).

For further details about NIS/SINIS cooling in the quasiequilibrium limit, we refer to Sec. V.C.1 and (Anghel and Pekola, 2001).

Let us now consider the limit of full nonequilibrium, neglecting the proximity effect from the superconductors

on the normal-metal island.² Then the distribution function inside the normal metal may be obtained by solving the kinetic equation Eq. (3) in the static case along with the boundary conditions given by Eq. (8). For simplicity, let us assume $R_L = R_R \equiv R_T \gg R_D$. In this limit, the distribution function $f_N(E)$ in the normal-metal island is almost independent of the spatial coordinate. Then, in Eq. (3) we can use $\partial_x^2 f \approx (\partial_x f(L) - \partial_x f(0))/L$, where L is the length of the N wire. From Eq. (11) we then get

$$\frac{R_D}{R_T} (N_R(f_N - f_R) - N_L(f_L - f_N)) = \tau_D \mathcal{I}_{\text{coll}}, \quad (41)$$

where $\tau_D = L_N^2/D$ is the diffusion time through the island. As a result (Giazotto *et al.*, 2004b; Heslinga and Klapwijk, 1993), the distribution function in the central wire can be expressed as

$$f_N = \frac{f_R N_R + f_L N_L + R_I \mathcal{V} e^2 \nu_F \mathcal{I}_{\text{coll}}}{N_R + N_L}. \quad (42)$$

Here $\mathcal{V} = LA$ is the volume of the island. In the presence of inelastic scattering, this is an implicit equation, as $\mathcal{I}_{\text{coll}}$ is a functional of f_N . Examples of the effect of inelastic scattering have been considered in (Heslinga and Klapwijk, 1993) in the relaxation time approach, and in (Giazotto *et al.*, 2004b) including the full electron–electron scattering collision integral. The distribution function f_N in Eq. (42) is plotted in Fig. 6 for a few values of the voltage for $\mathcal{I}_{\text{coll}} = 0$ and for a few strengths of electron–electron scattering at $eV = 2.5\Delta$.

3. Superconductor-normal-metal structures with transparent contacts

If a superconductor is placed in a good electric contact with a normal metal, a finite pairing amplitude is induced in the normal metal within a thermal coherence length $\xi_T = \sqrt{\hbar D/(2\pi k_B T)}$ near the interface. This superconducting *proximity effect* modifies the properties of the normal metal (Belzig *et al.*, 1999; Lambert and Raimondi, 1998) and makes it possible to transport supercurrent through it. It also changes the local distribution functions by modifying the kinetic coefficients in Eq. (5). Superconducting proximity effect is generated by Andreev reflection (Andreev, 1964b) at the normal-superconducting interface, where an electron scatters from the interface as a hole and vice versa. Andreev reflection forbids the sub-gap energy transport into the superconductor, and thus modifies the boundary conditions for the distribution functions. In certain cases, the proximity effect is not relevant for the physical observables whereas the Andreev reflection can still contribute. This incoherent regime is realized if one is interested in length scales much longer than the extent of

² This is justified in the limit $R_L, R_R \gg R_D$.

the proximity effect. Below, we first study such "pure" Andreev-reflection effects, and then go on to explain how they are modified in the presence of the proximity effect.

In the incoherent regime, for $E < \Delta$, Andreev reflection can be described through the boundary conditions (Pierre *et al.*, 2001)

$$f(\mu_S + E) = 1 - f(\mu_S - E) \quad (43a)$$

$$\hat{\mathbf{n}} \cdot \nabla [f(\mu_S - E) - f(\mu_S + E)] = 0, \quad (43b)$$

evaluated at the normal-superconducting interface. Here $\hat{\mathbf{n}}$ is the unit vector normal to the interface and μ_S is the chemical potential of the superconductor. The former equation guarantees the absence of charge imbalance in the superconductor, while the latter describes the vanishing energy current into it. For $E > \Delta$, the usual normal-metal boundary conditions are used. Note that these boundary conditions are valid as long as the resistance of the wire by far exceeds that of the interface; in the general case, one should apply Eqs. (9).

Assume now a system where a normal-metal wire is placed between normal-metal (at $x = L$, potential μ_N and temperature $T = T_{e,N}$) and superconducting reservoirs (at $x = 0$, $\mu_S = 0$, $T = T_{e,S}$). Solving the Boltzmann equation (3) then yields (Nagaev and Buttiker, 2001)

$$f(E) = \begin{cases} \frac{1}{2} \left(1 + \frac{x}{L}\right) f_N(E) + \frac{1}{2} \left(1 - \frac{x}{L}\right) \bar{f}_N(E), & E < \Delta \\ \left(1 - \frac{x}{L}\right) f_{\text{eq}}(E; \mu = 0, T_{e,S}) + \frac{x}{L} f_N(E), & E > \Delta. \end{cases} \quad (44)$$

Here $f_N(E) = f_{\text{eq}}(E; \mu_N, T_{e,N})$ and $\bar{f}_N(E) = f_{\text{eq}}(E; -\mu_N, T_{e,N})$. This function is plotted in Fig. 2 (b). In the quasiequilibrium regime, the problem can be analytically solved in the case $eV, k_B T \ll \Delta$, i.e., when Eqs. (43) apply for all relevant energies. Then the boundary conditions are $\mu = \mu_S = 0$ and $\hat{\mathbf{n}} \cdot \nabla T_e = 0$ at the NS interface. Thus, the quasiequilibrium distribution function is given by $f(E, x) = f(E; \mu(x), T_e(x))$ with $\mu(x) = \mu_N(1 - x/L)$ and

$$T_e(x) = \sqrt{T_{e,N}^2 + \frac{V^2}{L_0} \frac{x}{L} \left(2 - \frac{x}{L}\right)}. \quad (45)$$

Note that this result is independent of the temperature $T_{e,S}$ of the superconducting terminal.

In this incoherent regime, the electrical conductance is unmodified compared to its value when the superconductor is replaced by a normal-metal electrode: Andreev reflection effectively doubles both the length of the normal conductor and the conductance for a single transmission channel (Beenakker, 1992), and thus the total conductance is unmodified. Wiedemann-Franz law is violated by the Andreev reflection: there is no heat current into the superconductor at subgap energies. However, the sub-gap current induces Joule heating into the normal metal and this by far overcompensates any cooling effect from the states above Δ (see Fig. 5).

The SNS system in the incoherent regime has also been analyzed by Bezuglyi *et al.* (2000) and Pierre *et al.* (2001). Using the boundary conditions in Eqs. (43) at both NS interfaces with different potentials of the two superconductors leads to a set of recursion equations that determine the distribution functions for each energy. The recursion is terminated for energies above the gap, where the distribution functions are connected simply to those of the superconductors. This process is called the multiple Andreev reflection: in a single coherent process, a quasiparticle with energy $E < -\Delta$ entering the normal-metal region from the left superconductor undergoes multiple Andreev reflections, and its energy is increased by the applied voltage during its traversal between the superconductors. Finally, when it has Andreev reflected $\sim (2\Delta/eV)$ times, its energy is increased enough to overcome the energy gap in the second superconductor. The resulting energy distribution function is a staircase pattern, and it is described in detail in (Pierre *et al.*, 2001). The width of this distribution is approximately 2Δ , and it thus corresponds to extremely strong heating even at low applied voltages.

The superconducting proximity effect gives rise to two types of important contributions to the electrical and thermal properties of the metals in contact to the superconductors: it modifies the charge and energy diffusion constants in Eqs. (5), and allows for finite supercurrent to flow in the normal-metal wires.

The simplest modification due to the proximity effect is a correction to the conductance in NN'S systems, where N' is a phase-coherent wire of length L , connected to a normal and a superconducting reservoir via transparent contacts. In this case, $j_S = T^{\text{an}} = 0$ and the kinetic equation for the charge current reduces to the conservation of $j^T = \mathcal{D}_T \partial_x f^T$. This can be straightforwardly integrated, yielding the current

$$I = G_N/e \int dE f_{\text{eq}}^T(E; V) D_T(E), \quad (46)$$

where $f_{\text{eq}}^T(E; V) = \{\tanh[(E + eV)/(2k_B T)] - \tanh[(E - eV)/(2k_B T)]\}/2$, T is the temperature in the normal-metal reservoir, and we assumed the normal metal in potential $-eV$. The proximity effect can be seen in the term $D_T = (\int_0^L \frac{dx}{\mathcal{D}_T(x; E)})^{-1}$. For $T = 0$, the differential conductance is $dI/dV = D_T(eV)G_N$. A detailed investigation of $D_T(E)$ requires typically a numerical solution of the retarded/advanced part of the Usadel equation (Golubov *et al.*, 1997). In general, it depends on two energy scales, the Thouless energy $E_T = \hbar D/L^2$ of the N' wire and the superconducting energy gap Δ . The behavior of the differential conductance as a function of the voltage and of the linear conductance as a function of the temperature are qualitatively similar, exhibiting the reentrance effect (Charlat *et al.*, 1996; Golubov *et al.*, 1997; den Hartog *et al.*, 1997): for $eV, k_B T \ll E_T$ and for $\max(eV, k_B T) \gg E_T$, they tend to the normal-state value G_N whereas for intermediate voltages/temperatures, the conductance is larger than

G_N , showing a maximum for $\max(eV, k_B T)$ of the order of E_T .

The proximity-effect modification to the conductance can be tuned in an Andreev interferometer, where a normal-metal wire is connected to two normal-metal reservoirs and two superconductors (Golubov *et al.*, 1997; Nazarov and Stoof, 1996; Pothier *et al.*, 1994). This system is schematized in the inset of Fig. 7. Due to the proximity effect, the conductance of the normal-metal wire is approximatively of the form $G(\phi) = G_N + \delta G(1 + \cos(\phi))/2$, where ϕ is the phase difference between the two superconducting contacts and δG is a positive temperature and voltage-dependent correction to the conductance. Its magnitude for typical geometries is at maximum some $0.1G_N$. The proximity-induced conductance correction is widely studied in the literature and we refer to (Belzig *et al.*, 1999; Lambert and Raimondi, 1998) for a more detailed list of references on this topic.

The thermal conductance of Andreev interferometers has been studied very recently. The formulation of the problem is very similar as for the conductance correction. For $E \ll \Delta$, there is no energy current into the superconductors. Therefore, it is enough to solve for the energy current $j^L = \mathcal{D}_L \partial_x f^L$ in the wires 1, 2 and 5. This yields

$$\dot{Q} = G_N/e^2 \int dE E D_L(E) (f_{\text{eq}}^L(E; T_2) - f_{\text{eq}}^L(E; T_1)),$$

where $f_{\text{eq}}^L(E; T) = \tanh[E/(2k_B T)]$ and the thermal conductance correction is obtained from $D_L(E) = (\int_0^L \frac{dx}{\mathcal{D}_L(x; E)})/L$. Here the spatial integral runs along the wire between the two normal-metal reservoirs. In the general case, D_L has to be calculated numerically. The thermal conductance correction has been analyzed by Bezuglyi and Vinokur (2003) and Jiang and Chandrasekhar (2005b). They found that it can be strongly modulated with the phase ϕ : in the short-junction limit where $E_T \gg \Delta$, for $\phi = 0$, D_L almost vanishes, whereas for $\phi = \pi$, D_L approaches unity and thus the thermal conductance approaches its normal-state value. For a long junction with $E_T \lesssim \Delta$, the effect becomes smaller, but still clearly observable. The first measurements (Jiang and Chandrasekhar, 2005a) of the proximity-induced correction to the thermal conductance show the predicted tendency of the phase-dependent decrease of κ compared to the normal-state (Wiedemann-Franz) value.

Prior to the experiments on heat conductance in proximity structures, the thermoelectric power α was experimentally studied in Andreev interferometers (Dikin *et al.*, 2002a,b; Eom *et al.*, 1998; Jiang and Chandrasekhar, 2004; Parsons *et al.*, 2003a,b). The observed thermopower was surprisingly large, of the order of 100 neV/K — at least one to two orders of magnitude larger than the thermopower in normal-metal samples. Also contrary to the Mott relation (c.f., below Eqs. (39)), this value depends nonmonotonically on the temperature (Eom *et al.*, 1998) at the temperatures of the order of a few hundred mK,

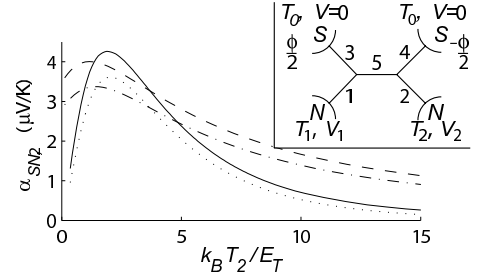


FIG. 7 Supercurrent-induced N-S thermopower α_{NS} for the system depicted in the inset. Solid line: α_{NS} at $T_1 \approx T_2$. Dotted line: approximation (47). The correction (48) accounts for most of the difference. Dashed line: α_{NS} at $k_B T_1 = 3.6 E_T$ with varying T_2 . Dash-dotted line: the corresponding approximation. Inset: Andreev interferometer where thermoelectric effects are studied. Two superconducting reservoirs with phase difference ϕ are connected to two normal-metal reservoirs through diffusive normal-metal wires. Adapted from (Virtanen and Heikkilä, 2004b).

and even a sign change could be found (Parsons *et al.*, 2003b). Moreover, the thermopower was found to oscillate as a function of the phase ϕ . The symmetry of the oscillations has in most cases been found to be antisymmetric with respect to $\phi = 0$, i.e., α vanishes for $\phi = 0$. However, in some measurements, the Chandrasekhar's group (Eom *et al.*, 1998; Jiang and Chandrasekhar, 2004) have found symmetric oscillations, i.e., α had the same phase as the conductance.

The observed behavior of the thermopower is not completely understood, but the major features can be explained. The first theoretical predictions were given by Claughton and Lambert (1996), who constructed a scattering theory to describe the effect of Andreev reflection on the thermoelectric properties of proximity systems. Based on their work, it was shown (Heikkilä *et al.*, 2000) that the presence of Andreev reflection can lead to a violation of the Mott relation. This means that a finite thermopower can arise even in the presence of electron-hole symmetry. Seviour and Volkov (2000b), Kogan *et al.* (2002), and Virtanen and Heikkilä (2004a,b) showed that in Andreev interferometers carrying a supercurrent, a large voltage can be induced by the temperature gradient both between the normal-metal reservoirs and between the normal metals and the superconducting contacts. Virtanen and Heikkilä (2004b) showed that in long junctions, the induced voltages between the two normal-metal reservoirs and the superconductors can be related to the temperature dependent equilibrium supercurrent $I_S(T)$ flowing between the two superconductors via

$$V_{1/2}^0 = \frac{1}{2} \frac{R_5(2R_{4/3} + R_5)R_{3/4} [I_S(T_1) - I_S(T_2)]}{R_{\text{NNN}}R_{\text{SNS}}}. \quad (47)$$

Here $R_{\text{NNN}} = R_1 + R_2 + R_5$, $R_{\text{SNS}} = R_3 + R_4 + R_5$ and R_k are the resistances of the five wires defined in the inset of Fig. 7. This is in most situations the dominant term and it can be also phenomenologically argued based on the temperature dependence of

the supercurrent and the conservation of total current (supercurrent plus quasiparticle current) in the circuit (Virtanen and Heikkilä, 2004b). A similar result can also be obtained in the quasiequilibrium limit for the linear-response thermopower (Virtanen and Heikkilä, 2004a). In addition to this term, the main correction in the long-junction limit comes from the anomalous coefficient \mathcal{T}^{an} ,

$$eV_{1/2}^1 = \frac{\mp R_{1/2}}{R_{\text{NNN}}} \langle \mathcal{T}_{1/2}^{\text{an}} \rangle \mp \frac{R_{3/4} R_5}{R_{\text{NNN}} R_{\text{SNS}}} \langle \mathcal{T}_5^{\text{an}} \rangle. \quad (48)$$

Here $\langle \mathcal{T}_k^{\text{an}} \rangle \equiv \frac{1}{L_k} \int_0^{L_k} dx \int_0^\infty dE \mathcal{T}_k^{\text{an}}(E) [f_{\text{eq}}^L(E, T_1) - f_{\text{eq}}^L(E, T_2)]$ and L_k is the length of wire k . One finds that for a "cross" system without the central wire (i.e., $R_5 = 0$), this term dominates $V_{1/2}^0$. Further corrections to the result (47) are discussed by Kogan *et al.* (2002) and Virtanen and Heikkilä (2004a).

The above theoretical results explain the observed magnitude and temperature dependence of the thermopower and also predict an induced voltage oscillating with the phase ϕ . However, the thermopower calculated by Seviour and Volkov (2000b), Kogan *et al.* (2002) and Virtanen and Heikkilä (2004a,b) is always an antisymmetric function of ϕ , and it vanishes for a vanishing supercurrent in the junction (including all the correction terms). Therefore, the symmetric oscillations of α cannot be explained with this theory.

The presence of the supercurrent breaks the time-reversal symmetry and hence the Onsager relation $\Pi = T\alpha$ (see Eqs. (39) and below) need not to be valid for $\phi \neq 0$. Heikkilä, *et al.* predicted a nonequilibrium Peltier-type effect (Heikkilä *et al.*, 2003) where the supercurrent controls the local effective temperature in an out-of-equilibrium normal-metal wire. However, it seems that the induced changes are always smaller than those due to Joule heating and thus no real cooling can be realized with this setup.

Recently, the thermoelectric effects in coherent SNS Josephson point contacts have been analyzed in (Zhao *et al.*, 2003, 2004). In such point contacts, the heat transport is strongly influenced by the Andreev bound states forming between the two superconductors.

G. Heat transport by phonons

When the electrons are thermalized by the phonons, they may also heat or cool the phonon system in the film. Therefore, it is important to know how these phonons further thermalize with the substrate, and ultimately with the heat bath on the sample holder that is typically cooled via external means (typically by either a dilution or a magnetic refrigerator). Albeit slow electron-phonon relaxation often poses the dominating thermal resistance in mesoscopic structures at low temperatures, the poor phonon thermal conduction itself can also prevent full thermal equilibration throughout the whole lattice. This

is particularly the case when insulating geometric constrictions and thin films separate the electronic structure from the bulky phonon reservoir (see Fig. 1). In the present section we concentrate on the thermal transport in the part of the chain of Fig. 1 beyond the sub-systems determined by electronic properties of the structure.

The bulky three-dimensional bodies cease to conduct heat at low temperatures according to the well appreciated $\kappa \propto T^3$ law in crystalline solids arising from Debye heat capacity via

$$\kappa = C v_S \ell_{\text{el,ph}}/3, \quad (49)$$

where κ is the thermal conductivity and C is the heat capacity per unit volume, v_S is the speed of sound and $\ell_{\text{el,ph}}$ is the mean free path of phonons in the solid (Ashcroft and Mermin, 1976). Thermal conductivity of glasses follows the universal $\propto T^2$ law, as was discovered by Zeller and Pohl (1971), which dependence is approximately followed by non-crystalline materials in general (Pobell, 1996). These laws are to be contrasted to $\propto T$ thermal conductivities of pure normal metals (Wiedemann-Franz law, c.f., below Eq. (39)). Despite the rapid weakening of thermal conductivity toward low temperatures, the dielectric materials in crystalline bulk are relatively good thermal conductors. One important observation here is that the absolute value of the bulk thermal conductivity in clean crystalline insulators at low temperatures does not provide the full basis of thermal analysis without a proper knowledge of the geometry of the structure, because the mean free paths often exceed the dimensions of the structures. For example, in pure silicon crystals, measured at sub-kelvin temperatures (Klitsner and Pohl, 1987), thermal conductivity $\kappa \simeq 10 \text{ Wm}^{-1}\text{K}^{-4}T^3$, heat capacity $C \simeq 0.6 \text{ JK}^{-4}\text{m}^{-3}T^3$ and velocity $v_S \simeq 5700 \text{ m/s}$ imply by Eq. (49) a mean free path of $\simeq 10 \text{ mm}$, which is more than an order of magnitude longer than the thickness of a typical silicon wafer. Therefore phonons tend to propagate ballistically in silicon substrates.

What makes things even more interesting, but at the same time more complex, e.g., in terms of practical thermal design, is that at sub-kelvin temperatures the dominant thermal wavelength of the phonons, $\lambda_{ph} \simeq \hbar v_S / k_B T$, is of the order of $0.1 \text{ }\mu\text{m}$, and it can exceed $1 \text{ }\mu\text{m}$ at the low temperature end of a typical experiment (see discussion in Subs. II.C.2). A direct consequence of this fact is that the phonon systems in mesoscopic samples cannot typically be treated as three-dimensional, but the sub-wavelength dimensions determine the actual dimensionality of the phonon gas. Metallic thin films and narrow thin film wires, but also thin dielectric films and wires are to be treated with constraints due to the confinement of phonons in reduced dimensions.

The issue of how thermal conductivity and heat capacity of thin membranes and wires get modified due to geometrical constraints on the scale of the thermal wavelength of phonons has been addressed by several authors experimentally (Holmes *et al.*, 1998; Leivo and Pekola,

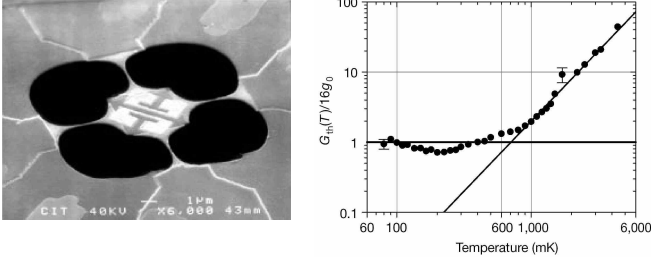


FIG. 8 The suspended silicon nitride bridge structure on the left, which was used by Schwab *et al.* (2000) to measure the quantum of thermal conductance shown in the graph on the right: thermal conductance levels off at the value $16g_0$ at temperatures well below 1 K. Adapted from (Schwab *et al.*, 2000).

1998; Woodcraft *et al.*, 2000) and theoretically (see, e.g., (Anghel *et al.*, 1998; Kuhn *et al.*, 2004)). The main conclusion is that structures with one or two dimensions $d < \lambda_{ph}$ restrict the propagation of (ballistic) phonons into the remaining “large” dimensions, and thereby reduce the magnitude of the corresponding quantities κ and C at typical sub-kelvin temperatures, but at the same time the temperature dependences get weaker.

In the limit of narrow short wires at low temperatures the phonon thermal conductance gets quantized, as was experimentally demonstrated by Schwab *et al.* (2000). This limit had been theoretically addressed by Angelescu *et al.* (1998), Rego and Kirczenow (1998) and Blencowe (1999), somewhat in analogy to the well-known Landauer result on electrical conduction through quasi-one-dimensional constrictions (Landauer, 1957). The quantum of thermal conductance is $g_0 \equiv \pi^2 k_B^2 T / (3h)$, and there are four phonon modes at low temperature due to four mechanical degrees of freedom each adding g_0 to the thermal conductance of the quantum wire. In an experiment, see Fig. 8 four such wires in parallel thus carried heat with conductance $g = 16g_0$. There are remarkable differences, however, in this result as compared to the electrical quantized conductance. In the thermal case, only one quantized level of conductance, $4g_0$ per wire, could be observed, and since the quantity transported is energy, the “quantum” of thermal conductance carries $\propto T$ in its expression besides the constants of nature.

The thermal boundary resistance (Kapitza resistance, after the Russian physicist P. Kapitza) between two bulk materials is $\propto T^{-3}$ due to acoustic mismatch (Lounasmaa, 1974). A remaining open issue is the question of thermal boundary resistance in a structure where at least one of the phonon baths facing each other is restricted, such that thermal phonons perpendicular to the interface do not exist in this particular subsystem. Classically the penetrating phonons need, however, to be perpendicular enough in order to avoid total reflection at the surface (Pobell, 1996). In practice though, the phonon

systems in the two subsystems cannot be considered as independent. We are not aware of direct experimental investigations on this problem.

On the device level reduced dimensions can be beneficial, e.g., in isolating thermally those parts of the devices to be refrigerated from those of the surrounding heat bath. This has been the method by which NIS based phonon coolers, i.e., refrigerators of the lattice have been realized experimentally utilizing thin silicon nitride films and narrow silicon nitride bridges (Clark *et al.*, 2005; Fisher *et al.*, 1999; Luukanen *et al.*, 2000; Manninen *et al.*, 1997). These devices are discussed in detail in Section V.C.

Detectors utilizing phonon engineering are discussed in Sec. IV.

H. Heat transport in a metallic reservoir

Energy dissipated per unit time in a biased mesoscopic structure is given quite generally as $\dot{Q} = IV$, where I is the current through and V is the voltage across the device. This power is often so large that its influence on the thermal budget has to be carefully considered when designing a circuit on a chip. For instance, the NIS cooler of Sec. V.C.1 has a coefficient of performance given by Eq. (77), with a typical value in the range $0.01 \dots 0.1$. This simply means that the total power dissipated is 10 to 100 times higher than the net power one evacuates from the system of normal electrons. Yet this tiny fraction of the dissipated power is enough to cool the electron system far below the lattice temperature due to the weakness of electron-phonon coupling. This observation implies that 10 to 100 times higher dissipated power outside the normal island tends to overheat the connecting electrode significantly, again because of the weakness of the electron-phonon coupling. Therefore it is vitally important to make an effort to thermalize the connecting reservoirs to the surrounding thermal bath efficiently. In the case of normal-metal reservoirs, heat can be conveniently conducted along the electron gas to an electrode with a large volume in which electrons can then cool via electron-phonon relaxation. In the case of a superconducting reservoir, e.g., in a NIS refrigerator, the situation is more problematic because of the very weak thermal conductivity at temperatures well below the transition temperature T_c . In this case the superconducting reservoirs should either be especially thick, or they should be attached to normal metal conductors (“quasiparticle traps”) as near as possible to the source of dissipation (see discussion in Sec. V.C.1). The latter approach is, however, not always welcome, because, especially in the case of a good metallic contact between the two conductors, the operation of the device itself can be harmfully affected by the superconducting proximity effect.

Let us consider heat transport in a normal metal reservoir. In the first example we approximate the reservoir geometry by a semi-circle, connected to a biased sample

with a hot spot of radius r_0 at its origin (see the inset of Fig. 9 (b)). This hot spot can approximate, for example, a tunnel junction of area πr_0^2 . The results depend only logarithmically on r_0 , and therefore its exact value is irrelevant when making estimates. We first assume that the electrons carry the heat away with negligible coupling to the lattice up to a distance r . According to Eq. (23), we can then write the radial flux of heat in the quasiequilibrium limit in the form

$$\dot{Q}(r) = -\kappa S dT/dr, \quad (50)$$

where κ is the electronic thermal conductivity, $S = \pi r t$ is the conduction area at distance r in a film of thickness t , and T is the temperature at radius r . According to the Wiedemann-Franz law and the temperature independent residual electrical resistivity in metals, one has $\kappa = L_0 \sigma T \equiv \kappa_0 T$ (see below Eq. (39)). With these assumptions, using Eq. (50), one finds a radial distribution of temperature

$$T(r_1) = \sqrt{T(r_2)^2 + \frac{\dot{Q} R_{\square}}{\pi L_0} \ln(r_2/r_1)}, \quad (51)$$

where r_1 and r_2 are two distances from the hot spot, and we defined the square resistance as $R_{\square} = \rho/t$. Thus making the reservoir thicker helps to thermalize it. The model above is strictly appropriate in the case where a thin film in form of a semi-circle is connected to a perfect thermal sink at its perimeter (at $r = r_2$). A more adequate model in a typical experimental case is obtained by assuming a uniform semi-infinite film connected at its side to a hot spot as above, but now assuming that the film thermalises via electron-phonon coupling. Using Eq. (50) and energy conservation one then obtains (see Sec. II.D)

$$\frac{d\dot{Q}}{dr} + \Sigma \pi r t (T^p - T_0^p) = 0, \quad (52)$$

where T_0 is the lattice temperature, and p is the exponent of electron phonon relaxation, typically $p = 5$. We can write this equation into a dimensionless form

$$\frac{d^2 u}{d\rho^2} + \frac{1}{\rho} \frac{du}{d\rho} = u^{p/2} - 1. \quad (53)$$

Here we have defined $u \equiv (T(r)/T_0)^2$ and $\rho \equiv r/r_S$, where $r_S \equiv \sqrt{\kappa_0/(2\Sigma)}/T_0^{p/2-1}$ is the length scale of temperature over which it relaxes towards T_0 . Figure 9 (a) shows the solutions of Eq. (53) for different values (1.1, 1.2, 1.5, 2.0, 2.5, and 3.0) of relative temperature rise $T(r_0)/T_0$. We see, indeed, that r_S determines the relaxation length. To have a concrete example let us consider a copper film with thickness $t = 200$ nm. For copper, using $p = 5$, we have $\kappa_0 \simeq 1 \text{ WK}^{-2}\text{m}^{-1}$ and $\Sigma \simeq 2 \cdot 10^9 \text{ WK}^{-5}\text{m}^{-3}$, which leads to a healing length of $r_S \sim 500 \mu\text{m}$ at the bath temperature of $T_0 = 100$ mK. The temperature rise versus input power \dot{Q} has been plotted in

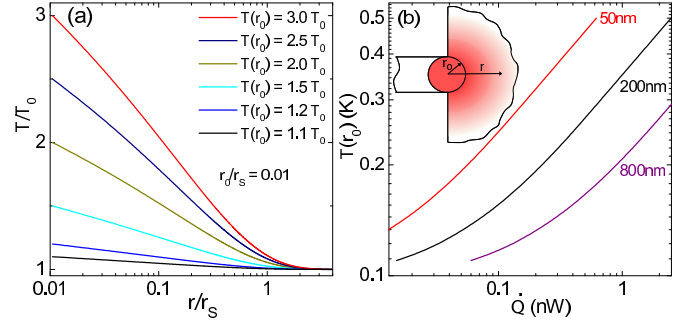


FIG. 9 (Color in online edition): Temperature rise according to the presented reservoir heating model. For details see text.

Fig. 9 (b) for copper films with different thicknesses. In particular for $t = 200$ nm, we obtain a linear response of $(T(r_0, \dot{Q})/T_0 - 1)/\dot{Q} \simeq 7 \cdot 10^{-4}/\text{pW}$.

A superconducting reservoir, which is a necessity in some devices, poses a much more serious overheating problem. Heat is transported only by the unpaired electrons whose number is decreasing exponentially as $\propto \exp(-\Delta/k_B T)$ towards low temperatures. Therefore the electronic thermal transport is reduced by approximately the same factor, as compared to the corresponding normal metal reservoir. Theoretically then κ is suppressed by nine orders of magnitude from the normal state value in aluminium at $T = 100$ mK. It is obvious that in this case other thermal conduction channels, like electron-phonon relaxation, become relevant, but this is a serious problem in any case. At higher temperatures, say at $T/T_C \geq 0.3$, a significantly thicker superconducting reservoir can help (Clark *et al.*, 2004).

III. THERMOMETRY ON MESOSCOPIC SCALE

Any quantity that changes with temperature can in principle be used as a thermometer. Yet the usefulness of a particular thermometric quantity in each application is determined by how well it satisfies a number of other criteria. These include, with a weighting factor that depends on the particular application: wide operation range with simple and monotonic dependence on temperature, low self-heating, fast response and measurement time, ease of operation, immunity to external parameters, in particular to magnetic field, small size and small thermal mass. One further important issue in thermometry in general terms is the classification of thermometers into *primary* thermometers, i.e., those that provide the absolute temperature without calibration, and into *secondary* thermometers, which need a calibration at least at one known temperature. Primary thermometers are rare, they are typically difficult to operate, but nevertheless they are very valuable, e.g., in calibrating the secondary thermometers. The latter ones are often easier to operate and thereby more common in research laboratories and in industry.

In this review we discuss a few mesoscopic thermometers that can be used at cryogenic temperatures. Excellent and thorough reviews of general purpose cryogenic thermometers, other than mesoscopic ones, can be found in many text books and review articles, see, e.g., (Lounasmaa, 1974; Pobell, 1996; Quinn, 1983) and many references therein.

Modern micro- and nanolithography allows for new thermometer concepts and realizations where sensors can be very small, thermal relaxation times are typically short, but which generally do not allow except very tiny amounts of self-heating. The heat flux between electrons and phonons gets extremely weak at low temperatures whereby electrons decouple thermally from the lattice typically at sub-100 mK temperatures, unless special care is taken to avoid this. Therefore, especially at these low temperatures the lattice temperature and the electron temperature measured by such thermometers often deviate from each other. An important example of this is the electron temperature in NIS electron coolers to be discussed in Section V.

A typical electron thermometer relies on a fairly easily and accurately measurable quantity M that is related to the electron energy distribution function $f(\varepsilon)$ via

$$M = \int_{-\infty}^{\infty} d\varepsilon k(\varepsilon) g[f(\varepsilon)]. \quad (54)$$

Here the kernel $k(\varepsilon)$ describes the process which is used to measure $f(\varepsilon)$ and $g[f]$ is a functional of $f(\varepsilon)$. The quantity M typically refers to an average current or voltage, in which case $g[f] = f - f_0$ is a linear function of $f(\varepsilon)$ with some constant function f_0 ; or it can refer to the noise power, in which case $g[f]$ is quadratic in f . For the thermometer to be easy to calibrate, $k(\varepsilon)$ should be a simple function dependent only on a few parameters that need to be calibrated. Moreover, if $k(\varepsilon)$ has sufficiently sharp features, it can be used to measure the shape of $f(\varepsilon)$ also in the nonequilibrium limit.

A. Hybrid junctions

Tunnelling characteristics through a barrier separating two conductors with non-equal densities of states (DOSs) are usually temperature dependent. The barrier B may be a solid insulating layer (I), a Schottky barrier formed between a semiconductor and a metal (Sc), a vacuum gap (I), or a normal metal weak link (N). We are going to discuss thermometers based on tunnelling in a CBC' structure. C and C' stand for a normal metal (N), a superconductor (S), or a semiconductor (Sm). As it turns out, the current-voltage ($I - V$) characteristics of the simplest combination, i.e., of a NIN tunnel junction, exhibit no temperature dependence in the limit of a very high tunnel barrier. Yet NIN junctions form elements of presently actively investigated thermometers (Coulomb blockade thermometer and shot noise thermometer) to

be discussed separately. The NIN junction based thermometers are suitable for general purpose thermometry, because their characteristics are typically not sensitive to external magnetic fields. Superconductor based junctions are, on the contrary, normally extremely sensitive to magnetic fields, and therefore they are suitable only in experiments where external fields can be avoided or at least accurately controlled.

In SBS' junctions one has to distinguish between two tunnelling mechanisms, Cooper pair tunnelling (Josephson effect) and quasiparticle tunnelling. The former occurs at low bias voltage and temperature, whereas the latter is enhanced by increased temperature and bias voltage. In the beginning of this section we discuss quasiparticle tunnelling only.

Let us consider tunnelling between two normal-metal conductors through an insulating barrier. I-V characteristics of such a junction were given by Eq. (29). We assume quasi-equilibrium with temperatures T_i , $i = L, R$ on the two sides of the barrier. Since $N_i(E) = 1$ to high precision at all relevant energies ($k_B T_i, eV \ll E_F = \text{Fermi energy}$), Eq. (29) can be integrated easily to yield $I = V/R_T$. Therefore the $I - V$ characteristics are ohmic, and they do not depend on temperature, and a NIN junction appears to be unsuitable for thermometry. There is, however, a weak correction to this result, due to the finite height of the tunnel barrier (Simmons, 1963a), which will be discussed in subsection III.D.

1. NIS thermometer

As a first example of an on-chip thermometer, let us discuss a tunnel junction between a normal metal and a superconductor (NIS junction) (Rowell and Tsui, 1976). I-V characteristics of a NIS junction have the very important property that they depend on the temperature of the N electrode only, which is easily verified, e.g., by writing $I(V)$ of Eq. (29) with $N_L(E) = \text{const.}$ and $N_R(E) = N_S(E)$ in a symmetric form

$$I(V) = \frac{1}{2eR_T} \int_{-\infty}^{\infty} N_S(E) [f_N(E - eV) - f_N(E + eV)] dE. \quad (55)$$

This insensitivity to the temperature of the superconductor holds naturally only up to temperatures where the superconducting energy gap can be assumed to have its zero-temperature value. This is true in practice up to $T/T_c \lesssim 0.4$.

Employing Eq. (55) one finds that a measurement of voltage V at a constant current $I = I_0$ yields a direct measure of $f_N(E)$, and in quasi-equilibrium, where the distribution follows thermal Fermi-Dirac distribution, it also yields temperature in principle without fit parameters. Figure 10 (a) shows the calculated I-V characteristics of a NIS junction at a few temperatures T/T_c . Figure 10 (b) gives the corresponding thermometer calibration: junction voltage has been plotted against temperature at

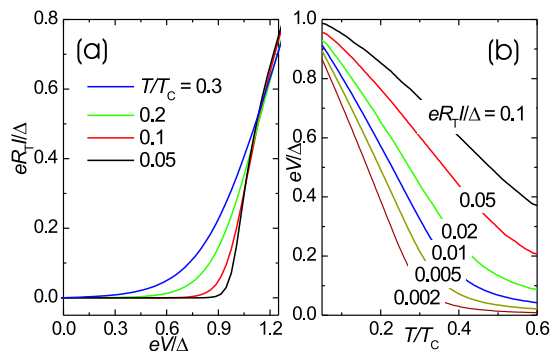


FIG. 10 NIS thermometer characteristics. Calculated I-V characteristics of a normal metal - superconductor tunnel junction at various relative temperatures T/T_c in (a). The corresponding voltage over the junction as a function of temperature when the junction is biased at a constant current is shown in (b). Characteristics at a few values of current are shown.

a few values of (constant) measuring current.

A NIS thermometer has a number of features which make it attractive in applications. The sensing element can be made very small and thereby NIS junctions can probe temperature locally and detect temperature gradients. Junctions made by electron beam lithography can be much smaller than $1\ \mu\text{m}$ in linear dimension (Nahum and Martinis, 1993). Using a scanning tunnelling microscope with a superconducting tip as a NIS junction one can most likely probe the temperature of the surface locally on nanometer scales in an instrument like those of Moussy *et al.* (2001); Vinet *et al.* (2001). Self-heating can be made very small by operating in the sub-gap voltage range $e|V| < \Delta$ (see Fig. 10), where current is very small. The superconducting probe is thermally decoupled from the normal region whose temperature is monitored by it. The drawbacks of this technique include high sensitivity to external magnetic field, high impedance of the sensor especially at low temperatures, and sample-to-sample deviations from the ideal theoretical behaviour. Due to this last reason, a NIS junction can hardly be considered as a primary thermometer: deviations arise especially at low temperatures, one prominent problem is saturation due to subgap leakage due to non-zero DOS within the gap and Andreev reflection.

A fast version of a NIS thermometer was implemented by Schmidt *et al.* (2003). They achieved sub- μs readout times (bandwidth about 100 MHz) by imbedding the NIS junction in an LC resonant circuit. This rf-NIS read-out is possibly very helpful in studying thermal relaxation rates in metals, and in fast far-infrared bolometry.

NIS junction thermometry has been applied in x-ray detectors (Nahum *et al.*, 1993), far-infrared bolometers (Chouvaev *et al.*, 1999; Mees *et al.*, 1991), in probing the energy distribution of electrons in a metal (Pothier *et al.*, 1997a), and as a thermometer in electronic coolers at sub-kelvin temperatures (Leivo *et al.*, 1996; Nahum *et al.*,

1994). It has also been suggested to be used as a far-infrared photon counter (Anghel and Kuzmin, 2003). In many of the application fields of a NIS thermometer it is not the only choice: for example, a superconducting transition edge sensor (TES) can be used very conveniently in the bolometry and calorimetry applications (see Sec. IV).

Recently Schottky contacts between silicon and superconducting metal have been shown to exhibit similar characteristics as fully metallic NIS junctions (Buonomo *et al.*, 2003; Savin *et al.*, 2001). These structures are discussed in subsection V.C.3.

2. SIS thermometer

A tunnel junction between two superconductors supports supercurrent, whose critical value I_C has a magnitude which depends on temperature according to (Ambegaokar and Baratoff, 1963): $I_C = \frac{\pi\Delta}{2eR_T} \tanh(\frac{\Delta}{2k_B T})$. This can naturally be used to indicate temperature because of the temperature dependence of the energy gap and the explicit hyperbolic dependence on T . Yet, these dependencies are exponentially weak at low temperatures. Another possibility is to suppress I_C by magnetic field, e.g., in a SQUID configuration, and to work at non-zero bias voltage and measure the quasiparticle current, which can be estimated by Eq. (29) again with both DOSs given by Eq. (12) now. The resulting current depends approximately exponentially on temperature, but the favourable fact is that the absolute magnitude of the current is increased because it is proportional to the product of the two almost infinite DOSs matching at low bias voltages, and, in practical terms, the method as a probe of a quasiparticle distribution is more robust against magnetic noise. Figure 11 shows the calculated and measured dependences of $I(V)$ at a few values of temperature T/T_c . Although the curves corresponding to the lowest temperatures almost overlap here, it is straightforward to verify that a standard measurement of current can resolve temperatures down to below $0.1T_c$ using an ordinary tunnel junction.

SIS junctions have not found much use as thermometers in the traditional sense, but they are extensively investigated and used as photon and particle detectors because of their high energy resolution (see, e.g., (Booth and Goldie, 1996) and Section IV). In this context SIS detectors are called STJ detectors, i.e., superconducting tunnel junction detectors. Another application of SIS structures is their use as mixers (Tinkham, 1996). While superficially similar to STJ detectors, their theory and operation differ significantly from each other. SIS junctions are also suitable for studies of quasiparticle dynamics and fluctuations in general (see, e.g., (Wilson *et al.*, 2001)).

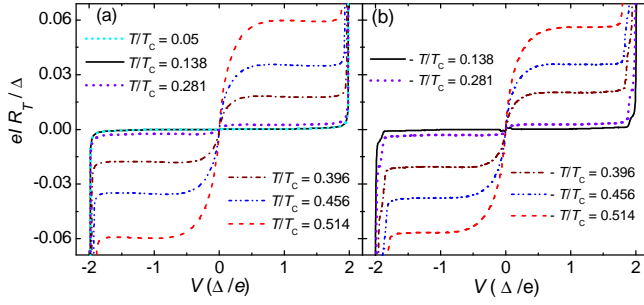


FIG. 11 SIS junction as a thermometer. (a) Calculated and (b) measured $I - V$ curves of a SIS tunnel junction at a few temperatures. Supercurrent has been suppressed. Experimental data from (Savin and Pekola, 2005).

3. Proximity effect thermometry

For applications requiring low-impedance ($\lesssim 1 \Omega$) thermometers at sub-micron scale, the use of clean NS contacts may be more preferable than thermometers applying tunnel contacts. In an SNS system, one may again employ either the supercurrent or quasiparticle current as the thermometer. For a given phase ϕ between the two superconductors, the former can be expressed through (Belzig *et al.*, 1999)

$$I_S(\phi) = \frac{1}{eR_N} \int_0^\infty dE j_S(E; \phi) (1 - 2f(E)), \quad (56)$$

where R_N is the normal-state resistance of the weak link, $j_S(E; \phi)$ is the spectral supercurrent (Heikkilä *et al.*, 2002), and the energies are measured from the chemical potential of the superconductors. Hence, the supercurrent has the form of Eq. (54). In practice, one does not necessarily measure $I_S(\phi)$, but the critical current $I_C = \max_\phi I_S(\phi)$. In diffusive junctions, this is obtained typically for ϕ near $\pi/2$, although the maximum point depends slightly on temperature.

The problem in SNS thermometry is in the fact that the supercurrent spectrum $j_S(\varepsilon)$ depends on the quality of the interface, on the specific geometry of the system, and most importantly, on the distance L between the two superconductors compared to the superconducting coherence length $\xi_0 = \sqrt{\hbar D / (2\Delta)}$ (Heikkilä *et al.*, 2002). Therefore, $I_C(T)$ dependence is not universal. However, the size of the junction can be tuned to meet the specific temperature range of interest. In the limit of short junctions, $L \lesssim \xi_0$ (Kulik and Omel'yanchuk, 1978), the temperature scale for the critical current is given by the superconducting energy gap Δ and for $k_B T \ll \Delta$, the supercurrent depends very weakly on the temperature. In a typical case $\xi_0 \sim 100 \dots 200$ nm, and thus already a weak link with L of the order of $1 \mu\text{m}$, easily realisable by standard lithography techniques, lies in the "long" limit. There, the critical current is $I_C = c(k_B T)^{3/2} \exp(-\sqrt{2\pi k_B T / E_T}) / (eR_N \sqrt{E_T})$

(Zaikin and Zharkov, 1981). This equation is valid for $k_B T \gtrsim 5E_T$. Here $E_T = \hbar D / L^2$ and the prefactor c depends on the geometry (Heikkilä *et al.*, 2002), for example for a two-probe configuration $c = 64\sqrt{2\pi^3} / (3 + 2\sqrt{2})$. The exponential temperature dependence and the crossover between the long- and short-junction limits were experimentally investigated by Dubos *et al.* (2001) and the above theoretical predictions were confirmed.

Using a four-probe configuration with SNS junctions of different lengths, Jiang *et al.* (2003) exploited the strong temperature dependence of the supercurrent to measure the local temperature. The device worked in the regime where part of the junctions were in the supercurrent-carrying state and part of them in the dissipative state. In the limit where supercurrent is completely suppressed, there is still a weaker temperature dependence of the conductance, due to the proximity-effect correction (c.f., Eq. (46)) (Charlat *et al.*, 1996). This can also be used for thermometry (Aumentado *et al.*, 1999), but due to the much smaller effect of temperature on the conductance, it is less sensitive.

Besides being just a thermometer of the electron gas, critical current of a SNS Josephson junction has been shown to probe the electron energy distribution (Baselmans *et al.*, 1999, 2001b; Giazotto *et al.*, 2004b; Huang *et al.*, 2002) as indicated by Eq. (56).

B. Coulomb blockade thermometer, CBT

Single electron tunnelling (SET) effects were foreseen in micro-lithographic structures in the middle of 1980's (Averin and Likharev, 1986). Such effects in granular structures had been known to exist already much earlier (Giaever and Zeller, 1968; Lambe and Jaklevic, 1969; Neugebauer and Webb, 1962). The first lithographic SET device was demonstrated by Fulton and Dolan (1987). Since that time SET effects have formed a strong subfield in mesoscopic physics. Typically SET devices operate in the full Coulomb blockade regime, where temperature is so low that its influence on electrical transport characteristics can be neglected; at low bias voltages current is blocked due to the charging energy of single electrons. Coulomb blockade thermometer (CBT) operates in a different regime, where single electron effects still play a role but temperature predominantly influences the electrical transport characteristics (Bergsten *et al.*, 2001; Farhangfar *et al.*, 1997; Meschke *et al.*, 2004; Pekola *et al.*, 1994). CBT is a primary thermometer, whose operation is based on competition between thermal energy $k_B T$ at temperature T , electrostatic energy eV at bias voltage V , and charging energy due to extra or missing individual electrons with unit of charging energy $E_C = e^2 / (2C^*)$, where C^* is the effective capacitance of the system. Figure 12 shows an SEM micrograph of a part of a typical CBT sensor suitable for the temperature range $0.02 \dots 1$ K. This sensor consists of four parallel one-dimensional arrays with 40

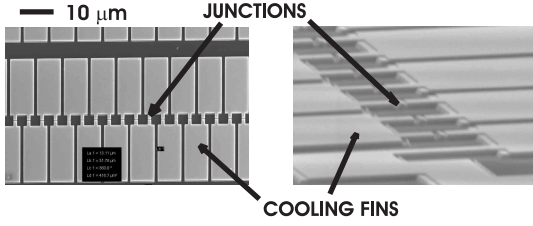


FIG. 12 A typical CBT sensor for the temperature range 20 mK - 1 K. The structure has been fabricated by electron beam lithography, combined with aluminium and copper vacuum evaporation. Both top view and a view at an oblique angle are shown; the scale indicated refers to the top view. Figure adapted from (Meschke *et al.*, 2004).

junctions in each.

In the partial Coulomb blockade regime the $I-V$ characteristics of a CBT array with N junctions in series do not display a sharp Coulomb blockade gap, but, instead, they are smeared over a bias range $eV \sim Nk_B T$. The asymptotes of the $I-V$ at large positive and negative voltages have, however, the same offsets as at low T , determined by the Coulomb gap. In the partial Coulomb blockade regime it is convenient to measure not the $I-V$ directly, but the differential conductance, i.e., the slope of the $I-V$ curve, $G \equiv dI/dV$, vs. V . The result is a nearly bell shaped dip in conductance around zero bias. Figure 13 illustrates a measured conductance curve, scaled by asymptotic conductance G_T at large positive and negative voltages. The important property of this characteristic is that the full width of this dip at half minimum, $V_{1/2}$, approximately proportional to T , determines the temperature without any fit, or any material or geometry dependent parameters, i.e., it is a primary measure of temperature. In the lowest order in $\frac{E_C}{k_B T}$, one finds for the symmetric linear array of N junctions of capacitance C in series (Farhangfar *et al.*, 1997; Pekola *et al.*, 1994)

$$G(V)/G_T = 1 - \frac{E_C}{k_B T} g\left(\frac{eV}{Nk_B T}\right). \quad (57)$$

For such an array $C^* = NC/[2(N-1)]$ and $g(x) = [x \sinh(x) - 4 \sinh^2(x/2)]/[8 \sinh^4(x/2)]$. The full width at half minimum of the conductance dip has the value

$$V_{1/2} \simeq 5.439 N k_B T / e, \quad (58)$$

which allows one to determine T without calibration.

It is often convenient to make use of the secondary mode of CBT, in which one measures the depth of the dip, $\Delta G/G_T$, which is proportional to the inverse temperature, again in the lowest order in $\frac{E_C}{k_B T}$:

$$\Delta G/G_T = E_C / (6k_B T). \quad (59)$$

Measuring the inflection point of the conductance curve provides an alternative means to determine T without calibration. In (Bergsten *et al.*, 2001) this technique

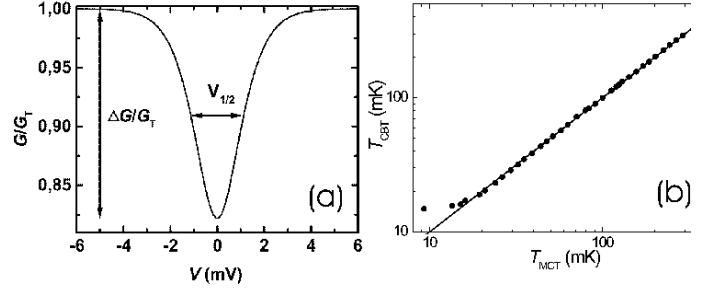


FIG. 13 Performance of a CBT thermometer. (a) Typical measurement: $G(V)/G_T$ is the differential conductance scaled by its asymptotic value at large positive and negative voltages, plotted as a function of bias voltage V . $V_{1/2}$ indicates the full width at half minimum of the characteristics, which is the main thermometric parameter. The full depth of the line, $\Delta G/G_T$, is another parameter to determine temperature. In (b) temperature deduced by CBT has been compared to that obtained by a ^3He melting curve thermometer. Saturation of CBT below 20 mK indicates typical thermal decoupling between electrons and phonons. Figure from Ref. (Meschke *et al.*, 2004).

was used for fast thermometry on two dimensional junction arrays. A simple and fast alternative measurement of CBT can be achieved by detecting the third harmonic current in a pure AC voltage biased configuration (Meschke *et al.*, 2005).

There are corrections to results (57), (58) and (59) due to both next order terms in $E_C/k_B T$ and due to non-uniformities in the array (Farhangfar *et al.*, 1997). Higher order corrections do sustain the primary nature of CBT, which implies wider temperature range of operation. The primary nature of the conductance curve exhibited by Eq. (57) through the bias dependence $g(\frac{eV}{Nk_B T})$ is preserved also irrespective of the capacitances of the array, even if they would not be equal. Only a non-uniform distribution of tunnel resistances leads to a deviation from the basic result of bias dependence of Eq. (57). Fortunately the influence of the inhomogeneity on temperature reading is quite weak, and it leads typically to less than 1 % systematic error in T .

The useful temperature range of a CBT array is limited at high temperature by the vanishing signal ($\Delta G/G_T \propto T^{-1}$). In practice the dip must be deeper than ~ 0.1 % to be resolvable from the background. The low temperature end of the useful temperature range is set by the appearance of charge sensitivity of the device, i.e., the background charges start to influence the characteristics of the thermometer. This happens when $\Delta G/G_T \simeq 0.5$ (Farhangfar *et al.*, 1997). With these conditions it is obvious that the dynamic range of one CBT sensor spans about two decades in temperature.

The absolute temperature range of CBT techniques is presently mainly limited by materials issues. At high temperatures, the measuring bias range gets wider, $V_{1/2} \propto T$, and the conductance becomes bias dependent

also due to the finite (energy) height of the tunnel barrier (Gloos *et al.*, 2000; Simmons, 1963a). Because of this, the present high temperature limit of CBTs is several tens of K. The (absolute) low temperature end of the CBT technique is determined by self-heating due to biasing the device. One can measure temperatures reliably down to about 20 mK at present with better than 1 % absolute accuracy in the range 0.05...4 K, and about 3 % down to 20 mK (Meschke *et al.*, 2004).

Immunity to magnetic field is a desired but rare property among thermometers. For instance, resistance thermometers have usually strong magnetoresistance. Therefore one could expect CBT to be also "magnetoresistive". On the contrary, CBT has proven to be immune to even the strongest magnetic fields (> 20 T) (van der Linden and Behnia, 2004; Pekola *et al.*, 2002, 1998). This happens because CBT operation is based on electrostatic properties: tunnelling rates are determined by charging energies. Hence, CBT should be perfectly immune to magnetic field as long as energies of electrons with up and down spins do not split appreciably, which is always the case in experiments.

Coulomb blockade is also a suitable probe of non-equilibrium energy distributions as demonstrated by Anthore *et al.* (2003).

C. Shot noise thermometer, SNT

Noise current or voltage of a resistor (resistance R) has been known to yield absolute temperature since 1920's (Blanter and Büttiker, 2000; Johnson, 1928; Nyquist, 1928). Till very recently only equilibrium noise, i.e., noise across an unbiased resistor, was employed to measure temperature. In this case Johnson noise voltage v_n and current i_n squared have expectation values $\langle v_n^2 \rangle = R^2 \langle i_n^2 \rangle = 4k_B T R \Delta f$, where Δf is the frequency band of the measurement. In other words, the current spectral density is given by $S_I = 4k_B T / R$, and voltage spectral density by $S_V = 4k_B T R$. There are several critical issues in measuring temperature through Johnson noise. First, the bandwidth has to be known exactly. Secondly, the small signal has to be amplified, and the gain must be known to high accuracy. Thirdly, the noise signal becomes extremely small at cryogenic temperatures, which in turn means that the measurement has to be able to detect a very small current or voltage, and at the same time no other noise sources should cause comparable voltages or currents.

Success in noise thermometry depends critically on the performance of the amplifiers used to detect the tiny noise current (or voltage). Constant progress in improving SQUIDS (Superconducting Quantum Interference Device) and in optimizing their operation has pushed the lowest temperature measurable by a Johnson noise thermometer down to below 1 mK (Lusher *et al.*, 2001).

It is not only the equilibrium noise that can be useful in thermometry. In the opposite limit, at $eV \gg k_B T$, the

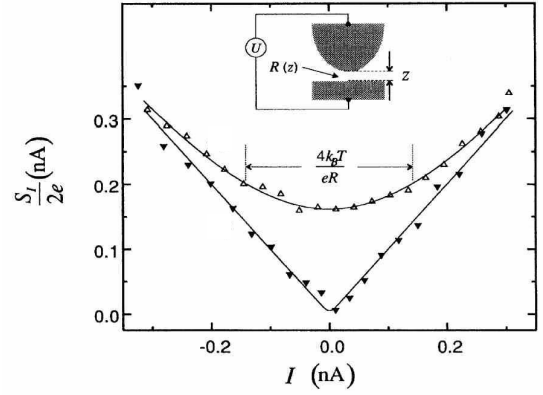


FIG. 14 Cross-over from Johnson noise to shot noise when increasing the bias voltage of a tunnel junction. The data shown by open symbols has been measured at 300 K with $R_T = 0.32$ G Ω , and data shown by solid symbols at 77 K with $R_T = 2.7$ G Ω . Adapted from (Birk *et al.*, 1995).

dominating noise, e.g., in tunnel junctions, is shot noise (Blanter and Büttiker, 2000; Schottky, 1918), whose current spectral density is given asymptotically by $S_I = F 2e|I|$. Fano factor F equals 1 for a tunnel junction. The way Johnson noise transforms into shot noise upon increasing the bias obeys the relation (see Eq. (34a) with $T_n \rightarrow 0$, and, e.g., (van der Ziel, 1986))

$$S_I(T) = 2eI \coth\left(\frac{eV}{2k_B T}\right). \quad (60)$$

At $|V| \gg k_B T / e$, Eq. (60) obtains the Poisson expression above, whereas at $|V| \ll k_B T / e$ it assumes the thermal Johnson form $S_I \simeq 4k_B T / R_T$.

Temperature dependent cross-over characteristics from Johnson to shot noise according to Eq. (60) have been demonstrated experimentally, e.g., in scanning tunnelling microscope experiments (Birk *et al.*, 1995) as shown in Fig. 14. Recently, Spietz *et al.* (2003) employed this cross-over in a lithographic tunnel junction between metallic films for thermometry (shot noise thermometer, SNT) in the temperature range from few tens of mK up to room temperature. At both ends of this range there are systematic errors in the reading, which can possibly be corrected by a more careful design of the sensor. In a rather wide range around 1 K (about 0.1...10 K), the absolute accuracy is better than 1 %. The crossover voltage depends only on $k_B T / e$, which means that the thermometer is indeed primary; ideally the temperature reading does not depend on the materials or geometry of the sensor. Figure 15 shows the experimental data of Spietz *et al.* (2003) at several temperatures: normalised (by Johnson noise) current noise has been plotted against normalised voltage $x \equiv eV / (2k_B T)$, whereby all curves at different temperatures should lie at $S_I^{\text{norm}} = x \coth(x)$. As seen in the bottom half of the figure, the residuals are smallest around 1 K.

As discussed above, noise measurements are difficult to

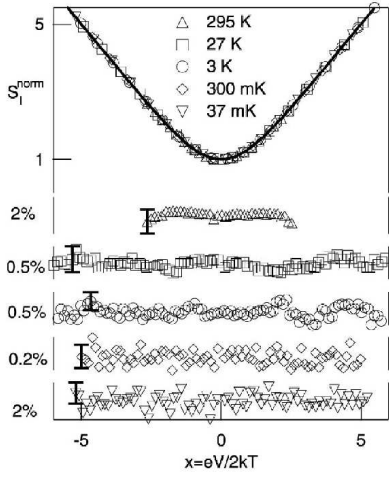


FIG. 15 Normalised junction noise versus normalised voltage at various temperatures. The residuals from the expected $x \coth(x)$ law are shown in the bottom half of the figure. From (Spietz *et al.*, 2003).

perform especially at low temperature where signal gets very small. At any temperature it is critically important to know the frequency window of the measurement and the gains in the amplifiers in Johnson noise thermometry. Yet the SNT avoids some of these problems. It is based on the cross-over between two noise mechanisms, both of which represent white noise, whereby the frequency window is ideally not a concern, since the same readout system is used in all the bias regimes. Moreover, the gains of the amplifiers are not that critical either because of the same argument. One can also use relatively high bandwidth which increases the absolute noise signal to be measured, and thereby makes the measurement faster.

The SNT technique has a few further attractive features. It is likely that its operation can be easily extended up to higher temperatures despite the deviations observed in the first experiments. The sensor consists of just one, relatively large size tunnel junction, which means that it is easy to fabricate with high precision. Also it is likely, although not yet demonstrated, that the SNT is not sensitive to magnetic field, since its operation is based on tunnelling characteristics in a NIN tunnel junction as in CBT.

Finally, noise measurements can in principle be used to measure the distribution function in non-equilibrium as well, as proposed by Pistolessi *et al.* (2004).

D. Thermometry based on the temperature dependent conductance of planar tunnel junctions

The effect of temperature on the current across a tunnel barrier with finite height is a suitable basis for thermometry in a wide temperature range (Gloos *et al.*, 2000). Simmons (1963a) showed that the tunnelling conductance at zero bias across a thin insulating barrier de-

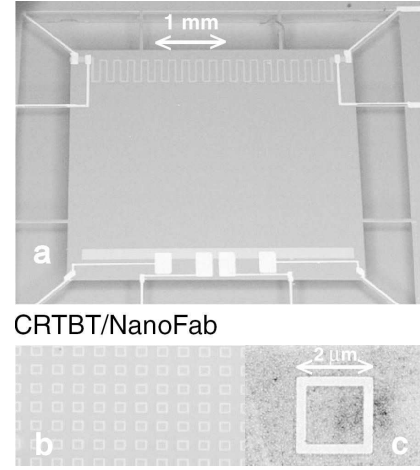


FIG. 16 The suspended thermal sensor employed in (Bourgeois *et al.*, 2005). The $\text{Nb}_x\text{N}_{1-x}$ thermometer can be seen in the lower part of the rectangular silicon membrane. The 450 000 Al superconducting rings are located in the middle part of the membrane; examples of them are shown in (b) and (c). Figure from (Bourgeois *et al.*, 2005).

pends on temperature as

$$G(T) = G_0[1 + (T/T_0)^2], \quad (61)$$

where G_0 is the temperature independent part of conductance and the scaling temperature T_0 depends on the barrier height ϕ_0 . For a rectangular barrier of width s one has $T_0^2 = \frac{3\hbar^2\phi_0}{\pi^2k_B^2ms^2}$, where m is the effective mass of the electrons within the insulating barrier. Experiments over a temperature range from 50 K up to 400 K on Al-AlOx-Al tunnel junctions have demonstrated that Eq. (61) is obeyed remarkably well (Gloos *et al.*, 2000; Suoknuuti *et al.*, 2001). Moreover, in these measurements the scaling temperature was found to be $T_0 \simeq 720$ K in all samples, without a clear dependence on the specific (zero temperature) conductance of the barrier, which varied over three orders of magnitude from $3 \mu\text{S}/\mu\text{m}^2$ up to $3000 \mu\text{S}/\mu\text{m}^2$. This property makes the method attractive in wide range thermometry, and T_0 can indeed be considered as a material specific, but geometry and thickness independent parameter up to a certain accuracy.

E. Anderson-insulator thin film thermometry

As regards to temperature read-out of micro-calorimetric devices, resistive thin film thermometers near the metal-insulator transition (MIT) are relatively popular. Electrical resistivity properties on both sides of the MIT are rather well understood (Belitz and Kirkpatrick, 1994), and in general resistance of such thin films shows strong temperature dependence, suitable for thermometry and in particular for calorimetry. On the insulator side resistivity ρ is determined by

hopping, and it has typically $\rho \propto e^{(T_0/T)^n}$ temperature dependence, with T_0 and n constants. On the metallic side, weaker dependence can be found. In practice, both $\text{Nb}_x\text{Si}_{1-x}$ (Denlinger *et al.*, 1994; Marnieros *et al.*, 1999, 2000) and $\text{Nb}_x\text{N}_{1-x}$ (Bourgeois *et al.*, 2005; Fominaya *et al.*, 1997) thin film based thermometers have been successfully employed. The suitable conduction regime can be tailored by adjusting x (x') in electron beam co-evaporation (Denlinger *et al.*, 1994) or in dc magnetron sputtering of Nb in a nitrogen atmosphere (Fominaya *et al.*, 1997).

Bolometric and calorimetric radiation detectors are discussed in detail in Sec. IV. Here we briefly mention the application of a $\text{Nb}_x\text{N}_{1-x}$ thermometer in a measurement of the heat capacity of 450 000 superconducting thin film loops on a silicon membrane (Bourgeois *et al.*, 2005), see Fig. 16. The heat capacity of the loops is proportional to their total mass, which was about 80 ng in this case. Vortices entering simultaneously into the 450 000 loops under application of magnetic field could be observed. A similar measurement (Lindell *et al.*, 2000), employing a NIS thermometer could resolve the specific heat jump at T_c of 14 thin film titanium disks with total mass of 1 ng on a silicon nitride membrane.

IV. THERMAL DETECTORS AND THEIR CHARACTERISTICS

The absorption of electromagnetic radiation by matter almost always ends in the situation where the incident optical power has, possibly via cascades of different physical processes, transformed into aggravated random motion of lattice ions, i.e. into heat. Here lies the fundamental principle behind the thermal detection of radiation: the transformation of the input electromagnetic energy to heat. In many cases, this state of maximum entropy has lost all the coherent properties that the incident radiation might have possessed, but yet there is information in this messy final state of the system: the rise in the system temperature. In this section, we give a short overview of thermal detectors, their theory and operation, and discuss some examples of thermal detectors and their applications.

There is a very small difference between thermometry and bolometry, the thermal radiation detection. Yet thermometry often implies measurement of temperature changes over a large fractional temperature range, whereas in the typical bolometric application, the observed temperature variations are extremely small. This allows us in the following to concentrate on the limit of small temperature changes around some mean well-defined value, i.e., we assume the operation in the quasiequilibrium regime (see Sec. II). In essence, bolometry is really high-precision thermometry, nothing more, with the added ingredient of finding efficient ways of coupling incident radiation to the device.

Although thermal detectors have developed enormous

diversity since their introduction in 1880 by Samuel P. Langley, and major advances in the way the temperature rise is measured and the detectors are constructed have been made, the basic principle remains the same. The operating principle of a thermal detector can be traced back to the generalized thermal model, shown in Fig. 1. The four main parts of a thermal detector are a thermally isolated element, a thermal link with a thermal conductance G_{th} (here G_{e-ph} or G_{ph-sub}), a thermal sensing element (i.e., a thermometer), and a coupling structure (e.g., an impedance matching structure for electromagnetic radiation) that serves to maximize the absorption of the incident radiation, be it in the forms of alpha particles or microwaves.

A. Effect of operating temperature on the performance of thermal detectors

Regardless of the exact architecture of the thermal detector, lowering the operating temperature will improve the performance significantly. This fact introduces the cooling techniques to the use of thermal detectors. Because of the diversity of the technological approaches it is hard to summarize the effect of the operating temperature in a fully universal fashion. However, some general trends can be evaluated. The figure of merit for thermal detectors is the noise equivalent power (NEP), which relates to the signal to noise ratio by $\text{SNR} = \dot{Q}_{\text{opt}} / (\text{NEP} \sqrt{2\tau_{\text{int}}})$, where \dot{Q}_{opt} is the incident optical power and τ_{int} is the post-detection integration time. The limiting NEP for an optimized thermal detector is given by the thermal fluctuation noise (TFN) arising from random fluctuations of energy across the thermal link with a thermal conductance $G_{\text{th}} \equiv d\dot{Q}/dT$ which result in variations in the temperature of the device (see also discussion in Subs. II.E.2). The TFN limited noise equivalent power (NEP) in the linear order is given by the fluctuation-dissipation result (Mather, 1982)

$$\text{NEP}_{\text{TFN}} \approx \sqrt{4k_{\text{B}}T^2G_{\text{th}}} \begin{cases} \propto T^3 & \text{e-p decoupling} \\ \propto T^{5/2} & \text{lattice isolation} \end{cases} \quad (62)$$

with the two cases relating the temperature dependence to the location of the thermal bottleneck. The expression for the lattice isolated case is generally valid at temperatures $T \lesssim \theta_{\text{D}}/10$ with θ_{D} the Debye temperature of the insulating material. The temperature T is the highest of the temperatures present in the system, i.e., the temperature of the thermally isolated element or that of the heat sink.

Refrigeration, combined with the advances in nanolithography techniques have recently opened a whole new realm for the application of electron-phonon decoupling to improve the thermal isolation of bolometric detectors. The operation of these so-called hot electron devices is usually limited to low (< 1 K) temperatures and very small thermally active volumes \mathcal{V} as the TFN

between the electron gas and the lattice is given by $\sqrt{5k_B\Sigma_{e-p}\mathcal{V}(T_e^6 + T_{ph}^6)}$ (Golwala *et al.*, 1997) where Σ varies between 1-4 nW/ $\mu\text{m}^3/\text{K}^5$ in metals (See Table I). The use of the lattice for the thermal isolation lends itself to operation over much broader temperature range as the geometry of the thermal link can be used to increase the thermal resistance.

Typically, the bath temperatures of cryogenic thermal detectors are centered around four temperature ranges: 4.2 K, the boiling temperature of liquid He at 1 atm, around 300 mK a temperature attainable with ^3He sorption refrigerators, around 100 mK, easily attainable using a compact adiabatic demagnetization refrigerator (ADR), or below ~ 50 mK, when a dilution refrigerator is used. In the recent years, the use of electronic refrigeration has become appealing with the development of the SINIS coolers. These coolers could enable the operation of thermal detectors at a much lower temperature than is 'apparent' to the user. For instance, the ^3He sorption coolers are quite attracting due to their compactness, low cost and simple operation. Used together with a SINIS cooler would allow for an affordable cryogenic detector system without having to sacrifice in performance.

Since the thermal fluctuation noise in a thermal detector is proportional to $T_e^n + T_{ph}^n$, maximum performance improvement is achieved by the reduction of the bath temperature (Anghel *et al.*, 2001). Modest performance increase is possible with direct electronic cooling, such as is the case in many of the SINIS bolometer experiments.

In addition to improved noise performance, direct coupling of a SINIS cooler to a thermal detector could allow for increasing the dynamic range of for example bolometers based on transition edge sensors (TES): A SINIS cooler can be used to draw a constant power from a TES that would otherwise saturate due to an optical load.

B. Bolometers: Continuous excitation

Thermal detectors that are used to detect variations in the incident flux of photons or particles are called bolometers (from the Greek word *bolē* - beam). This condition is generally met when the mean time between incident quanta of energy that arrive at the detector is much shorter than the recovery time of the bolometer³. The bolometric operating principle is very simple: Change $\Delta\dot{Q}_{\text{opt}}$ in the incident optical power creates a change in the temperature of a thermally isolated element by $\Delta T = \Delta\dot{Q}_{\text{opt}}/G_{\text{th}}$. A sensitive thermometer is used to measure this temperature change. The recovery time τ_0 is determined by the heat capacity C of the bolometer, and the thermal conductance G_{th} with $\tau_0 = C/G_{\text{th}}$, analogously to an electrical RC circuit.

Bolometric detectors remain popular today, 125 years after their first introduction. Probably the most important advantage of thermal detectors is their versatility: Bolometers can detect radiation from α -particles to radio waves, their dynamic range can be easily adapted for a variety of signal or background levels. As an extreme example, bolometers have been used to detect infrared radiation from nuclear fireballs (Stubbs and Phillips, 1960), and the cosmic microwave background. (Lamarre *et al.*, 2003).

In the early days, bolometers typically utilized hand-crafted construction (dental floss, cigarette paper and balsa wood are examples of typical materials used in the construction) (Davis *et al.*, 1964). If detecting electromagnetic waves, typically the absorber consisted of a metal with a suitable thickness yielding a square resistance of 377 Ω , i.e. matching the impedance of the vacuum. Further improvements on matching were achieved by placing the bolometer in a resonant cavity. One major setback with bolometers in their early days was unavoidably slow speed, caused by the large heat capacity resulting from the macroscopic size of the components used. The dawn of modern microfabrication techniques has all but eliminated this shortcoming, with bolometers of high sensitivity achieving time constants as short as a few hundred nanoseconds.

Today, the most common type of cryogenic resistive bolometers utilize transition edge sensors for the thermometry. In a TES bolometer, a superconducting film with a critical temperature T_c is biased within its superconductor - normal metal transition where small changes in the film temperature result to changes in the current through the device (or the voltage across the film). In most cases, the TES consists of two or more sandwiched superconductor-normal metal layers. The relative thicknesses of the S and N layers are used to tune the transition temperature to a desirable value by the proximity effect.

Transition-edge sensors are by no means a novel type of a thermal detector, as first suggestions for their use came out already in the late thirties (Andrews, 1938; Goetz, 1939), and first experimental results by 1941 (Andrews, 1941). Two principal problems prohibited the wide use of this type of thermal detectors for some fifty years: Typically the normal-state resistance of the superconducting films was too low in order to obtain adequate noise matching with field effect transistor (FET) preamplifiers, and the lack of good transimpedance amplifiers usually required the films to be current biased with a voltage readout. This introduced a requirement to tune the heat bath temperature very accurately within the narrow range of temperatures in the superconducting transition. This also made the devices exceedingly sensitive to small variations in the bath temperature, introducing stringent requirements for the heat bath stability.

These limitations can be overcome by the use of an external negative feedback circuit that maintains the film within its transition temperature and above the

³ The opposite (calorimetric) limit will be discussed in section IV.C

bath temperature. Such an approach was adopted by Clarke *et al.* (1977), who were able to demonstrate $\text{NEP} = 1.7 \cdot 10^{-15} \text{ W}/\sqrt{\text{Hz}}$ at an operating temperature of 1.27 K, using a transformer-coupled FET as the voltage readout. Introducing a negative feedback has similar advantages as in the case of operational amplifiers: linearity is improved, sensitivity to internal parameters of the amplifier (or bolometer) is reduced, and the speed is increased. Interestingly, the use of an external negative feedback in conjunction with superconducting transition edge sensors never found widespread use, possibly due to the (slightly) more complicated read-out architecture, and the need for a matching transformer.

The breakthrough of TESs came in 1995, when superconducting quantum interference device (SQUID) ammeters, which are inherently well suited in matching to low load impedances, were introduced as the readout devices for TESs (Irwin, 1995; Irwin *et al.*, 1995a). This allowed for the use of voltage biasing, which introduces strong negative electrothermal feedback (ETF) that causes the thermally isolated film to self-regulate within its superconducting transition. The local nature of the ETF makes the operation of these detectors very simple as no external regulation is necessary. As with an external negative feedback, an important advantage of the voltage biased TES is the fact that once the bath temperature is below $\sim T_c/2$, the need for bath temperature regulation is significantly relaxed. Finally, the increased speed due to the strong negative ETF increases the bandwidth of the detector, allowing for either detecting faster signal changes in a bolometer, or higher count rates in a calorimeter. A comprehensive review of the theory and operation of voltage biased TESs has been recently published (Irwin and Hilton, 2005).

The behaviour of thermal detectors is generally well understood. In the following discussion we shall summarize the main results for the theory of thermal detectors. The results are quite generally applicable to any resistive bolometers, but the treatment is geared towards voltage biased TES, firstly as they are currently the most popular type of thermal detectors, and secondly because the electrothermal effects are very prominent in these devices, having a major impact on the device speed and linearity.

We start by writing the equation governing the thermal circuit (here we limit the discussion to a simple case of one thermal resistance and heat capacity). Generally, the power flow to the heat sink is given by $\dot{Q}_{\text{out}} = K(T^n - T_0^n)$, where K is a constant which depends on materials parameters and the geometry of the link. The time dependence of the bolometer temperature can be solved from the heat equation for a bolometer with a bias point resistance of $R = V/I$ absorbing a time-varying optical signal $\dot{Q}_{\text{opt}}(t) = \dot{Q}_o e^{i\omega t}$ (c.f., Eq. (23)):

$$C \frac{d(\delta T e^{i\omega t})}{dt} + K(T^n - T_0^n) + G_{\text{th}} \delta T = \dot{Q}_{\text{bias}} + \dot{Q}_o e^{i\omega t} + \frac{d\dot{Q}_{\text{bias}}}{dT} \delta T, \quad (63)$$

where δT is used to denote the temperature change due to the signal power and \dot{Q}_{bias} describes the incoming heat flow due to the detector bias. Equating the steady state components of the equation yields $\dot{Q}_{\text{bias}} = K(T^n - T_0^n)$, from which one can obtain the result for the average operating temperature of the bolometer, given by $T = \dot{Q}_{\text{bias}}/\bar{G}_{\text{th}} + T_0$ where an average thermal conductance \bar{G}_{th} is defined by $\bar{G}_{\text{th}} = K(T^n - T_0^n)/(T - T_0) = \dot{Q}_{\text{bias}}/[(\dot{Q}_{\text{bias}}/K + T_0^n)^{1/n} - T_0]$.

The electrothermal feedback manifests itself through the fact that the change in input signal power modifies the bias dissipation, an effect described by the last term in Eq. (63). Taking a closer look at the temperature change we obtain

$$\delta T = \frac{\dot{Q}_o}{G_{\text{th}} + i\omega C - d\dot{Q}_{\text{bias}}/dT} \quad (64)$$

where $G_{\text{th}} = d\dot{Q}_{\text{out}}/dT \approx nKT^{n-1}$ is the dynamic thermal conductance. Now, considering the electrothermal term

$$\frac{d\dot{Q}_{\text{bias}}}{dT} = -\frac{\dot{Q}_{\text{bias}}\alpha}{T}\beta(\omega), \quad (65)$$

where $\alpha = d \log R / d \log T$ describes the sensitivity of the detector resistance to the temperature changes and $\beta(\omega) \equiv [R - Z_S(\omega)]/[R + Z_S(\omega)]$ is the effect of the bias circuit (with an embedding impedance of Z_S) on the ETF. Taking into account the thermal cut-off of the bolometer, the frequency-dependent loop gain is defined as

$$\mathcal{L}(\omega) \equiv \mathcal{L}_0 \frac{\beta(\omega)}{\sqrt{1 + \omega^2 \tau_0^2}}, \quad (66)$$

where $\mathcal{L}_0 \equiv \dot{Q}_{\text{bias}}\alpha/(G_{\text{th}}T)$ and $\tau_0 = C/G_{\text{th}}$ is the intrinsic thermal time constant of the bolometer. The electrothermal loop gain describes the effect of varying incident optical power to the bias power dissipated in the detector. For positive bolometers with $\alpha > 0$ the loop gain is positive for current bias (since $\text{Re}[\beta(\omega)] > 0$) and negative for voltage bias (as $\text{Re}[\beta(\omega)] < 0$). For bolometers with a negative temperature coefficient of resistance the situation is reversed. For metallic bolometers operated at room temperature $\alpha \sim 1$ and the loop gain is typically small ($\mathcal{L}_0 \lesssim 1$) so that the role of ETF is negligible. On the contrary, superconducting detectors with $\alpha \sim 100$ and G_{th} some three orders of magnitude smaller than for room temperature devices can have large loop gain ($\mathcal{L}_0 \gtrsim 50$), so that ETF plays a significant role in the detector characteristics. A major impact of negative ETF is that the bolometer time constant is reduced from τ_0 to $\tau_{\text{eff}} = \tau_0/[1 + \beta(0)\mathcal{L}_0]$. This reduction in the time constant is one of the major benefits of strong negative ETF.

Voltage biasing conditions are typically reached by driving a constant current I_0 through a parallel combination of the bolometer and a load resistor Z_S . As

long as $Z_S \ll R$, the bolometer is effectively voltage biased. The responsivity of a voltage biased bolometer can be derived as follows: The current responsivity is defined as $\mathcal{R}_I \equiv dI/d\dot{Q}_o$. Using Eqs. (64), (65) and (66), $V = I_0 Z_S R / (Z_S + R)$, and $I = I_0 Z_S / (Z_S + R)$, the result for the current responsivity becomes

$$\mathcal{R}_I(\omega) = -\frac{1}{V} \frac{(1 + \beta) \mathcal{L}_0}{2(1 + \beta \mathcal{L}_0)} \frac{1}{\sqrt{1 + \omega^2 \tau_{\text{eff}}^2}}. \quad (67)$$

In the limiting case at $\omega = 0$ with $\beta = 1$ (perfect voltage bias) and $\mathcal{L}_0 \gg 1$,

$$\mathcal{R}_I(0) = -\frac{1}{V}. \quad (68)$$

In order to evaluate the NEP for a bolometer, a discussion on the noise sources in bolometers is merited. In general, the NEP, noise spectral density S , and responsivity are related by $\text{NEP} = \sqrt{S_{V,I}} / |\mathcal{R}_{V,I}|$, where the subscripts refer to voltage or current noise and responsivity, respectively. The noise in bolometers is due to several uncorrelated sources. The most important of them is the thermal fluctuation noise, mentioned already above. Generally, this contribution is given by

$$\text{NEP}_{\text{TFN}} = \sqrt{4\gamma k_B T_c^2 G_{\text{th}}}. \quad (69)$$

Here γ describes the effect of the temperature gradient across the thermal link between the sensor and the heat sink (Mather, 1982) in the diffusive limit (i.e., no ballistic heat transport present) as

$$\gamma = \frac{(b+1) \left(T_c^{b+3} - T_c^{-b} T_0^{3+2b} \right)}{(3+2b) T_c^2 \left(T_c^{b+1} - T_0^{b+1} \right)} \xrightarrow{T_c \gg T_0} \frac{b+1}{2b+3}. \quad (70)$$

Here we assumed that the thermal conductivities obey $\kappa \propto T^b$. For resistive bolometers, another important contribution to the NEP is due to the Johnson noise, given by

$$\text{NEP}_J = \sqrt{\frac{4k_B T_c}{R}} \frac{V}{\mathcal{L}_0} \sqrt{1 + \omega^2 \tau_0^2}. \quad (71)$$

In addition to these noise sources, the current noise of the amplifier, $S_{i_{\text{in,amp}}}$, adds a contribution $\text{NEP}_{\text{amp}} = \sqrt{S_{i_{\text{in,amp}}}} / \mathcal{R}_I$. The total NEP of a bolometer is then

$$\begin{aligned} \text{NEP}_{\text{tot}}^2 = & \text{NEP}_{\text{TFN}}^2 + \text{NEP}_J^2 \\ & + \text{NEP}_{\text{amp}}^2 + \text{NEP}_{\text{excess}}^2, \end{aligned} \quad (72)$$

where the slightly ambiguous contribution $\text{NEP}_{\text{excess}}$ encompasses various contributions from additional external and internal noise sources. Typical excess external noise contributions arise from heat bath temperature fluctuations and pickup in the cabling to name a few. In addition to the external excessive noise, it has in recent years become clear that there are also internal noise sources that

are not fully accounted for. For instance, TESs with significant internal thermal resistance can no longer be treated using the simple lumped element model, and they suffer from internal thermal fluctuation noise (ITFN), adding a contribution (Hoevers *et al.*, 2000)

$$\text{NEP}_{\text{ITFN}} = \sqrt{\frac{4k_B T R}{L_0}} G_{\text{th}} \sqrt{1 + \omega^2 \tau_0^2}, \quad (73)$$

where L_0 is the Lorenz number.

For some devices, these noise sources are sufficient to explain all the observed noise. However, many groups are developing X-ray microcalorimeters (see below) which are often operated at a small fraction of the normal state resistance exhibit noise that increases rapidly as the bias point resistance is decreased, and has a significant influence on the performance of the detectors. Several possible explanations have been put forth, e.g., noise arising from the fluctuations in magnetic domains or phase-slip lines (Knoedler, 1983; Wollman *et al.*, 1997). A systematic study of the excess noise in different TES geometries has been published recently (Ullom *et al.*, 2004), showing that there exists a clear correlation between α and the observed excess noise, with the magnitude of the excess noise scaling roughly as $0.2\sqrt{\alpha}$. A quantitative agreement with the measured excess noise spectrum has so far been achieved in one experiment (Luukanen *et al.*, 2003), where the TES consisted of an annular (so called Corbino) geometry with a superconducting center contact, and a concentric current return at the outer perimeter of the annular TES. This geometry results in strictly radial current flow, enabling a simple analytical expression for the current density in the TES. The $1/r$ dependence in the current density together with a small radial temperature gradient causes the TES to separate to two annular superconducting and normal state regions.

For any system undergoing a second order phase transition, order parameter fluctuations will take place. The excess noise arises from the thermally driven fluctuation of the phase boundary which manifest as resistance fluctuations. The volume associated with the order parameter fluctuation can be obtained by noting that the Ginzburg-Landau free energy δF associated with the fluctuation is $\delta F \sim k_B T_c$. As the TES is biased towards smaller R , the relative contribution of the order parameter fluctuations becomes larger until it fully dominates over the other noise contributions. For the Corbino-geometry TES, the contribution due to the fluctuation superconductivity noise (FSN) to the NEP is

$$\text{NEP}_{\text{FSN}} = \frac{0.24 L_0 T_c^2 G}{V^2 \alpha} \Gamma \sqrt{1 + \omega^2 \tau_0^2}, \quad (74)$$

where $\Gamma \approx 10^{-8} \text{ K}/\sqrt{\text{Hz}}$ is a constant dependent on the TES parameters.

So far, this noise model has not successfully been applied to TESs in the more conventional square geometry, mainly due to the fact that the current distribution

varies with bias point and is not easily calculable. A solution could be obtained by solving the full 2D Ginzburg-Landau equations for a square geometry.

1. Hot electron bolometers

In principle, modern bolometers can be artificially divided into two major sub-classes depending on where the dominant thermal bottleneck lies. The so-called hot-electron bolometers (HEBs) utilize the decoupling of the electron gas in a metal or a semiconductor from the phonon heat bath. The earliest HEBs were based on InSb, where the weak coupling of the electrons to the lattice at temperatures around 4 K allows the electrons to be heated to a temperature significantly above that of the lattice even in a bulk sample. Mobility in InSb is limited by ionized impurity scattering which results in decreasing resistivity with an increasing electric field. This is the basis of the detection mechanism (Brown, 1984; Rollin, 1961). Often HEBs have sufficient speed for mixing, and in fact HEB mixers are a current topic of considerable interest. Most HEB mixers operate at 4 K, and in order to maintain our focus on phenomena and devices at temperatures below 1 K, we unfortunately will not discuss them within this review.

HEB direct detectors (Ali *et al.*, 2003; Karasik *et al.*, 2003; Richards, 1994) have been a subject of considerable interest, but in general a full optical demonstration remains to be carried out. The attractive features of such devices include very short time constant (well below 1 μ s), potentially very good NEP performance (below 10^{-19} W/ $\sqrt{\text{Hz}}$ when operated at or below 0.3 K), and simple construction that does not require surface micromachining steps. The architecture is essentially very similar to that of the HEB mixers: a small superconducting TES film coupled to the feed of a lithographic antenna. The application of the SQUID readout scheme utilized in typical hot phonon microbolometers and microcalorimeters might not be as straightforward as one could expect as the introduction of the SQUID input coil inductance to the voltage biasing circuit can make the system unstable due to the interaction of the poles of the electrical circuit and the thermal circuit. The approximate criterion for the stability of a voltage biased TES is that the effective time constant of the TES should be about one order of magnitude longer than the electrical time constant of the bias circuit (Irwin *et al.*, 1998).

A hot-electron bolometer that has been demonstrated is based on electron thermometry with NIS junctions (Nahum and Martinis, 1993, 1995). Here the incident optical power elevates the electron temperature in a small normal metal island weakly thermally coupled to the lattice phonons, and the change in the electron temperature can be sensed as a change in the tunneling current (see Subs. III.A.1). Noise equivalent powers below 10^{-19} W/ $\sqrt{\text{Hz}}$ have been predicted (Kuzmin, 2004) but remain to be experimentally verified. An additional at-

tractive feature of the SINIS bolometer is that a DC bias on the device can be used to refrigerate the electrons to a temperature below that of the bath temperature (see Subs. V.C.1). Another benefit over TESs is the fact that the SINIS bolometer saturates much more gently compared to the TESs, which basically have no response at all once the device is overheated above T_c . The self-cooling property of the SINIS bolometer can also be used to compensate for excessive background loading, thus effectively giving it a larger dynamic range. The main obstacle towards constructing large arrays of (SI)NIS based HEBs is that their impedance (typically 1 k Ω - 100 k Ω) is hard to match to the existing cryogenic SQUID multiplexers (Chervenak *et al.*, 1999; de Korte *et al.*, 2003; Lanting *et al.*, 2005; Reintsema *et al.*, 2003; Yoon *et al.*, 2001). In principle, one could apply superconducting transformers to match the SQUID noise, but transformers with sufficient impedance transformation range are quite large, which makes this approach unpractical. A novel readout method that lends itself for array readouts is a microwave reflectometric measurement, in which the SINIS bolometer is connected in series with a tuning inductor (Schmidt *et al.*, 2003, 2004b). The LC resonance frequency of the inductor and the stray capacitance of the junctions is tuned to fall within the bandwidth of the cryogenic microwave amplifier (400-600 MHz), facilitating good impedance match. The dynamic resistance of the device is highly sensitive to the electron temperature, and thus temperature changes cause modulation of Q of the resonance circuit. This modulation is sensed by sending a small RF signal to the resonant circuit, and measuring the reflected power. The electrical NEP inferred from noise measurements was in these experiments 1.6×10^{-17} W/ $\sqrt{\text{Hz}}$.

2. Hot phonon bolometers

The second major class of bolometers are hot phonon bolometers (HPBs). They rely on a geometrical design of the heat link G_{geom} so that the thermal bottleneck lies between two phonon populations. This approach is the most common, and allows for operation at temperatures up to and beyond room temperature. The earliest and most widely used of the contemporary HPBs are the so-called spider-web bolometers (Mauskopf *et al.*, 1997), operated at 300 mK and below, where a free-standing Si_3N_4 mesh is used to support a thermal sensing element. Narrow Si_3N_4 legs provide the thermal isolation for the mesh. Before the introduction of TESs and SQUIDs the thermometer of choice was a small crystal of neutron-transmuted (NTD) Ge due to its relatively high temperature coefficient of resistance ($d \log R / d \log T|_{T=0.3\text{K}} \approx -6$) and large resistance (~ 25 M Ω) that allowed for good noise matching with FET preamplifiers. On the other hand this made the devices very microphonic. Efficient optical coupling was possible since radiation at wavelengths smaller than the

mesh period are absorbed to a resistive film deposited on the Si_3N_4 mesh. An example of a spider-web bolometer using a NTD Ge is shown in Fig. 17. Later versions of the spider-web bolometers have adopted the use of TES as thermometers, coupled to a SQUID readout (Gildemeister *et al.*, 1999).

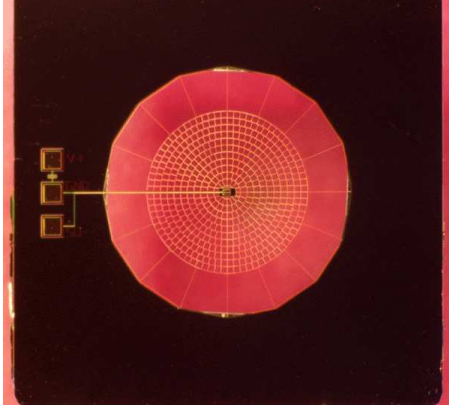


FIG. 17 (Color in online edition): A micrograph of a "spider-web" bolometer. A NTD Ge thermistor is located at the centre of the web. Image courtesy of NASA/JPL-Caltech.

Alternatively to the spider-web absorber, a $\lambda/4$ resonant cavity can be used to maximize the optical efficiency over a limited bandwidth. The SCUBA-2 instrument (Duncan *et al.*, 2003; Holland *et al.*, 2003) on the James Clerk Maxwell telescope is an ambitious undertaking with a pixel count of over 12 000. The bolometers consist of thermally isolated, $(1 \text{ mm}^2) \times 60 \text{ nm}$ silicon 'bricks' with the front surface of the Si degenerately doped with phosphorous to 377Ω per square. The resonant cavity is formed by the Si in between the doped layer, and a Mo-Cu TES deposited to the back side of the pixel.

Even though the superconducting TES thermometers are becoming increasingly popular, bolometers utilizing lithographic semiconducting thermistors still yield impressive performance and are more forgiving in terms of the saturation power. In the so-called pop-up bolometers, a lithographic, doped Si is used as the thermistor, while an ingenious torsional bending method of the Si_3N_4 legs is used to bend the legs and wiring layers perpendicular to the absorbers. This architecture enables the construction of arrays with a very high filling factor (Voellmer *et al.*, 2003). Another promising lithographic resistive thermometer technology is based on thin films of NbSi (Camus *et al.*, 2000). The high resistivity of these films allows for impedance levels that provide a good noise matching to room temperature JFET amplifiers.

Instead of the surface absorbing approach, another method is based on the use of a lithographic antenna (Hwang *et al.*, 1979; Neikirk *et al.*, 1983), and terminating the induced currents to a thermally isolated bolometer, an approach often used in the HEB mixers discussed above. The attractive feature of this method is that

the thermally sensing volume can be made much smaller compared to the case of the surface-absorbing bolometers, making these devices much faster. The low heat capacity often allows for lower NEP, as in many cases the NEP_{TFN} is limited by the maximum time constant $\tau_{\text{max}} = C/G_{\text{th,min}}$ allowed by the application. In this case $\text{NEP}_{\text{TFN}} = \sqrt{4\gamma k_B T^2 C / \tau_{\text{max}}}$. Moreover, the small size of the thermally sensitive volume makes it far less sensitive to out of band stray light, relaxing filtering and baffling requirements of the incoming radiation. Antenna coupling also lends itself to the construction of integrated, on-chip filters for defining the bands for an array of bolometers (Hunt *et al.*, 2003; Mees *et al.*, 1991; Myers *et al.*, 2005). Arrays of antenna-coupled bolometers can also utilize the inherent polarization selectivity of the antennas. An example of an antenna-coupled TES bolometer that incorporates on-chip transmission line impedance transformers and band-pass filters is shown in Fig. 18. No NEPs have yet been measured on this device, but the expected NEP is $\sim 10^{-16} \text{ W}/\sqrt{\text{Hz}}$ for a device with $T_c = 450 \text{ mK}$.

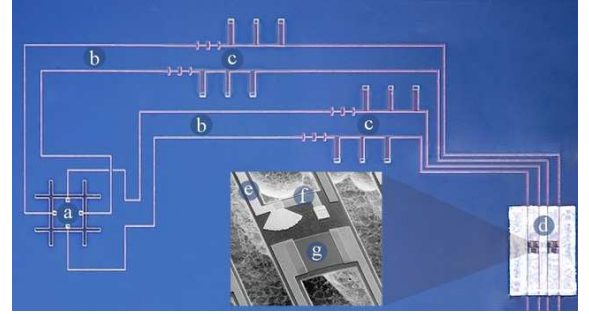


FIG. 18 (Color in online edition): Micrograph of an antenna-coupled TES bolometer. A dual-polarized double-slot antenna (a) is coupled via microstrip transmission lines (b) with band-pass and low-pass filters (c) to two Al/Ti bilayer TES thermometers located on suspended Si_3N_4 membranes (d). The inset shows in detail the termination of the microstrip line (e) to a resistor (f), and the Al/Ti TES (g). Figure courtesy A. T. Lee, UC Berkeley.

While not published yet, the best performance of an antenna-coupled HPB utilizing a similar design has been obtained by the JPL-Caltech bolometer group, with an electrical $\text{NEP} = 5 \cdot 10^{-19} \text{ W}/\sqrt{\text{Hz}}$ at 230 mK (Kenyon, 2005). The architecture is shown in Fig. 19.

In the simplest case, the bolometer is simply a strip of metal placed to the feed of the lithographic antenna. Although this approach is by far the simplest, it introduces limitations for the performance of a HPB: Unlike in the case of HEB mixers, maximizing the thermal isolation of the bolometer is always desirable. However, the bolometer resistance should be matched to the impedance of the antenna (typically $\sim 100 \Omega$ for broadband lithographic antennas on Si substrates), and thus the thermal conductance to the bath through the antenna, G_{ant} , is fixed by the Wiedemann-Franz law, $G_{\text{ant}} = L_0 T / \text{Re}(Z_a)$, where

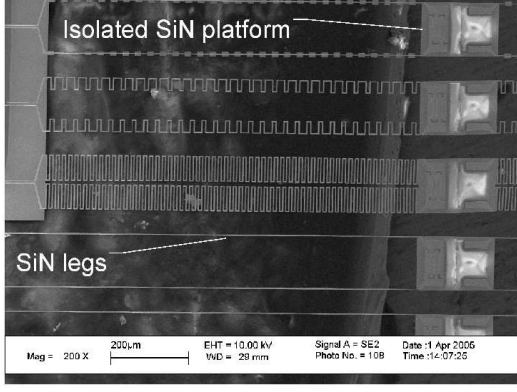


FIG. 19 SEM micrograph of an isolated Si_3N_4 platforms with Mo/Au TESs. As an extreme example of thermal isolation, the meandering Si_3N_4 legs have an aspect ratio of $\sim 2800:1$, yielding a thermal conductance $G_{\text{th}} \approx 100 \text{ fW/K}$ at a bath temperature of 210 mK. Figure courtesy M.E. Kenyon, JPL.

Z_a is the antenna impedance. A parallel heat loss path is to the substrate below the bolometer film, with conductance $G_{\text{sub}} \propto LW$ where L and W are the length and width of the bolometer film, respectively. For substrate mounted antenna-coupled HPBs it is thus beneficial to minimize the size of the bolometer. This requirement can be relaxed if the bolometer strip is released from the underlying substrate to form an air-bridge (Neikirk and Rutledge, 1984). For air-bridged devices at temperatures higher than 4 K, $\text{NEP}_{\text{TFN}} \propto T^{3/2}$. Recently, an air-bridge bolometer operating at 4.2 K was demonstrated, showing potential for background-limited performance when observing 300 K blackbodies (Luukanen *et al.*, 2005; Luukanen and Pekola, 2003). The potential applications for these devices include passive detection of concealed weapons under clothing, remote trace detection, and terrestrial submillimetre-wave imaging.

C. Calorimeters: Pulsed excitation

In the limit opposite to the bolometric detection, i.e. when the mean time between the quanta of energy arriving at the detector exceeds the device relaxation time, thermal detectors are known as calorimeters. While the topic of calorimetry also encompasses heat capacity measurements especially in mesoscopic samples, the following discussion concentrates on the detection of radiation only in order to keep the scope of our review in reasonable limits. For those interested in microcalorimetry in the sense of heat capacity measurements, we direct the reader to references (Bourgeois *et al.*, 2005; Denlinger *et al.*, 1994; Fominaya *et al.*, 1997; Lindell *et al.*, 2000) and (Marnieros *et al.*, 1999).

Cryogenic calorimeters are used today in a large va-

riety of applications, from the detection of weakly interacting massive particles (WIMPs) in dark matter search (Akerib *et al.*, 2003; Bravin *et al.*, 1999), X-ray (de Korte *et al.*, 2004; Kelley *et al.*, 1999; Moseley *et al.*, 1984) and γ -ray (van den Berg *et al.*, 2000) astrophysics to secure optical communications (Miller *et al.*, 2003; Nam *et al.*, 2004). As is the case with bolometers, calorimeters are usually operated at temperatures below 1 K. The theory and operation of calorimetric thermal detectors is very similar to bolometers, and generally the theoretical treatment above is valid. However, the optimization of calorimetric detectors can be quite different. The quantum of energy E deposited by either a photon, charged particle, WIMP etc. can be determined from the temperature rise $\Delta T = E/C$, where C is the heat capacity of the calorimeter. This temperature rise then decays exponentially with a time constant τ_{eff} to its equilibrium value. Thermometry in the calorimeters is most often done either using semiconducting or TES thermometers, as is the case with bolometers. In addition, thermometry based on the change of magnetization of a paramagnetic sensor is appealing due to its non-dissipative nature, and has yielded some promising results (Fleischmann *et al.*, 2003; Schönefeld *et al.*, 2000).

The figure of merit for a calorimeter is the energy resolution, ΔE , of full-width at half-maximum (FWHM), related to NEP through (Moseley *et al.*, 1984)

$$\Delta E = 2\sqrt{2 \ln 2} \left(\int_0^\infty \frac{4}{\text{NEP}^2(f)_{\text{tot}}} df \right)^{-1/2} \approx 2\sqrt{2 \ln 2} \text{NEP}(0)_{\text{tot}} \sqrt{\tau_{\text{eff}}}, \quad (75)$$

For a 'classic' calorimeter with a white noise spectrum the energy resolution is in terms of the operating temperature and the heat capacity given by

$$\Delta E = 2\sqrt{2 \ln 2} \sqrt{k_B T^2 C}, \quad (76)$$

indicating that ΔE scales $\propto T^{5/2}$ or $\propto T^{3/2}$ depending whether the heat capacity of the sensor is dominated by the lattice or the electronic system, respectively.

In most of the devices under development today the lattice temperature is being measured, as sufficient cross section to the incoming energy often requires a rather large volume of a device. An exception to the norm are TES calorimeters optimized for optical single photon detection for applications in secure quantum key distribution (Nam *et al.*, 2004), shown in Fig. 20. In these devices, the thermal isolation is via electron-phonon decoupling. A trade-off is made between energy resolution and the speed of the detectors. Energy resolution of the detectors is sufficient to determine the photon-number state of the incoming photons, while maintaining a speed that is adequate for fast information transfer.

As with bolometers, the TESs currently outperform the competition in terms of the sensitivity. The best reported energy resolution for any energy dispersive detector was recently obtained with a Mo-Cu

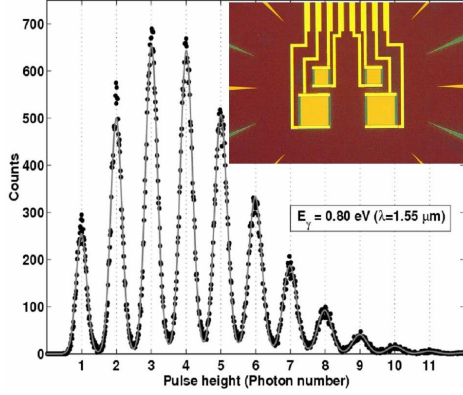


FIG. 20 (Color in online edition): The energy spectrum of a pulsed 1550 nm laser, measured with an optical TES microcalorimeter. The peaks in the plot correspond to the photon-number state of the incoming pulses. The inset shows a micrograph of the devices. Figure courtesy of A.J. Miller, NIST.

calorimeter (see Fig. 21), yielding an energy resolution of 2.38 ± 0.11 eV at a photon energy of 5.89 keV (Irwin and Hilton, 2005). The driving application in

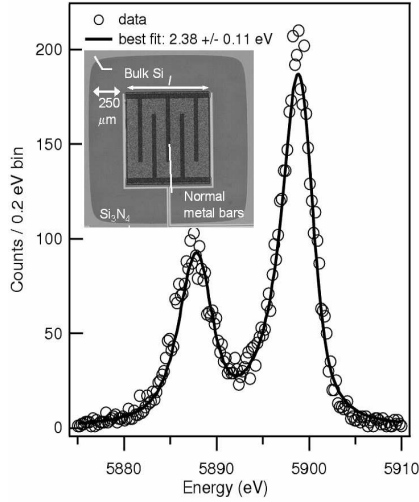


FIG. 21 An energy spectrum of the ^{55}Mn K_α complex, obtained with a Mo/Cu TES microcalorimeter. The width of the measured characteristic x-ray lines is a convolution of the intrinsic x-ray linewidth and the gaussian detector contribution with a FWHM of 2.38 ± 0.11 eV. The TES is fabricated on a free-standing Si_3N_4 membrane. The inset shows a SEM micrograph of the TES. The normal metal bars extending partially across the TES have been experimentally verified to improve the energy resolution of the detector (Ullom *et al.*, 2004). Figure courtesy of J. Ullom, NIST.

the development of X-ray microcalorimeters are two major X-ray astrophysics missions planned by the European Space Agency (ESA) and the U.S. National Aeronautics and Space Administration (NASA). Both missions, *X-ray Evolving Universe Spectroscopy (XEU)*

(The European Space Agency, 2005) mission and the *Constellation-X* mission (NASA, 2005) will employ X-ray microcalorimeters as their primary instrument. The energy resolution of the state of the art microcalorimeters have already reached the requirements stated in the science goals for these missions. Thus, the current primary focus of the technical research is on the development of large arrays of microcalorimeters, and more importantly, SQUID multiplexing read-outs for the detector arrays. A prototype 5×5 array of Ti/Au TES microcalorimeters is shown in Fig. 22.

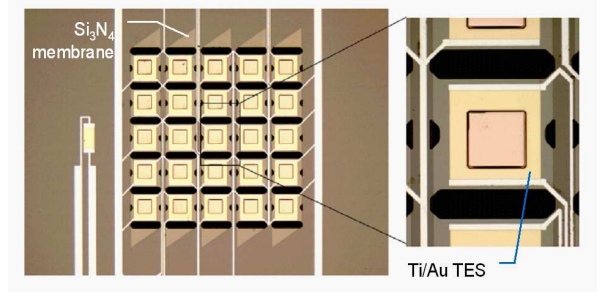


FIG. 22 (Color in online edition): A prototype Ti/Au microcalorimeter array. The dark regions within the Si_3N_4 membrane are holes in the membrane. Figure courtesy of SRON-MESA.

D. Future directions

While cryogenic thermal detectors are the most sensitive radiation detectors around, further significant performance increases are envisioned in the future. The push is from single pixels to large staring focal plane arrays of detectors for numerous astrophysics applications. For this reason, novel thermal detector concepts must be able to be integrated into large arrays.

The performance of hot electron bolometer mixers has been improving rapidly over the past years. Noise temperatures approaching $10 \times h\nu / (2k_B)$ are being reported, and the emphasis is in pushing the operating frequency deeper into the THz region. In principle, frequencies in the infrared range are not out of the question. Lithographic antennas have demonstrated good performance up to 30 THz (Grossman *et al.*, 1991), while it is clear that the fabrication becomes increasingly challenging as the required feature size is reduced.

In the single pixel direct detector development, the quest for ever better sensitivity is still ongoing. For bolometers, the improvement in NEP directly translates to the capability of observing over less pre-detection bandwidth without sacrificing signal to noise ratio. This would enable the construction of arrays capable of yielding spectroscopic information. It is here where the functions of HEB mixers, bolometers and calorimeters conjoin - in the capability of performing single photon spectrometry at far-infrared wavelengths.

V. ELECTRONIC REFRIGERATION

Thermoelectric effects and, in particular, thermoelectric cooling have been discovered more than 170 years ago (Peltier, 1834). During the last 40 years considerable progress has been made in developing practical thermoelectric refrigerators for industrial and scientific applications (Nolas *et al.*, 2001; Rowe and Bhandari, 1983). The temperature range of interest has been, however, far above cryogenic temperatures. Yet, during the last decade, solid state refrigerators for low temperature applications and, in particular, operating in the sub-kelvin temperature range have been intensively investigated. The motivations of this activity stem from the successful development and implementation of ultrasensitive radiation sensors and quantum circuits which require on-chip cooling (Pekola *et al.*, 2004b) for proper operation at cryogenic temperatures. Solid state refrigerators have typically lower efficiency as compared to more traditional systems (e.g., Joule-Thomson or Stirling gas-based refrigerators). By contrast, they are more reliable, cheaper and, what is more relevant, they can be easily scaled down to mesoscopic scale. All this gives a unique opportunity to combine on-chip refrigeration with different micro- and nanodevices.

The aim of this part of the review is to describe the existing solid state electron refrigerators operating at cryogenic temperatures (in particular below liquid helium temperature), and to give an overview of some novel ideas and refrigeration schemes.

A. General principles

The physical principle at the basis of thermoelectric cooling is that energy transfer is associated with quasi-particle electric current, as shown in Sec. II. Under suitable conditions thermal currents can be exploited for heat pumping, and if heat is transferred from a cold region to a hot region of the system, the device acts as a refrigerator. The term *refrigeration* is associated throughout this Review to a process of lowering the temperature of a system with respect to the ambient temperature, while *cooling*, in general, means just heat removal from the system. It is noteworthy to mention that the maximum cooling power of a refrigerator is achieved at a vanishing temperature gradient, while the maximum temperature difference is achieved at zero cooling power. The efficiency of a refrigerator is normally characterized by its coefficient of performance (η), i.e., the ratio between the refrigerator cooling power (\dot{Q}_{cooler}) and the total input power (P_{total}):

$$\eta = \frac{\dot{Q}_{cooler}}{P_{total}}. \quad (77)$$

Irreversible processes (e.g., thermal conductivity and Joule heating) degrade the efficiency of refrigerators, and

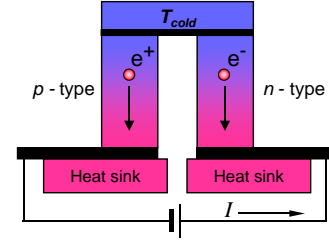


FIG. 23 Basic Peltier thermoelement.

are essential elements that need to be carefully evaluated for the optimization of any device.

The basic principles of the design are in general similar for different types of refrigerators. The increase of temperature gradient can be achieved by realizing a multistage refrigerator. In this case, the stage operating at a higher temperature should be designed for larger cooling power in order to efficiently extract the heat released from the lower-temperature stage ("pyramid design"). The enhancement of the refrigerator cooling power can be achieved by connecting several refrigerators in parallel. The parallel design is more effective both for an efficient heat evacuation from the hotter regions of the device and for the application of higher electric currents to the refrigerator. It also allows more freedom to properly bias all cooling elements.

The temperature dependence of the electric and thermal properties of the active parts in the refrigerator may limit their exploitation at low temperatures. The reduction of thermal conductivity by lowering the temperature has both positive (better thermal insulation between cold and hot regions) and negative (difficulty in removing heat from the system) effects.

At cryogenic temperatures different types of superconductors can be efficiently exploited. They can be used both as *passive* and *active* elements: in the former case, owing to their low thermal conductivity and zero electric resistance (e.g., as one of the two arms in Peltier refrigerators), in the latter as materials with an energy gap in the density of states for energy-dependent electron tunneling (e.g., in NIS coolers).

Currently, the development of refrigerating techniques follows two main directions: search of new materials with improved characteristics suitable for existing refrigeration schemes, and development of new refrigeration methods and principles.

B. Peltier refrigerators

Thermoelectric (Peltier) refrigeration is widely used for cooling different electronic devices (Nolas *et al.*, 2001; Phelan *et al.*, 2002; Rowe and Bhandari, 1983). Nowadays Peltier refrigerators providing temperature reduction down to 100...200 K and cooling power up to 100 W are available. Peltier cooling (or heating) occurs

when an electric current is driven through the junction of two different materials. The heat released or absorbed, $\dot{Q}_{Peltier}$, depending on the direction of the electric current at the junction, is proportional to the electric current (I) driven through the circuit, $\dot{Q}_{Peltier} = \Pi_{AB}I$, where $\Pi_{AB} = \alpha_{AB}T$, and Π_{AB} and α_{AB} are the Peltier and Seebeck coefficients of the contact, respectively (see also Eq. (39)). In order to obtain enhanced values of the Peltier coefficient, conventional Peltier refrigerators generally consist of p - and n -type semiconductors with opposite sign of Π coefficients (see Fig. 23). The efficiency of a Peltier refrigerator is not determined only by the coefficient $\Pi_{AB} = \Pi_A - \Pi_B$, but also by thermal conductivities (κ) of both materials across the contact. Furthermore their electric resistances (ρ) are responsible of Joule heating affecting the coefficient of performance. The maximum temperature difference (ΔT_{max}) achievable with a Peltier refrigerator is given by (Nolas *et al.*, 2001) $\Delta T_{max} = ZT_{cold}^2/2$, where $Z = \frac{\alpha_{AB}^2}{\rho\kappa}$ is a figure of merit of the refrigerator, and T_{cold} is the temperature of the cold junction (see Fig. 23). More often, however, the refrigerator efficiency is characterized by the dimensionless figure of merit ZT . We recall that $ZT \propto (\frac{k_B T}{E_F})^2$. Most of the materials used in thermoelectric applications have $ZT \sim 1$ at room temperature (DiSalvo, 1999; Min and Rowe, 2000). In general, at low temperatures only one single thermoelectric material is needed, because a superconductor can be used as one of the two arms of the refrigerator (Goldsmid *et al.*, 1988; Nolas *et al.*, 2001).

In spite of the drastic reduction of cooling efficiency at low temperature, there is, however, some development of new materials and devices suitable for operation at cryogenic temperatures. Recently, Peltier cooling with $\Delta T_{max} \approx 0.2$ K was demonstrated below 10 K (Harutyunyan *et al.*, 2003) (see Fig. 24). Crystals of CeB_6 were used to exploit the strong thermoelectric coefficients arising from the Kondo effect. The dimensionless figure of merit of this material is 0.1...0.25 in the temperature range between 4 K and 10 K. The authors claim that a proper optimization of the refrigerator design would allow more than 10% temperature reduction below 4K with a single-stage refrigerator.

At millikelvin temperatures lattice specific heat and thermal conductivity decrease drastically, and thermoelectric refrigeration might become feasible. Following this idea and taking into account the Wiedemann-Franz relation, values of ZT as high as 20 at temperatures below 10 mK and the possibility to achieve thermoelectric refrigeration were predicted (Goldsmid and Gray, 1979; Nolas *et al.*, 2001).

Kapitulnik (1992) proposed to exploit a metal close to its metal-insulator transition for the implementation of a thermoelectric refrigerator operating below liquid-He temperatures. The basic concept behind this proposal is that near the metal-insulator transition, the transport coefficients acquire anomalous power laws such that their relevant combination describing the figure of merit for

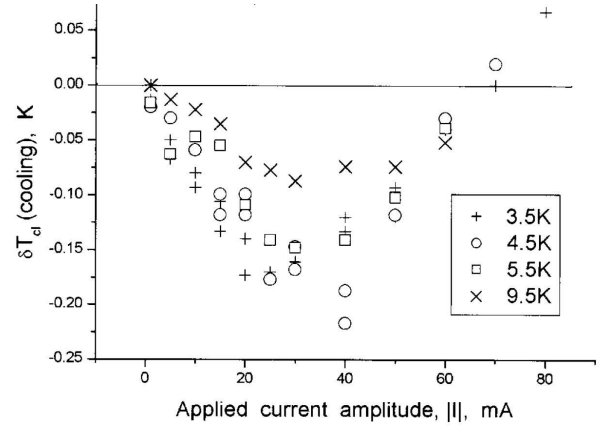


FIG. 24 Thermoelectric refrigeration at cryogenic temperatures using cerium hexaboride. Adapted from (Harutyunyan *et al.*, 2003).

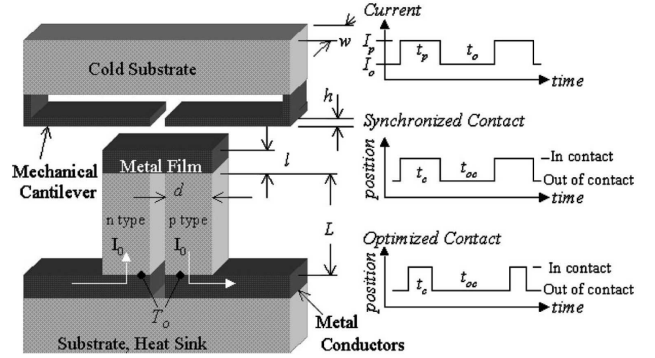


FIG. 25 Schematic diagram of the thermoelectromechanical cooler, time sequences of the pulsed current applied to the device, and the two modes of cantilever contact: synchronized and optimized (Miner *et al.*, 1999).

efficient cooling also becomes large.

Further improvement of the efficiency of conventional thermoelectric coolers could be, in principle, achieved through a thermoelectromechanical refrigerator (Miner *et al.*, 1999; Thonhauser *et al.*, 2004). In such a device, a periodic variation of the electric current through a Peltier element combined with a synchronized mechanical thermal switch would allow to improve the overall cooling performance (see Fig. 25). The enhancement of refrigeration is due to the spatial separation of the Peltier cooling and Joule heating.

The analysis of thermoelectric devices is usually based on the parameters typical of bulk materials. Significant progress in low temperature Peltier refrigeration might be achieved by using exotic materials (Goltsev *et al.*, 2003; Rontani and Sham, 2000) and low-dimensional structures (Balandin and Lazarenkova, 2003; DiSalvo, 1999; Hicks *et al.*, 1993), such as composite thin films, modulation-doped heterostructures, quantum wires, nan-

otubes, quantum dots, etc. These systems offer, in general, more degrees of freedom to optimize those quantities that affect the efficiency of thermoelectric refrigerators.

C. Superconducting electron refrigerators

1. (SI)NIS structures

Although heat transport in superconducting microstructures originally dates back more than 40 years ago in SIS junctions (Chi and Clarke, 1979; Gray, 1978; Melton *et al.*, 1981; Parmenter, 1961), it is instructive to start our description of this topic from NIS tunnel junction structures. Figure 26(a) shows the calculated \dot{Q} for a NIS tunnel junction (see Sec. II.G.2) versus bias voltage at different temperatures ($T = T_{e,N} = T_{e,S}$). When \dot{Q} is positive, it implies heat removal from the N electrode, i.e., *hot* excitations are transferred to the superconductor. For each temperature there is an optimal voltage that maximizes \dot{Q} and, by decreasing the temperature, the heat current results to be peaked around $V \simeq \Delta/e$. Figure 26(b) displays the heat current versus temperature calculated at each optimal bias voltage. The quantity $\dot{Q}(T)$ is maximized at $T \approx 0.25 \Delta/k_B = T_{opt}$ (as indicated by the arrow in the figure) where it reaches $\dot{Q} \simeq 6 \times 10^{-2} \Delta^2/e^2 R_T$, decreasing both at lower and higher temperatures. Also shown in the figure is $\dot{Q}(T)$ obtained assuming a temperature-independent energy gap. Such a comparison shows that this latter assumption is fully justified for $T \leq 0.2 \Delta/k_B$. In the low temperature limit ($T_{e,N} \leq T_{e,S} \ll \Delta/k_B$) it is possible to give an approximate expression (Anghel and Pekola, 2001) for the optimal bias voltage (V_{opt}), $V_{opt} \approx (\Delta - 0.66 k_B T_{e,N})/e$, as well as for the maximum cooling power at V_{opt} ,

$$\dot{Q}_{opt} \approx \frac{\Delta^2}{e^2 R_T} [0.59 (\frac{k_B T_{e,N}}{\Delta})^{3/2} - \sqrt{\frac{2\pi k_B T_{e,S}}{\Delta}} \exp(-\frac{\Delta}{k_B T_{e,S}})]. \quad (78)$$

Equation (78) is useful for getting quantitative estimates on the performance of realistic coolers. In the same temperature limit and for $V = V_{opt}$ the current through the NIS junction can be approximated as $I \approx 0.48 \frac{\Delta}{e R_T} \sqrt{\frac{k_B T_{e,N}}{\Delta}}$. The NIS junction coefficient of performance η is given by $\eta(V) = \dot{Q}(V)/[I(V)V]$. For $V \approx \Delta/e$ and in the low temperature limit, η thus obtains the approximate value

$$\eta_{opt} \approx 0.7 \frac{T_{e,N}}{T_c}, \quad (79)$$

where we assumed $\Delta = 1.764 k_B T_c$, and T_c is the critical temperature of the superconductor. Equation (79) shows that the efficiency of a NIS junction is around or below 20% at the typical operation temperatures. The full behavior of η versus temperature calculated at each optimal bias voltage is displayed in Fig. 26(c). The simple results presented above point out how the optimized operation of

a superconducting tunnel junction as a building block of microrefrigerators stems from a delicate balance among several factors such as the contact resistance, the operation temperature, the superconducting gap Δ as well as the bias voltage across the junction.

The first observation of heat extraction from a normal metal dates back to 1994 (Nahum *et al.*, 1994), where cooling of conduction electrons in Cu below the lattice temperature was demonstrated using an Al/Al₂O₃/Cu tunnel junction. A significant improvement was made two years later, still in the Al/Al₂O₃/Cu system, by Leivo *et al.* (1996), which recognized that using two NIS junctions in series and arranged in a symmetric configuration (i.e., in a SINIS fashion) leads to a much stronger cooling effect. This fact can be understood keeping in mind that \dot{Q} is a symmetric function of V so that, at fixed voltage across the structure, quasi-electrons above Δ are extracted from the N region through one junction, while at the same time quasi-holes are filled in N below $-\Delta$ from the other junction (see Fig. 26(d)). In this configuration, a reduction of the electron temperature from 300 mK to about 100 mK was obtained. Later on, several other experimental evidences of electron cooling in SINIS metallic structures were reported (Arutyunov *et al.*, 2000; Clark *et al.*, 2004; Fisher *et al.*,

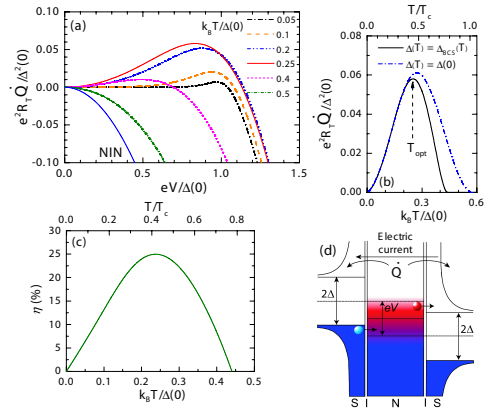


FIG. 26 Characteristics of (SI)NIS refrigerators. (a) Calculated cooling power \dot{Q} of a NIS junction vs bias voltage V for several temperatures $T = T_{e,N} = T_{e,S}$. Also shown is the behavior of a NIN junction. (b) \dot{Q} calculated at the optimal bias voltage as a function of temperature, assuming both a temperature-independent energy gap (dash-dotted blue line) and the real BCS dependence (black line). T_{opt} indicates the temperature value that maximizes \dot{Q} . (c) Coefficient of performance η calculated at the optimal bias voltage versus temperature. (d) Scheme of the energy band diagram of a voltage biased SINIS junction. The electric current flows into the normal region through one tunnel junction and out through the other, while the heat current \dot{Q} flows out of the N electrode through both tunnel junctions.

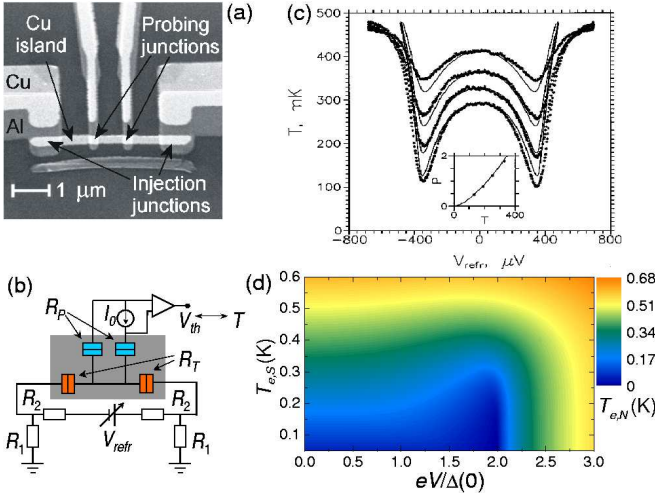


FIG. 27 SINIS refrigeration. (a) Scanning electron micrograph of a typical SINIS microrefrigerator. The structure was fabricated by standard electron beam lithography combined with Al and Cu UHV e-beam evaporation. The probe junction resistance usually satisfies the condition $R_p \gg R_T$ in order to prevent self-cooling. (b) Sketch of a typical measurement setup for electron cooling. (c) Electron temperature in the N region versus V_{refr} measured at different bath temperatures. Dots represent experimental data, while solid lines are theoretical fits. The inset shows the cooling power (pW) against temperature obtained from the fits (dots). (d) Contour plot of the theoretical electron temperature $T_{e,N}$ vs bias voltage V and $T_{e,S}$ for a SINIS cooler, assuming thermal load due to the electron-phonon interaction (see text). (a) is adapted from (Pekola *et al.*, 2004a); (c) from (Leivo *et al.*, 1996).

1995, 1999; Leivo *et al.*, 1997; Leoni *et al.*, 1999, 2003; Luukanen *et al.*, 2000; Pekola *et al.*, 2000a, 2004a, 2000b; Tarasov *et al.*, 2003; Vystavkin *et al.*, 1999). In these experiments NIS junctions are used to alter the electron temperature in the N region as well as to measure it. In order to measure the temperature, the N region is normally connected to additional NIS contacts (i.e., "probe" junctions) acting as thermometers (previously calibrated by varying the bath temperature of the cryostat), and operating along the lines described in Sec. III.A.1. Moreover, the differential conductance of the probe junctions gives also detailed information about the actual quasiparticle distribution function in the N region (Pekola *et al.*, 2004a; Pothier *et al.*, 1997b).

Figure 27(a) shows the SEM micrograph of a typical Al/Al₂O₃/Cu SINIS refrigerator including the superconducting probe junctions. The schematic of a commonly used experimental setup for electron refrigeration and temperature measurement is shown in Fig. 27(b). The voltage bias V_{refr} across the SINIS structure allows to change the electron temperature in the N region; at the same time, a measure of the voltage drop across the two probe junctions (V_{th}) at a constant bias current (I_0) yields the electron temperature $T_{e,N}$ in the

normal electrode (Rowell and Tsui, 1976). Figure 27(c) illustrates the experimental data of Leivo *et al.* (1996) of the measured electron temperature $T \equiv T_{e,N}$ versus V_{refr} , taken at different bath temperatures (i.e., those at $V_{refr} = 0$). As can be readily seen, the electron temperature rapidly decreases by increasing the voltage bias across the SINIS structure, reaching the lowest value around $V_{refr} \approx 2\Delta \simeq 360 \mu\text{eV}$ (note that now two junctions in series are involved in the process). Then, by further increasing the bias, the electron temperature rises due to the heat flux induced into the metal. Furthermore, the minimum electron temperature strongly depends on the starting bath temperature. The inset shows the extracted maximum cooling power (dots) that obtains values as high as 1.5 pW at $T = 300$ mK, corresponding to about 2 pW/ μm^2 (in the present experiment, sub-micron NIS junctions were exploited, with barrier resistances $R_T \simeq 1$ k Ω).

The general operation of a SINIS microrefrigerator like that shown in Fig. 27(a) can be understood by recalling that the final electron temperature in the N region stems from the balance among several factors that tend to drive power into the electron system (i.e., power losses), as discussed in detail in Sec. II. Most of metallic SINIS refrigerators fabricated so far operate in a regime where strong inelastic electron-electron interaction tends to drive the system into quasiequilibrium, where the electron system can be described by a Fermi function at a temperature $T_{e,N}$ that differs, in general, from that of the lattice (T_{ph}). At the cryogenic temperatures of interest (i.e., typically below 1 K), the dominant contribution comes from electron-phonon scattering that exchanges energy between electrons and the lattice phonons. The refrigerator cooling power (\dot{Q}_{refr}) can be defined as the maximum power load the (SI)NIS device can sustain while keeping the N region at temperature $T_{e,N}$, and can be generally expressed as

$$\dot{Q}_{refr} = 2\dot{Q}(V/2; T_{e,N}, T_{e,S}) - \dot{Q}_{e-ph}(T_{e,N}, T_{ph}), \quad (80)$$

where the factor 2 takes into account the presence of two identical NIS junctions, and it is often assumed that in the superconductors $T_{e,S} = T_{ph}$. The minimum temperature $T_{e,N}$ reached by the N metal thus fulfills the condition $\dot{Q}_{refr} = 0$. An example of $T_{e,N}$ versus V behavior along the lines of Eq. (80) is represented by the solid curves plotted in Fig. 27(c). Furthermore, any additional term that adds thermal load into the electron system can be properly taken into account by including its specific contribution to the right-hand side of Eq. (80) (Fisher *et al.*, 1999; Ullom and Fisher, 2000). Figure 27 (d) shows an example of the calculated electron temperature $T_{e,N}$ vs voltage and $T_{e,S}$ as obtained from the solution of Eq. (80), $\dot{Q}_{refr} = 0$. Here we considered a typical Al/Al₂O₃/Cu SINIS cooler with volume $\mathcal{V} = 0.15 \mu\text{m}^3$, $R_T = 1$ k Ω , $\Sigma = 2$ nW/ $\mu\text{m}^3\text{K}^5$ (Cu), and $T_{e,S} = T_{ph}$. As it can be readily seen, the $T_{e,N}$ value strongly depends on the bias voltage as well as on the lattice temperature. Depending on the thermal load due

to the electron-phonon interaction and the operating V , the SINIS device can thus behave as a cooler or as a refrigerator.

Let us now highlight some of the basic requirements of SINIS structures for *electron* cooling operation (their use for *lattice* cooling is addressed in Sec. V.C.6). In particular, the working temperature range of these structures depends mainly on the type of the superconductor (through its energy gap Δ and hence its critical temperature T_c), on the strength of the electron-phonon interaction Σ , on the junction resistance R_T , and on the N region volume \mathcal{V} . First of all, a reduction of the active volume to be cooled is the most straightforward method to increase the efficiency of the refrigeration process, this being more relevant at high lattice temperatures (according to the assumed T_{ph}^5 -dependence of electron-phonon interaction). In addition, cooling power maximization in the *high-temperature* regime (let us say 1...4.2 K) would require both to lower the electron-phonon coupling constant and to increase Δ through a proper choice of the superconductor. The first issue can be solved up to some extent with a variety of materials with different Σ (see Table I). As far as the second issue is concerned, there is a vast choice of superconducting metals with T_c covering the temperature range up to about 20 K (Kittel, 1996).

On the other hand, the question of junction resistance requires a careful discussion. In general, from Eq. (78), \dot{Q} enhancement is expected from a reduction of R_T . This latter issue can be accomplished both by making thinner barriers and by increasing the junction area. The first issue is not so straightforward, as already discussed in Subs. II.F.2, due to the intrinsic difficulty in fabricating high-quality low- R_c barriers, although optimized barriers are currently under investigation (see Sec. VI.F.1). Latter option was experimentally addressed by Fisher *et al.* (1999) in Al/Al₂O₃/Ag refrigerators, where large cooling powers of a few tens of pW were obtained with junctions of $20 \times 20 \mu\text{m}^2$ surface area. The reduction in electron temperature was, however, much inferior to that achievable with sub-micron sized junction. The problem intrinsic to junctions with large overlap (especially at the lowest temperatures) stems from the larger density of quasiparticles present in the superconductor, due to the fact that quasiparticles require a larger time to exit the junction region and escape from the superconductor. Therefore, this excess of quasiparticles alters in general the refrigerator performance by returning energy to the normal electrode, mainly due to back-tunneling from the superconductor as well as due to recombination processes, where phonons can enter and heat up the N region (Jochum *et al.*, 1998; Kaplan *et al.*, 1976; Ullom and Fisher, 2000). In addition, inelastic scattering with phonons and dynamic impurities can also lead to an excess of quasiparticles. These contributions can easily overcompensate the junction cooling power, so that it is crucial to remove this excess of quasiparticles from the superconductor. Toward this end a number of techniques exist among which we mention the exploitation

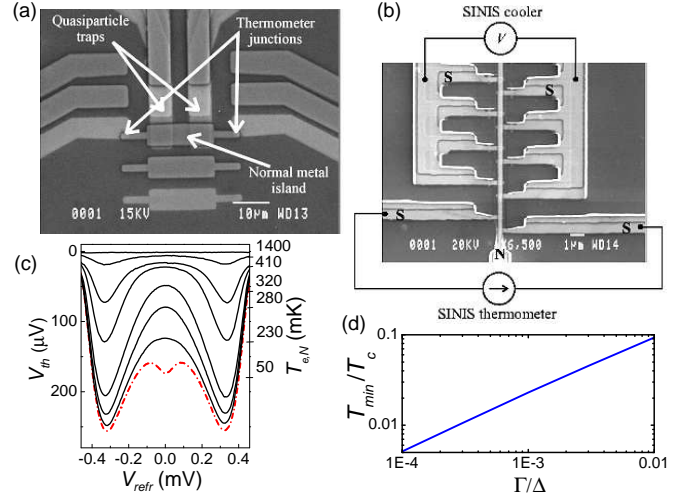


FIG. 28 Optimization of SINIS refrigerators. (a) SEM micrograph of an Al/Al₂O₃/Cu SINIS microrefrigerator exploiting large-area junctions ($\sim 10 \mu\text{m}^2$) with quasiparticle traps. (b) SEM image of a part of comb-like SINIS structure with 10+10 junctions for cooling and a SINIS thermometer. (c) Electron temperature $T_{e,N}$ in the N region of an Al/Al₂O₃Cu SINIS refrigerator versus V_{refr} measured at different bath temperatures. The lowest curve (red dash-dotted line) shows the anomalous heating effect observable at the lowest temperatures and attributed to the presence of quasiparticle states within the superconducting gap. (d) Theoretical ultimate minimum electron temperature of a SINIS cooler T_{min}/T_c at $V \simeq 2 \Delta/e$ versus Γ/Δ in quasiequilibrium. (a) is adapted from (Pekola *et al.*, 2000a); (b) from (Luukanen *et al.*, 2000); (c) and (d) from (Pekola *et al.*, 2004a).

of defect-free and thick S electrodes (that allow quasiparticles to escape *ballistically* from the junction area as well as to decrease their density near the barrier) and the exploitation of quasiparticle "traps" (Parmenter, 1961), i.e., normal metal films connected to the superconductor in the junction region through a tunnel barrier or in direct metallic contact (Irwin *et al.*, 1995b; Pekola *et al.*, 2000a) (see Fig. 28(a)). Such traps act as sinks of quasiparticles absorbing almost all the excess quasiparticle energy present in the superconductor, and have proved to efficiently help heat removal from the superconductor leading to a significant improvement of SINIS device cooling performance (Luukanen *et al.*, 2000; Pekola *et al.*, 2000a, 2004a). All these are commonly exploited tricks for the thermalization of the superconducting electrodes, and in these conditions, it is a reasonable approximation to set $T_{e,S} = T_{ph}$. Furthermore, the experiments (Pekola *et al.*, 2000a) demonstrated that the trap performance is in general superior when it is in direct metallic contact at short distance from the cooling junction (typically below $1 \mu\text{m}$, although the optimal distance mainly depends on the superconductor coherence length), nevertheless in small-area junctions even a contact through an insulating barrier seems sufficient for the purpose. The effectiveness of trapping in

SINIS structures was theoretically addressed in detail by Voutilainen *et al.* (2005) and Golubev and Vasenko (2002). Another possibility to achieve high cooling by maximizing the ratio of the junction area to the size of the region to be cooled is to use several small-area junctions (with size in the sub-micron range) connected in parallel to the N electrode (to limit the drawbacks typical of large junctions) (Arutyunov *et al.*, 2000; Leoni *et al.*, 1999; Luukanen *et al.*, 2000; Manninen *et al.*, 1999), as shown in Fig. 28(b).

The issue of tunnel junction *asymmetry* in SINIS refrigerators was addressed by Pekola *et al.* (2000b). This effect is fortunately weak: these authors theoretically showed that the maximum cooling power is reduced by 7% in the case the junction resistances differ by a factor of two, as compared to a symmetric structure with the same total junction area. Furthermore, the reduction is only about 25% even when the resistance ratio is four. This effect stems from the "self aligning" character of the double junction structure: the voltage drop across each junction is simultaneously close to Δ/e , thus corresponding to the maximum cooling power, when the voltage across the whole SINIS system is close to $2\Delta/e$. This fact is due to the high non-linearity of the current-voltage characteristics of the two junctions which carry the same current. The experiments have confirmed such a weak dependence of the cooling power on the structure asymmetry (Pekola *et al.*, 2000b).

In the *low-temperature* regime the situation is rather different. While power load from electron-phonon interaction becomes less and less dominant by decreasing the temperature, and typically below 0.1 K the cooler behavior can be described as if the lattice would not exist at all, other factors can limit the achievable cooling power as well as the lowest attainable electron temperature. First of all, at the lowest temperatures the maximum achievable cooling power of a NIS junction is intrinsically limited, given by $\dot{Q} \propto (e^2 R_T)^{-1} \Delta^{1/2} (k_B T_{e,N})^{3/2}$. Then non-idealities in the tunnel barriers, where the possible presence of Andreev-like transport channels (e.g., pin-holes) may strongly degrade the cooling power (in the high temperature regime this contribution is in general overcome by thermal activation) (Bardas and Averin, 1995). Furthermore, nonequilibrium effects in the N region as well in the S electrodes may be a limitation. In the N region, a suppression of the cooling power is expected by increasing the quasiparticle relaxation time (Frank and Krech, 1997), i.e., by driving the electron gas far from equilibrium. In the superconductors, a *non-thermal* distribution can alter the cooling response of the refrigeration process as well as the presence of hot quasiparticle excitations (like with large-area junctions) may be responsible of additional heat load into the N region. Yet, quasiparticle states within the superconducting gap represent a crucial problem at the lowest temperatures, yielding anomalous heating in the N region and limiting the achievable minimum temperature (Pekola *et al.*, 2004a). Such quasiparticle states, due mainly to inelastic

scattering in the superconductor (Dynes *et al.*, 1984) or to inverse proximity effect from the nearby N region, are generally taken into account by adding an imaginary part (Γ) to the superconductor DOS, as in Eq. (12). Figure 28(c) shows a representative set of cooling curves taken in an Al/Al₂O₃/Cu SINIS refrigerator at different lattice temperatures, where at the lowest temperature (red dash-dotted line) (this typically happens around or below $T_0 \approx 100$ mK) the electron gas first undergoes *heating*, then it is strongly cooled at the expected bias around $V_{refr} \simeq 2\Delta/e$. A similar anomaly was reported in some experiments on SINIS refrigerators (Fisher *et al.*, 1999; Pekola *et al.*, 2004a, 2000b; Savin *et al.*, 2001). The anomalous heating was attributed to the presence of such states within the S gap that give rise to a sort of *dissipative* channel which dominates heat current in a certain bias range (Pekola *et al.*, 2004a). Pekola *et al.* (2004a) theoretically demonstrated that the minimum achievable electron temperature (T_{min}) in SINIS refrigerators is set by the amount of quasiparticle states present within the superconducting gap, and is given by $T_{min}/T_c \simeq 2.5(\Gamma/\Delta)^{2/3}$ at $V_{refr} \simeq 2\Delta/e$ in quasiequilibrium (see Fig. 28(d)). We note that a measure of the Γ/Δ value in real NIS junctions is approximately given by the ratio of the zero-bias to the normal state junction conductance at low temperature. The existence of quasiparticle states within the superconducting gap thus sets a *fundamental* limit to the minimum achievable temperature, and great care has to be devoted to get rid of their presence to optimize the refrigeration process at the lowest temperatures.

2. S₁IS₂(IS₁) structures

The enhancement of superconductivity by quasiparticles extraction was proposed in 1961 by Parmenter (1961) in the context of S₁IS₂ tunnel junctions, where S₁ and S₂ represent superconductors with different energy gaps. Later on, Melton *et al.* (1981) theoretically discussed the possibility to exploit such a system to realize a refrigerator (addressing both the basic features and performance). From an experimental point of view, Chi and Clarke (1979) observed in Al films an enhancement of the energy gap of the order of 40% due to quasiparticle extraction. Then, Blamire *et al.* (1991), using Nb/AlO_x/Al/AlO_x/Nb structures, were able to obtain an enhancement of the critical temperature of the Al layer by more than 100%. The physical mechanism giving rise to this effect was discussed by Heslinga and Klapwijk (1993) and by Zaitsev (1992). More recently, also Nevirkovets (1997) observed in similar structures an enhancement of the Al gap by quasiparticle extraction.

Figure 29(a) shows the calculated heat current versus bias voltage for a S₁IS₂ tunnel junction at $T = T_{e,S1} = T_{e,S2} = 0.2 \Delta_1(0)/k_B$ for various Δ_2/Δ_1 ratios (see Eq. (30)). The quantity $\dot{Q}(V)$ is an even function of V , thus allowing connection of two junctions in a sym-

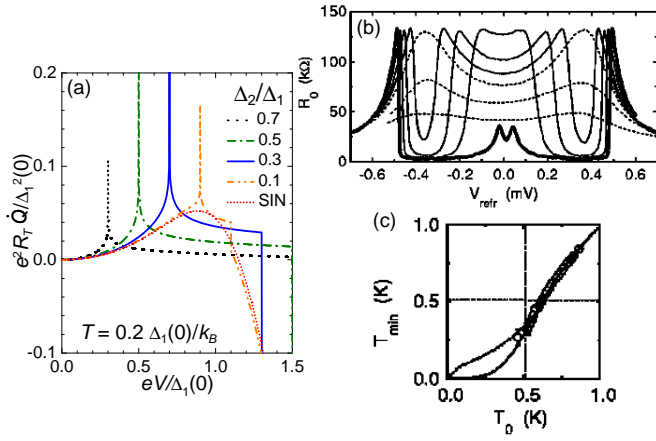


FIG. 29 $S_1IS_2(IS_1)$ refrigerator. (a) Calculated cooling power \dot{Q} of a S_1IS_2 junction vs bias voltage V at $T = T_{e,S1} = T_{e,S2} = 0.2 \Delta_1(0)/k_B$ for several Δ_2/Δ_1 ratios. Red-dotted line represents \dot{Q} when S_2 is in the normal state. (b) Measured cooling of a Ti island to and in the superconducting state by quasiparticle tunneling. R_0 is related to the electron temperature $T_{e,S2}$ in Ti (see text). Dashed lines: Ti is in the normal state. Thin solid lines: Ti is cooled from the normal to the superconducting state. Thick solid line: Ti is already superconducting at $V_{\text{refr}} = 0$. (c) Measured minimum electron temperature (T_{min}) of Ti versus bath temperature T_0 . (b) and (c) are adapted from (Manninen *et al.*, 1999).

metric configuration as in the NIS case, and is positive for $|V| < (\Delta_1(T) + \Delta_2(T))/e$ where *hot* quasiparticle excitations are removed from S_2 . Moreover, the heat current is maximized at $V = \pm(\Delta_1(T) - \Delta_2(T))/e$, where it is logarithmically diverging (Harris, 1974; Tinkham, 1996) (note that this is somewhat broadened by the smearing in the density of states in a realistic situation (Frank and Krech, 1997; Manninen *et al.*, 1999; Pekola *et al.*, 2004a)). From Fig. 29(a) it follows that heat extraction from S_2 only occurs if $\Delta_2(T) < \Delta_1(T)$ holds. Then, at $V = \pm(\Delta_1(T) + \Delta_2(T))/e$ a sharp transition brings $\dot{Q}(V)$ to negative values (more details about the heat transport in S_1IS_2 junctions can be found in (Frank and Krech, 1997)). The dotted line represents $\dot{Q}(V)$ when the electrode S_2 is in the normal state (i.e., NIS case). Notably, when both electrodes are in the superconducting state, $\dot{Q}(V)$ can *exceed* significantly that in the normal state. This peculiar characteristic of heat transport in S_1IS_2 junctions makes them promising in realizing a “cascade” refrigerator that might operate at bath temperatures higher than those for a SINIS cooler, where several combined superconducting stages are used to efficiently cool a normal or a superconducting region.

The experimental observation of electron cooling in a superconductor was reported by Manninen *et al.* (1999) using Al/insulator/Ti tunnel junctions. In this experiment, aluminum (i.e., the larger-gap superconductor) was used to cool the electron system of a Ti strip from $1.02 T_{c2}$ to below $0.7 T_{c2}$, where $T_{c2} = 0.51$ K was the Ti criti-

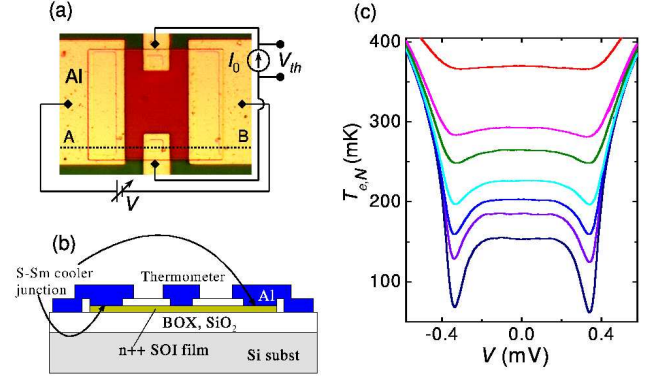


FIG. 30 Semiconductor-superconductor structures for electronic cooling. (a) Optical micrograph of a typical Al/Si/Al microrefrigerator and schematics of the measurement setup. The current I_0 and voltage V_{th} are used to determine the electron temperature in the n^{++} -Si layer, and the bias voltage V is used to change its value. (b) Cross section of the structure along the line AB in (a). (c) Measured electron temperature $T_{e,N}$ in Si versus bias voltage across the Al/Si/Al cooler at different substrate temperatures. Adapted from (Savin *et al.*, 2003).

cal temperature. Figure 29(b) shows a representative set of measurements taken at different bath temperatures T_0 . In particular, it shows the zero-bias resistance of the thermometer junctions R_0 against the bias voltage across the refrigerators (V_{refr}). Dashed lines indicate the behavior at bath temperatures where Ti is still in the normal state: the electron temperature in Ti decreases (i.e., R_0 increases) by increasing V_{refr} , reaching a minimum slightly below $V_{\text{refr}} = 2\Delta_1/e \simeq 420 \mu\text{eV}$, as expected for a SINIS refrigerator (Δ_1 is the energy gap of Al). Note that dashed lines are the upside-down equivalent, for example, of the measurements shown in Fig. 27(c). Thin solid lines indicate the temperature behavior when Ti is cooled from the normal to the superconducting state. This happens for T_0 larger than T_{c2} but below 625 mK, at V_{refr} values for which R_0 has a deep minimum. Here, for instance, starting from $T_0 = 520$ mK, the minimum electron temperature reached in Ti was $T_{\text{min}} \approx 320 \pm 40$ mK, thus demonstrating the effectiveness of the cooling mechanism also in all-superconducting refrigerators. Thick solid line corresponds to the case where the Ti strip is already superconducting, i.e., at a bath temperature below T_{c2} . The results for the minimum electron temperature reached in Ti against T_0 is represented by the open circles in Fig. 29(c). Comparison to the theory gave good agreement with the experiment (lines in Fig. 29(c)) with an electron-phonon interaction constant $\Sigma_{\text{Ti}} \approx 1.3 \text{ nW}/\mu\text{m}^3\text{K}^5$.

3. SSmS structures

Superconductor-semiconductor structures have recently attracted interest in the field of electron cooling (Buonomo *et al.*, 2003; Savin *et al.*, 2003, 2001). The basic idea is to exploit, for the active part of the cooler, heavily-doped semiconductor layers instead of normal metals, with the natural Schottky barrier forming at the contact to the metal electrodes (Brennan, 1999; Lüth, 2001; Rhoderick and Williams, 1988; Sze, 1981, 1985). The peculiar characteristic intrinsic to this scheme stems from the possibility to alter up to a large extent the semiconductor electronic properties (like, for example, the charge density, etc.) and to change the transmissivity of the Schottky barrier through proper doping or choice of the semiconducting layer (see also Sec. VI.F.2).

Heavily-doped silicon is a natural choice both from a practical and technological point of view, mainly owing to the widespread and well-developed Si technology. Up to now, the only evidence of superconducting electron cooling with semiconductors comes from microrefrigerators realized with the silicon-on-insulator (SOI) technology (Buonomo *et al.*, 2003; Savin *et al.*, 2003, 2001). The first demonstration of electron refrigeration in Si was reported by Savin *et al.* (2001), where the authors obtained a maximum temperature reduction under hot quasiparticle extraction of the order of 30% at the bath temperature $T_0 = 175$ mK. Figure 30(a) shows the optical micrograph of a typical Al/Si/Al cooler. The two bigger Al electrodes are used for cooling, while the two smaller for detecting the electronic temperature in Si. A sketch of the structure cross-section is displayed in Fig. 30(b), where the n^{++} -Si region appears just on top of the silicon dioxide insulating layer. The structures were characterized by a doping level $N_D = 4 \times 10^{19} \text{ cm}^{-3}$. A set of cooling curves extracted from one of such devices is shown in Fig. 30(c) (Savin *et al.*, 2003). It displays the electron temperature $T_{e,N}$ in the n^{++} -SOI layer versus bias voltage across the refrigerator at different starting bath temperatures. The observed electronic temperature reduction is of the order of 60% at $T_0 \approx 150$ mK. Although the device volume and the cooler resistances were rather high, the authors attributed this significant cooling to a very small electron-phonon coupling constant in Si: as a matter of fact, the latter was determined to be $\Sigma_{\text{Si}} \simeq 0.1 \text{ nW}/\mu\text{m}^3\text{K}^5$ (Savin *et al.*, 2001), i.e., about one order of magnitude smaller than in Cu. The maximum achieved cooling power was $\dot{Q}_{\text{max}} \approx 1.3 \text{ pW}$ at $T_0 = 175$ mK, mainly limited by the high value of the specific contact resistances ($R_c \sim 67.5 \text{ k}\Omega\mu\text{m}^2$). These authors also addressed the effect of carrier concentration in Si on cooling performance (Savin *et al.*, 2003).

Buonomo *et al.* (Buonomo *et al.*, 2003) also obtained a cooling effect in Al/Si/Al refrigerators, with a device configuration similar to that of Fig. 30(a). Their structures were characterized by a doping level $N_D = 8 \times 10^{18} \text{ cm}^{-3}$ and contact specific resistances $R_c \sim 100 \text{ k}\Omega\mu\text{m}^2$. Notably, they confirmed the same value reported by

Savin *et al.* (2001) for the electron-phonon coupling constant in Si. In addition, these authors also explored the Nb/Si/Nb combination for electron cooling. Their results, however, showed no cooling effect, owing probably to a too transmissive interface at the contact with Si. This effect was ascribed both to the slightly lower Schottky barrier height of Nb/Si contact ($\sim 0.5\text{--}0.6 \text{ eV}$ (Chang *et al.*, 1971; Heslinga and Klapwijk, 1989)) with respect to the Al/Si ($\sim 0.6\text{--}0.7 \text{ eV}$ (Chang *et al.*, 1971; Singh, 1994)) and to disorder-enhanced subgap conductance (Badolato *et al.*, 2000; Bakker *et al.*, 1994; Giazotto *et al.*, 2001a, 2003a, 2001b; Kastalsky *et al.*, 1991; Kutchinsky *et al.*, 1997; Magnée *et al.*, 1994; Nguyen *et al.*, 1992; Nitta *et al.*, 1994; Poirier *et al.*, 1997; van Wees *et al.*, 1992; Xiong *et al.*, 1993). Further results on the electron-phonon coupling constant as well as on the electronic thermal conductivity in n -type Si were reported in (Heslinga and Klapwijk, 1992; Kivinen *et al.*, 2003).

Because of the low electron-phonon coupling constant in heavily doped Si, one may expect to cool islands with larger volumes than in the normal metal case, and perhaps improve the high-temperature limit of cooling by some factor. The issue of high R_c values that limit the maximum achievable cooling power still represents a drawback of these refrigerators that has to be overcome. High doping of the semiconductor (in the tunneling regime $R_c \propto \exp(N_D^{-1/2})$ (Sze, 1981, 1985), see also Sec. VI.F.2) as well as *engineering* of the Schottky barrier height through incorporation of interface layers at the metal-semiconductor junction (Cantile *et al.*, 1994a,b; Costa *et al.*, 1991; De Franceschi *et al.*, 1998a,b, 2000; Grant and Waldrop, 1988; Koyanagi *et al.*, 1993; Marinelli *et al.*, 2000) can be exploited in order to tailor the interface transmissivity.

4. SF systems

As discussed at the beginning of Sec. V.C.1, decreasing the contact resistance (R_T) is not a viable route to enhance heat current in NIS junctions. A possible scheme to surmount the problem of Andreev reflection at the metal-superconductor interface is to exploit, instead of an insulating barrier, a thin ferromagnetic (F) layer in good electric contact with S (Giazotto *et al.*, 2002). The physical origin of the SF cooler operation stems from the spin-band splitting characteristic of a ferromagnet. The electron involved in the Andreev reflection and its phase-matched hole belong to opposite spin bands; as a consequence, depending on the degree of spin polarization \mathcal{P} of the F layer, strong suppression of the Andreev current may occur at the SF interface (de Jong and Beenakker, 1995). In the limit of large \mathcal{P} , the subgap current is thus strongly suppressed while efficient hot-carrier transfer leads to a sizeable heat current across the system. In the following we give the main results of such a proposal.

The impact of partial spin polarization ($\mathcal{P} < 100\%$) in

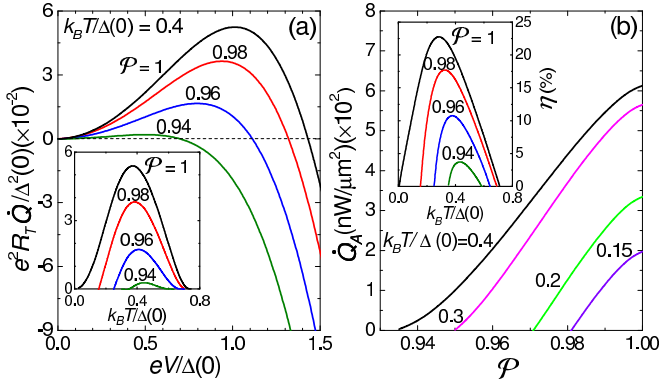


FIG. 31 Superconductor-ferromagnet refrigerator. (a) Calculated heat current \dot{Q} of a SF junction vs bias voltage V at $T = T_{e,F} = T_{e,S} = 0.4 \Delta(0)/k_B$ for several spin polarizations P . The inset shows the same quantity calculated at the optimal bias voltage against temperature for some values of P . (b) Calculated maximum cooling power surface density \dot{Q}_A versus P for various temperatures. The inset shows the coefficient of performance η calculated at the optimal bias voltage versus temperature for some P values. Adapted from (Giazotto *et al.*, 2002, 2005).

the F region is displayed in Fig. 31(a) where the heat current \dot{Q} versus bias voltage across the junction is plotted for some values of P at $T = T_{e,F} = T_{e,S} = 0.4 \Delta(0)/k_B$ ($T_{e,F}$ is the electron temperature in F). For each P value there exists an optimum bias voltage (V_{opt}) which maximizes \dot{Q} . In the limit of a half-metal ferromagnet (i.e., $P = 100\%$) (Coey and Sanvito, 2004; Mazin, 1999) this value is around $V_{opt} \simeq \Delta/e$. Moreover, for $P = 94\%$ there is still a positive \dot{Q} across the junction. The inset of Fig. 31 (a) shows \dot{Q} calculated at each optimized bias voltage against temperature for various values of P . The heat current is maximized around $T = T_{opt} \approx 0.4 \Delta(0)/k_B$, rapidly decreasing both at higher and lower temperatures.

The junction specific cooling power is shown in Fig. 31(b), where \dot{Q}_A (evaluated at each optimal bias voltage) is plotted versus P at different bath temperatures. Notably, for a half-metallic ferromagnet at $T = 0.4 \Delta(0)/k_B$, cooling power surface densities as high as $600 \text{ nW}/\mu\text{m}^2$ can be achieved, i.e., about a factor of 30 larger than those achievable in NIS junctions at the optimized interface transmissivity (i.e., $\mathcal{T} \simeq 3 \times 10^{-2}$ at $T \simeq 0.3 \Delta(0)/k_B$, see Fig. 4(b)). This marked difference stems from SF specific normal-state contact resistances as low as some $10^{-3} \Omega \mu\text{m}^2$ that are currently achieved in highly-transmissive junctions (Upadhyay *et al.*, 1998). The inset of Fig. 31(b) shows the junction coefficient of performance (η) calculated at the optimal bias voltage versus temperature for various P values. Notably, for $P = 100\%$, η reaches $\sim 23\%$ around $T = 0.3 \Delta(0)/k_B$ and exceeds 10% for $P = 96\%$. In addition, in light of a possible exploitation of this structure in combination

with a N region (i.e., a SFN refrigerator) it turned out that cooling effects comparable to the SF case can be achieved with a F-layer thickness of a few nm (i.e., of the order of the magnetic length). We note that the large \dot{Q}_A typical of the SF combination makes it promising as a possible higher-temperature first stage in cascade cooling (for instance, over or around 1 K), where it could dominate over the large thermal coupling to the lattice characteristic for such temperatures.

The results given above point out the necessity of strongly spin-polarized ferromagnets for a proper operation of the SF refrigerator. Among the predicted half-metallic candidates it is possible to indicate CrO_2 (Brener *et al.*, 2000; Kamper *et al.*, 1987; Schwartz, 1986), for which values of P in the range 85...100% have been reported (Coey *et al.*, 1998; Dedkov *et al.*, 2002; Ji *et al.*, 2001; Parker *et al.*, 2002), $(\text{Co}_{1-x}\text{Fe}_x)\text{S}_2$ (Mazin, 2000), NiMnSb (de Groot *et al.*, 1983), $\text{Sr}_2\text{FeMoO}_6$ (Kobayashi *et al.*, 1998) and NiMnV_2 (Weht and Pickett, 1999). So far no experimental realizations of SF structures for cooling applications have been reported.

5. HT_c NIS systems

Heat transport in high-critical temperature (HT_c) NIS junctions was theoretically addressed by Devyatov *et al.* (2000). In these systems the cooling power depends on interface transmissivity as well as on orientation of the superconductor crystal axes and temperature. In particular, these authors showed that the maximum positive heat current in these structures can be achieved in junctions with zero superconducting crystallographic angle, at temperature $T = 0.45 T_c$ and bias voltage $V \approx 0.8 \Delta(0)/e$. The behavior of $\dot{Q}(V)$ turns out to be qualitatively similar to that of NIS junctions based on low-critical temperature superconductors (see Fig. 26(a)), and with comparable values (in relative units). From this it follows that the cooling power of electronic refrigerators based on HT_c materials is approximately two orders of magnitude larger than in NIS junctions based on low-critical temperature superconductors (at much lower temperatures).

A somewhat different cooling effect in HT_c superconductors was predicted by Svidzinsky (2002), who showed that an adiabatic increase of the supercurrent in a ring (or cylinder) made from a HT_c superconductor may lead to a cooling effect. The maximum cooling occurs if the supercurrent is equal to its critical value. For a clean HT_c superconductor, the minimum achievable temperature (T_{min}) was found to be around $T_{min} = T_0^2/T_c$, with T_0 the initial temperature of the ring, thus meaning that substantial cooling can be achieved using large T_c values.

Experimentally, Fee (1993) realized a Peltier refrigerator junction exploiting a HT_c superconductor and operating around liquid nitrogen temperatures. In particular, his device consisted of a BiSb alloy and $\text{YBa}_2\text{Cu}_3\text{O}_{7-\delta}$

superconducting rods connected by a small copper plate which acted as the cold junction of the device. The latter showed a maximum cooling of 5.35 K below the bath temperature $T_0 = 79$ K. The figure of merit of the junction, Z , was estimated to be as large as $2.0 \times 10^{-3} \text{ K}^{-1}$.

6. Application of (SI)NIS structures to lattice refrigeration

One well established application of SINIS refrigerators concerns lattice cooling (Clark *et al.*, 2005; Luukanen *et al.*, 2000; Manninen *et al.*, 1997). As a matter of fact, while NIS tunneling directly cools the electron gas of the normal electrode, the phonon system can be refrigerated through the electron-phonon coupling (see Eq. (24)). The latter, however, is typically very small at the lowest temperatures, thus limiting the heat transfer from the surroundings to the electrons. This situation normally happens whenever the metal to be cooled is in direct contact with a thick substrate, for instance, oxidized Si (Leivo *et al.*, 1996; Nahum *et al.*, 1994): only the electrons of the N region cool down while the metal lattice presumably remains at the substrate temperature. The metal lattice can be refrigerated considerably if the thermal resistance between the phonons and the substrate is not negligible compared to that between the electrons and the phonons. One effective choice to meet this requirement, that was indeed suggested at the beginning of cooling experiments (Fisher *et al.*, 1995; Nahum *et al.*, 1994) as well as for detector applications (Deiker *et al.*, 2004; Doriese *et al.*, 2004; Irwin *et al.*, 1996; Nahum and Martinis, 1995; Pekola *et al.*, 2004b; Ullom *et al.*, 2004), is to exploit a thermally isolated thin dielectric *membrane* on which the N region of the cooler is extended. In this way, tunneling through the NIS junction will cool down the electrons of the metal, then the phonons of the metal (via electron-phonon coupling) that subsequently will refrigerate the membrane phonons (Clark *et al.*, 2005; Luukanen *et al.*, 2000; Manninen *et al.*, 1997) according to

$$\dot{Q}_{\text{SINIS}}(V; T_{e,N}, T_{e,S}) + \dot{Q}_{ph-sub}(T_{ph}, T_{sub}) = 0, \quad (81)$$

where $T_{e,N} \simeq T_{ph}$, $T_{e,S} \simeq T_{sub}$, T_{ph} is the lattice temperature in the dielectric membrane, T_{sub} is the lattice temperature in the substrate, and \dot{Q}_{ph-sub} is the rate of exchanged energy between the membrane phonons and substrate phonons. Eventually, if additional devices are standing on the same dielectric platform (for instance, detectors, etc.), the latter will cool down first the phonons of the device and then its electrons through the electron-phonon interaction.

Dielectric membranes made of silicon nitride (Si_3N_4) have proved to be attractive for this purpose in light of their superior thermal isolation properties at low temperatures. Low-temperature heat transport characterization as well as thermal relaxation in low-stress Si_3N_4 membranes and films were quite recently addressed (Holmes *et al.*, 1998; Leivo and Pekola, 1998).

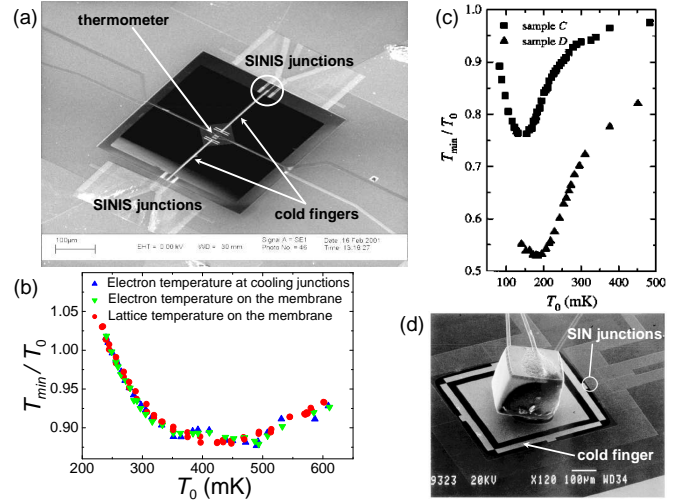


FIG. 32 Lattice refrigeration with SINIS. (a) SEM image of a Si_3N_4 membrane (in the center) with self-suspended bridges. Two normal-metal cold fingers extending onto the membrane are used to cool down the dielectric platform. The $\text{Al}/\text{Al}_2\text{O}_3/\text{Cu}$ SINIS coolers are on the bulk (far down and top) and the thermometer stands in the middle of the membrane. (b) Maximum temperature decrease (T_{min}/T_0) versus bath temperature T_0 measured at different positions in the cooler shown in (a). (c) Maximum *lattice* temperature decrease on the membrane versus bath temperature measured in two other samples similar to that shown in (a). In this case, the refrigerators exploited many small-area junctions arranged in parallel in a comb-like configuration. (d) SEM micrograph of a NIS refrigerator device with a neutron transmutation doped (NTD) Ge resistance thermometer attached on top of it. (c) is adapted from (Luukanen *et al.*, 2000), (d) from (Clark *et al.*, 2005).

The first demonstration reported of lattice cooling (Manninen *et al.*, 1997) exploited such membranes in combination with $\text{Al}/\text{Al}_2\text{O}_3/\text{Cu}$ SINIS refrigerators. In this experiment the authors were able to achieve a 2% temperature decrease in the membrane at bath temperatures $T_0 \approx 200$ mK.

Figure 32(a) shows a SEM image of a typical new-generation lattice cooler fabricated on a Si_3N_4 membrane with self-suspended bridges. The membrane consists of a low-stress Si_3N_4 film deposited by low pressure chemical vapor deposition (LPCVD) on Si, and subsequently etched (with both wet and dry etching) in order to create the suspended bridge structure. In such thin membranes phonon propagation is essentially two-dimensional. The condensation of the phonon gas into lower dimensions in ultrathin membranes was also theoretically discussed (Anghel and Manninen, 1999; Anghel *et al.*, 1998; Kuhn *et al.*, 2004). The self-suspended bridges improve thermal isolation of the dielectric platform from the heat bath (Leivo and Pekola, 1998). The image also shows the $\text{Al}/\text{Al}_2\text{O}_3/\text{Cu}$ refrigerators of the SINIS type that are placed on the bulk substrate (i.e., outside the membrane) to ensure good thermal contact with the bath.

The N cold fingers extend onto the silicon nitride membrane, whose temperature is determined through an additional SINIS thermometer placed in the middle of the structure.

The lattice refrigeration effect achieved in this SINIS refrigerator is shown in Fig. 32(b). Here the maximum temperature decrease of the membrane (T_{min}/T_0) against bath temperature T_0 is displayed (red circles), and shows that temperature reduction as high as about 12% was reached in the 400...500 mK range. The electron refrigeration effect in the Cu region was also measured at two different positions in the device, i.e., nearby the cooling junctions and on the membrane. Notably, the T_{min}/T_0 behavior is almost the same for the different sets of data; this basically means that: a) good thermalization was achieved in the cold fingers; b) the electron-phonon coupling was sufficiently large while Kapitza resistance between Cu and Si_3N_4 was sufficiently small to ensure the lattice temperature on the membrane to be nearly equal to the Cu electron temperature on the membrane itself. The best results of lattice refrigeration by SINIS coolers reported to date are shown in Fig. 32(c) (Luukanen *et al.*, 2000) for two other devices (labeled C and D in the figure) similar to that of Fig. 32(a). These devices exploited three Cu cold fingers and several small-area junctions arranged in parallel in a comb-like configuration for the SINIS cooling stage. The junction specific resistances were $R_c = 1.39 \text{ k}\Omega\mu\text{m}^2$ and $R_c = 220 \text{ }\Omega\mu\text{m}^2$ for device C and D, respectively. Lattice temperature reduction as high as 50% at 200 mK was achieved in the sample with lower R_c , thus confirming the effectiveness of small-area junctions in yielding larger temperature reductions. The achieved cooling power in these devices was estimated on the pW level. The reduction of the refrigeration effect at the lowest temperatures can be explained in terms of larger decoupling of electrons and phonons, but also the effects discussed in Sec. V.C.1 should play a role.

Figure 32 (d) demonstrates the realization of a complete refrigerator device including a thermometer (Clark *et al.*, 2005), where four pairs of NIS junctions are used to cool down a $450 \times 450 \mu\text{m}^2$ suspended Si_3N_4 dielectric membrane. Each NIS junction area is $25 \times 15 \mu\text{m}^2$, and the N electrode consists of Al doped with Mn to suppress superconductivity while Al is used for the superconducting reservoirs. Also shown is a neutron transmutation doped (NTD) Ge resistance thermometer (with volume $250 \times 250 \times 250 \mu\text{m}^3$) glued on the membrane. In such a refrigerator the authors measured with the NTD Ge sensor a minimum final temperature slightly below 240 mK starting from a bath temperature $T_0 = 320 \text{ mK}$, under optimal bias voltage across the cooling junctions. This result is promising in light of a realistic implementation of superconducting refrigerators, and shows the possibility of cooling efficiently the whole content of dielectric membranes through NIS junctions (Pekola, 2005).

Possible strategies to attain enhanced lattice refrigeration performance in the low temperature regime (i.e., below 500 mK) could be a careful optimization in terms

of the number and specific resistance of the cooling junctions as well as to exploit superconductors with the gap larger than in Al. Making the dielectric platform thinner and reducing thermal conduction along it should also increase the temperature drop across the membrane. The exploitation of the described method around or above 1 K, however, is still now not so straightforward, mainly due to the strong temperature dependence of the electron-phonon interaction that thermally shunts more effectively the N electrode portion standing on the bulk substrate to the lattice (note that also the thermal conduction along the membrane is strongly temperature dependent (Kuhn *et al.*, 2004; Leivo and Pekola, 1998)). Toward this end, a reduction of the N volume placed out of the membrane should help; in addition, $\text{S}_1\text{IS}_2(\text{IS}_1)$ refrigerators (see Sec. V.C.2) as well as SF junctions (see Sec. V.C.4) might significantly improve the membrane cooling in the higher temperature regime.

7. Josephson transistors

A further interesting field of application of SINIS structures concerns superconducting weak links (Golubov *et al.*, 2004; Likharev, 1979). In particular, in *diffusive* SNS junctions, i.e., where the junction length largely exceeds the elastic mean free path, coherent sequential Andreev scattering between the superconducting electrodes may give rise to a continuum spectrum of resonant levels (Belzig *et al.*, 1999; Heikkilä *et al.*, 2002; Yip, 1998) responsible for carrying the Josephson current across the structure. The supercurrent turns out to be given by this spectrum weighted by the occupation number of correlated electron-hole pairs, the latter being determined by the quasiparticle energy distribution in the N region of the weak link. In *controllable* Josephson junctions, the supercurrent is modulated by driving the quasiparticle distribution out of equilibrium (Heikkilä *et al.*, 2002; Seviour and Volkov, 2000a; Volkov, 1995; Volkov and Pavlovskii, 1996; Volkov and Takayanagi, 1997; van Wees *et al.*, 1991; Wilhelm *et al.*, 1998; Yip, 1998) via dissipative current injection in the weak link from additional normal-metal terminals. This operation principle leads to a controlled supercurrent suppression and was successfully exploited both in all-metal (Baselmans *et al.*, 2002a, 1999, 2001a,b, 2002b; Huang *et al.*, 2002; Morpurgo *et al.*, 1998; Shaikhaidarov *et al.*, 2000) (where a transition to a π -state was also reported) as well as in hybrid semiconductor-superconductor weak links (Kutchinsky *et al.*, 1999; Neurohr *et al.*, 1999; Richter, 2000; Schäpers *et al.*, 2003a, 1998, 2003b). The situation drastically changes if we allow current injection from additional *superconducting* terminals arranged in a SINIS fashion (Baselmans, 2002; Giazotto *et al.*, 2004a,b, 2003b). In this way, thanks to the SINIS junctions, critical supercurrent can be strongly increased as well as steeply suppressed with respect to equilibrium, leading

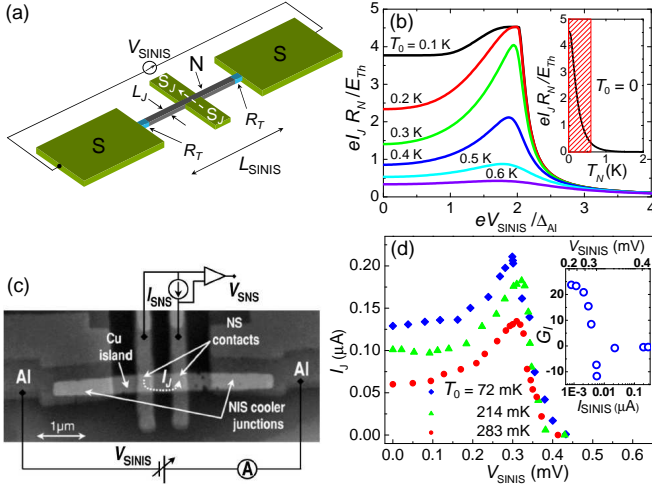


FIG. 33 Josephson transistor. (a) Simplified scheme of a SINIS-controlled Josephson transistor. The Josephson current in the S_JNS_J weak link (along the white dashed line) is controlled by applying a bias V_{SINIS} across the SINIS line connected to the weak link, allowing to increase or decrease its magnitude with respect to equilibrium. (b) Theoretical normalized critical current I_J versus V_{SINIS} calculated in the quasiequilibrium limit for several lattice temperatures T_0 for a Nb/Cu/Nb *long* junction. The inset shows the supercurrent vs electron temperature characteristic calculated at $\phi = \pi/2$. (c) SEM image of an Al/Cu/Al Josephson junction including the Al/Al₂O₃/Cu symmetric SINIS electron cooler. The SNS long weak link is placed in the middle of the structure. Also shown is a scheme of the measurement circuit. (d) Measured critical current I_J versus V_{SINIS} at three different bath temperatures T_0 for the device shown in (c). The inset displays the measured differential current gain G_I versus I_{SINIS} at $T_0 = 72$ mK. (b) is adapted from (Giazotto *et al.*, 2003b), while (c) and (d) from (Savin *et al.*, 2004).

to a tunable structure with large current and power gain.

A simplified scheme of this class of transistors is displayed in Fig. 33(a). A diffusive S_JNS_J *long* Josephson junction of length L_J (i.e., with $L_J \gg \xi_0$, where ξ_0 is the S_J coherence length) shares the N region of a SINIS control line of length L_{SINIS} . The superconductors S_J and S can be in general different (i.e., with gaps Δ_J and Δ_S , respectively); in addition, the S_J electrodes are kept at zero potential, while the SINIS line is biased with V_{SINIS} . The supercurrent (I_J) behavior in response to a bias voltage V_{SINIS} stems from the degree of nonequilibrium the SINIS line is able to generate in the weak link according to (Heikkilä *et al.*, 2002; Wilhelm *et al.*, 1998; Yip, 1998)

$$I_J(V_{SINIS}) = \frac{1}{eR_N} \int_0^\infty dE j_S(E, \phi) (1 - 2f(E, V_{SINIS})), \quad (82)$$

where R_N is the weak link normal-state resistance, ϕ is the phase difference across the superconductors, and $j_S(E, \phi)$ is the spectral supercurrent, obtainable from the solution of the Usadel equations (Usadel, 1970). The

most straightforward situation occurs at sufficiently low lattice temperatures, i.e., typically below 1 K, when $\ell_{e-e} < L_{SINIS} < \ell_{e-ph}$ (see Sec. II). In such a case, strong electron-electron relaxation forces the electron system in the N region to retain a local thermal quasiequilibrium (see also Sec. V.C.1), so that $1 - 2f(E, V_{SINIS}) = \tanh[E/(2k_B T_{e,N}(V_{SINIS}))]$. The transistor effect in the structure thus simply depends on the electron temperature $T_{e,N}(V_{SINIS})$ established in the weak link upon biasing the SINIS line according to Eq. (80). The full calculation of the behavior of a prototype Nb/Cu/Nb long Josephson junction with integrated Al/Al₂O₃/Cu SINIS electron cooler is displayed in Fig. 33(b) (Giazotto *et al.*, 2003b). Here the normalized I_J is plotted against V_{SINIS} for several bath temperatures T_0 . For all chosen values of T_0 , the supercurrent value increases monotonically up to about $V_{SINIS} \approx 1.8 \Delta_S/e$, where the SINIS line provides the largest cooling power and allows to attain the lowest electron temperature. Then, by further increasing the voltage, an efficient suppression of I_J occurs due to electron heating: the device behaves as a tunable superconducting junction. The above given results can be easily understood recalling that for a *long* SNS junction at low lattice temperature (i.e., $k_B T_0 \ll \Delta_J$) and for $k_B T_{e,N} \gg E_{Th} = \hbar D/L_J^2$ (D is the N-region diffusion coefficient), I_J depends exponentially on the effective electron temperature $T_{e,N}$ (Wilhelm *et al.*, 1997; Zaikin and Zharkov, 1981) and is almost independent of T_0 . Hence, long junctions are more appropriate for the device to obtain large I_J changes with small $T_{e,N}$ variations (as indicated by the red hatched region in the inset of Fig. 33(b)). In the *short* junction limit ($L_J \ll \xi_0$), conversely, the I_J temperature dependence is set by the energy gap Δ_J , thus implying a much reduced effect from the cooling line. Furthermore, it is expected that the power dissipation values from two to four order of magnitude smaller than with all-normal control lines can be obtained in these structures, thus making them promising as mesoscopic transistors for low dissipation cryogenic applications.

So far, the only successful demonstration of this transistor-like operation was reported by (Savin *et al.*, 2004) in Al/Cu/Al SNS junctions integrated with Al/Al₂O₃/Cu SINIS refrigerators. The SEM image of one of these samples along with a scheme of the measurement setup is shown in Fig. 33(c). The structure parameters were the following: cooler junction resistances $R_T \simeq 240 \Omega$, Josephson weak link normal state resistance $R_N = 11.5 \Omega$, and minimum SNS interelectrode separation $L_J \simeq 0.4 \mu\text{m}$ that compared with the superconducting coherence length ($\xi_0 \approx 62$ nm) provides the frame of the *long* junction regime. The critical current I_J versus V_{SINIS} at three different T_0 is shown in Fig. 33(d). For each bath temperature, I_J increases around $V_{SINIS} \approx 1.8 \Delta_S/e$, as expected from the reduction of $T_{e,N}$ by electron cooling, while it is steeply suppressed at larger bias voltages. The resemblance of the experiment with the curves of Fig. 33(b) is evident. In

the present case, I_J enhancement under hot quasiparticle extraction by more than a factor of two was observed at $T_0 = 283$ mK. The transistor current gain $G_I = dI_J/dI_{\text{SINIS}}$, shown in the inset of Fig. 33(d), obtained values in the range $-11...20$ depending on the control bias. As far as power dissipation is concerned, these authors reported low dissipated power on the 10^{-13} W level in the extraction regime while of some tens of pW in the regime of I_J suppression.

The transistor behavior for arbitrary inelastic scattering strength in the SINIS line (or, equivalently, for arbitrary values of L_{SINIS}) as well as for different SNS junction lengths, was theoretically addressed in detail in (Giazotto *et al.*, 2004a,b). The role of geometry, materials combination, phase dependence, and the input noise power were also discussed. Notably, a marked supercurrent transition to a π -state under nonequilibrium (about two times larger than that achievable with an all-normal control channel (Wilhelm *et al.*, 1998; Yip, 1998)) was predicted to occur for negligible or moderate electron-electron interaction. We recall that in the π -state (Bulaevskii *et al.*, 1977) the supercurrent flows in opposite direction with respect to the phase difference ϕ between the two superconductors, i.e., such a sign reversal is equivalent to the addition of a phase factor π to the Josephson current-phase relation. Furthermore, current gain in the range $10^2...10^5$ and power gain up to 10^3 were predicted to occur depending on the control voltage.

Finally, transistor operation in a Josephson *tunnel* junction integrated with a $S_1IS_2IS_1$ refrigerator was also theoretically addressed in the quasiequilibrium regime (Giazotto and Pekola, 2005). In this case, the device benefits from the sharp characteristics due to the presence of superconductors with unequal energy gaps (see also V.C.2), that leads to improved overall characteristics as compared to the SINIS-controlled SNS junction in the same transport regime.

D. Perspective types of refrigerators

Any electric current that is accompanied by the extraction of hot electrons (or holes) can be used, in principle, for refrigeration purposes. For instance, this may happen in *thermionic* transport over a potential barrier as well as in energy-dependent *tunneling* through a barrier. Since an exhaustive analysis of all possible predicted refrigeration methods is far beyond the limits set to this Review, in the following we give a brief description of a few examples that we believe are relevant in the present context. In such devices, several different effects may contribute to the refrigeration process (e.g., thermionic transport, quantum tunneling as well as thermoelectric effects), so that making a proper "classification" of the refrigeration principle is, strictly speaking, rather difficult. As a consequence, we shall try mainly to follow the definitions as they were introduced in the original literature.

1. Thermionic refrigerators

A vacuum thermionic cooling device consists of two electrodes separated by a vacuum gap. Cooling occurs when highly energetic electrons overcome the vacuum barrier through thermionic emission, thus reducing the electron temperature of one of the two electrodes. In such a situation, the refrigerator operation is mainly affected and limited by radiative heat transfer between the electrodes. The thermionic emission current density (j_R) is given by the Richardson equation, $j_R = A_0 T^2 \exp(-\frac{\Phi}{k_B T})$, where Φ and T are the work function and the temperature of the emitting electrode, respectively, $A_0 = 4\pi em k_B^2 / h^3$ is the Richardson constant, and m is the electron mass. From the expression above, a strong reduction of j_R is expected upon lowering the temperature. Mahan (1994) developed a simple model for thermionic refrigeration, and demonstrated that its efficiency can be as high as 80% of the Carnot value. Vacuum thermionic refrigerators are generally characterized by a higher efficiency as compared to thermoelectric coolers, and are considered to be an attractive solution for future refrigeration devices (Nolas and Goldsmid, 1999). However, the high Φ values typical of currently available materials make thermionic cooling efficient, at present, only above 500 K.

Several ideas on how to increase the cathode emission current and to improve the operation of these refrigerators have been proposed (Hishinuma *et al.*, 2001, 2002; Korotkov and Likharev, 1999; Purcell *et al.*, 1994). Korotkov and Likharev suggested to cover the emitter with a thin layer of a wide-gap semiconductor, and to exploit the resonant emission current to cool the emitter (Korotkov and Likharev, 1999). The analysis of such a thermionic cooler predicted an efficient refrigeration down to 10 K.

The issue of high Φ values can be overcome by a reduction of the distance between the electrodes (in the submicron range) and by the application of a strong electric field. Following this scheme, Hishinuma *et al.* (2001) theoretically analyzed a thermionic cooler where the two electrodes were separated by a distance in the nanometer range. In such a situation, the potential barrier is essentially lowered (see Fig. 34(a)), allowing both thermionic emission and energy-dependent tunneling. As a consequence, rather small (if compared to vacuum thermionic devices) external voltages ($\sim 1...3$ V) are required in order to produce significant electric currents. For suitable values of the applied voltage and distances between the electrodes, electrons above the Fermi level dominate the electric transport (both thermionic emission over the barrier and tunneling through the barrier), thus leading to cooling of the emitter. As it can be inferred from Fig. 34(b), the contribution of the energy-dependent tunneling to total cooling is essential, and this refrigerator could be classified as a vacuum tunneling device. The cooling power surface density in this combined thermionic-tunneling refrigerator was predicted to

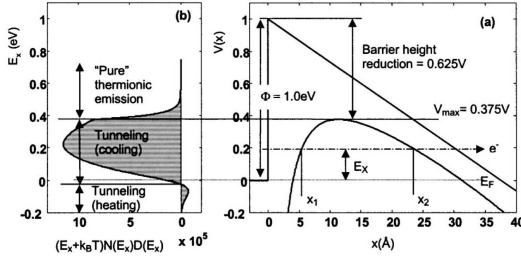


FIG. 34 Refrigeration by combined tunneling and thermionic emission. (a) Schematic diagram of the potential barrier profile $V(x)$ for $\Phi = 1$ eV and with electrode separation of 60 Å. (b) Heat flow distribution at $T = 300$ K. Adapted from (Hishinuma *et al.*, 2001).

obtain values as high as 100 W/cm^2 at room temperature. However, in the only experimental demonstration of this device, a moderate emission current (below 10 nA) was reported at room temperature, with an observed temperature reduction of about 1 mK (Hishinuma *et al.*, 2003). So far, no experimental demonstration of vacuum thermionic refrigeration at cryogenic temperatures has been reported.

2. Application of low-dimensional systems to electronic refrigeration

The exploitation of low-dimensional systems gives additional degrees of freedom in order to engineer materials that may lead to enhanced operation of thermoelectric and thermionic devices (Hicks *et al.*, 1993; Hishinuma *et al.*, 2002; Sales, 2002; Sofo and Mahan, 1994). Some of the limitations intrinsic to vacuum thermionic refrigerators can be overcome with *solid state* thermionic coolers (Mahan and Woods, 1998; Shakouri and Bowers, 1997). As a matter of fact, modern growth techniques easily allow one to control both the barrier height and its width within a wide range of values. One disadvantage of solid state thermionic coolers stems from the thermal conductivity of the barrier which is essentially absent in vacuum devices. Nevertheless, a large temperature reduction can be achieved by using a multilayered heterostructure (Mahan and Woods, 1998; Shakouri and Bowers, 1997; Zhou *et al.*, 1999). According to theory (Mahan and Woods, 1998; Shakouri and Bowers, 1997), heterostructure-based thermionic refrigerators perform somewhat better as compared to thermoelectric coolers. The predicted temperature reduction of a single-stage device at room temperature can be as high as 40 K, and this value can be significantly increased in a multilayer configuration. So far, however, the experimental implementations of single barrier (Shakouri *et al.*, 1999) and superlattice (Fan *et al.*, 2001; Zhang *et al.*, 2003) refrigerators have reported temperature reductions of a few

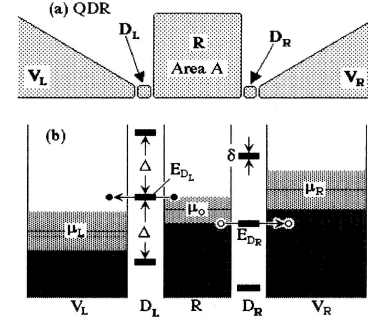


FIG. 35 Quantum-dot refrigerator. (a) Scheme of a quantum-dot refrigerator. (b) Energy-level diagram of the structure. The reservoir R is cooled as its quasiparticle distribution function is sharpened by resonant tunneling through quantum dots D_L and D_R to the electrodes V_L and V_R . From (Edwards *et al.*, 1995).

degrees at room temperature.

Further improvement of thermionic refrigeration can, in principle, be achieved by combining laser cooling and thermionic cooling (Mal'shukov and Chao, 2001; Shakouri and Bowers, 1997). In such an opto-thermionic device, hot electrons and holes extracted through thermionic emission lose their energy by emitting photons rather than by heating the lattice. The theoretical investigation of a GaAs/AlGaAs-based opto-thermionic refrigerator predicted specific cooling power densities of the order of several W/cm^2 at 300 K (Mal'shukov and Chao, 2001).

The presence of singularities in the energy spectrum of low-dimensional systems can be used in solid state refrigeration. For instance, the discrete energy spectrum in quantum dots can be exploited for refrigeration at cryogenic temperatures (Edwards *et al.*, 1995, 1993). In such a quantum-dot refrigerator (QDR) (see Fig. 35(a)) a reservoir (R) is coupled to two electrodes via quantum dots (D_L and D_R) whose energy levels can be tuned through capacitively-coupled electrodes. The QD energy levels can be adjusted so that resonant tunneling to the electrode V_L is used to deplete the states in R above μ_0 and, similarly, holes below μ_0 in R tunnel to V_R (see Fig. 35(b)). As a consequence, the net result will be to sharpen the quasiparticle distribution function in R, thus leading to electron refrigeration. In spite of a rather moderate achievable cooling power, the QDR was predicted to be effective for cooling electrons of a micrometer-sized two-dimensional electron gas reservoir at mK temperatures, and even of a macroscopic reservoir at lower temperatures (Edwards *et al.*, 1995, 1993).

VI. DEVICE FABRICATION

A. Structure typologies and material considerations

This section is devoted to the description of the main techniques and experimental procedures used for the fabrication of typical superconducting electronic refrigerators and detectors. Owing to the great advances reached in the last decades in micro- and nanofabrication technology (Bhushan, 2004; Timp, 1999), the amount of information related to fabrication methods is too large to be covered here and beyond the scope of the present review. Therefore, we only briefly highlight all those issues that we believe are strictly relevant for this research field. In particular we first of all focus on the two typologies of existing superconducting structures, namely all-metal and hybrid devices, and on the main differences between them, both in terms of materials and fabrication techniques. The former concern structures where the active parts of the device, i.e., both the superconducting elements and the normal regions are made of metals; in hybrid structures, the non superconducting active part of the device is made of doped semiconducting layers.

As far as all-metal-based structures are concerned, they are realized with low-critical-temperature thin-film superconductors (normally Al, Nb, Ti and Mo), while the normal regions usually consist of Cu, Ag or Au. Their fabrication protocol includes patterning of a suitable radiation-sensitive masking layer through electron-beam or optical lithography in combination with a shadow-mask (angle) evaporation technique (Dolan, 1977). The final device is thus realized in a single step in the deposition chamber, where additional tunnel barriers between different regions of the structure are *in-situ* created by suitable oxidation of the metallic layers. Although all this leads to an efficient way for fabricating metallic structures, however the electronic properties typical of metals are only weakly dependent on their growth conditions and on the specific employed technique. As a consequence, it is hard to tailor the metallic properties in order to finally match some specific requirements.

On the other hand, the situation is rather different with semiconductors that offer some advantages in comparison to metals. The large magnitude difference of Fermi wave-vector between metals and semiconductors allows in general to observe quantum effects in structures much bigger than with metals. In addition, the availability of several techniques for growing high-purity crystals (e.g., molecular beam epitaxy) yields the capacity to tailor the semiconductor electronic properties and, at the same time, enables the fabrication of structures characterized by coherent transport especially in reduced dimensionality (Capasso, 1990). The exploitation of low-dimensional electron systems as active elements of electronic coolers was predicted to be the next possible breakthrough in this research field (Edwards *et al.*, 1995, 1993; Hicks and Dresselhaus, 1993a,b; Hicks *et al.*, 1993, 1996; Koga *et al.*, 2000, 1998, 1999). Moreover, the realization

of structures where charge carriers experience arbitrarily chosen effective potentials is a further advantage of modern engineered heterostructures (Yu and Cardona, 2001). Last but not least, the possibility of changing the carrier density through electrostatic gating allows to strongly alter some semiconductor parameters (like the mobility as well as the coherence length), thus enabling to have access to different electronic transport regimes in the same structure (Ferry and Goodnick, 1997).

Like all-metal devices, hybrid structures generally exploit the same superconducting materials. However, only heavily-doped Si layers in combination with superconductors were exploited up to now for the realization of superconducting refrigerators (Buonomo *et al.*, 2003; Savin *et al.*, 2003, 2001). The fabrication procedure of hybrid structures involves typically two lithographic steps, where the first allows to pattern the semiconductor active layer through various techniques (such as wet or dry etching). The second one the patterning of the superconducting electrodes. Differently from all-metal devices, at the metal-semiconductor interface forms the well-known Schottky barrier (Lüth, 2001). The latter can be tailored through suitable doping of the semiconductor, allowing to control the interface transmissivity (i.e., the junction specific resistance) over several orders of magnitude.

Both all-metal and hybrid structures are normally fabricated on semi-insulating semiconductor substrates which provide both the mechanical support and rigidity as well as the thermalization of the device at the bath temperature. It is noteworthy to mention that undoped thermally-oxidized Si substrates are widely used toward this end for metallic structures, while hybrid coolers typically exploit the silicon-on-insulator (SOI) technique in order to provide the Si active layer.

B. Semiconductor growth techniques

Depending on the physical principle exploited, semiconductor growth technologies can be either physical or chemical, such as gas and liquid-phase chemical processes. In the following we give a brief survey of the most common semiconductor growth methods.

The Czochralski (1918) crystal pulling method is probably the most common technique for growing semiconductor bulk single crystals and the largest amount of Si used in the semiconductor industry is obtained using this technique. This technique allows to grow large semiconductor single crystals. However, it is often sufficient and less demanding from an economical point of view, to grow a thin ($\sim 1 \mu\text{m}$) perfect crystal layer on top of a bulk crystal of lower quality. This is accomplished by growing *epitaxially* the top layer, i.e., the atoms forming the latter build a crystal with the same crystallographic structure and orientation as the starting substrate (in contrast, non-epitaxial layers can be amorphous or polycrystalline).

Gas-phase epitaxy is a widespread technique and represents nowadays the most important process for the industrial fabrication of Si and GaAs devices. In chemical vapour deposition (CVD) (Adams, 1983; Grove, 1967; Sze, 1985), the constituents of the vapor phase chemically react at the substrate surface and the product of the reaction is a film deposited on the substrate. Nowadays, CVD is widely employed for growing several elemental semiconductors and alloys and, depending on the specific application, it has been implemented and adapted in a number of different configurations (Jensen, 1989). Among these we mention 1) metalorganic CVD (MOCVD), exploits a thermally heated reactor and organometallic gas sources; 2) plasma-enhanced CVD (PECVD), exploits a plasma discharge to provide the energy for the reactions to occur; 3) atmospheric pressure CVD (APCVD), does not require a vacuum environment.

While typical CVD processes are carried out in low vacuum (i.e., in the pressure range from 10^{-1} to several Torr), molecular beam epitaxy (MBE) (Arthur, 1968; Chang and Ludeke, 1975; Cho, 1970; Cho and Arthur, 1975) is an ultrahigh vacuum (UHV) growth technique, performed at pressures usually lower than 10^{-10} Torr. In such vacuum conditions the amount of residual gas contaminants present in the growth chamber is minimized, thus allowing to deposit epitaxial layers of high purity and quality. The main features of this method are a precise control of both chemical and stoichiometric composition, and a perfect tuning of doping profiles on the scale of a single atomic layer (Cho, 1979). The film growth concept is fundamentally an evolution of UHV evaporation, where thermal or electron-beam sources are used to create a flux of *molecular* species. Significant MBE work has been achieved with Si and Ge as well as with IV-IV and II-VI semiconductor compounds and several metals, but probably the largest amount of research has been devoted to III-V semiconductor alloys.

C. Thin-film metals deposition methods

1. Thermal evaporation

Vacuum evaporation is one of the oldest and simplest thin film deposition techniques (Holland, 1958; Maissel and Glang, 1970). It is a physical vapor deposition (PVD) method widely used to deposit a variety of materials, from elemental metals to alloys and insulators. Evaporation is based on the boiling off or sublimation of a heated source material onto a substrate surface. The result of the evaporant condensation is the final film. The rate of atoms or molecules (\mathcal{N}_e) lost under evaporation from a source material per unit area per unit time can be expressed by the Hertz-Knudsen relation $\mathcal{N}_e = a[P_V^*(T) - P][2\pi M k_B T]^{-1/2}$, where a is the evaporation coefficient ($a = 1$ for a clean evaporant surface), P is the ambient hydrostatic pressure acting on the evaporant in the condensed phase, $P_V^*(T)$ is the equilibrium

vapor pressure of the evaporant, and M its molecular weight. This expression shows that the evaporation rate strongly depends on the evaporant vapor pressure. Most common metals typically deposited by thermal evaporation (such as Al, Au, Ga, and In) usually have vapor pressures in the range between 10^{-2} to 1 Torr in the temperature window of $600^\circ \dots 2000^\circ \text{C}$; conversely refractory metals (such as Nb, Mo, Ta, W and Pt) or ceramics (such as BN, and Al_2O_3) reach such vapor pressures at much higher temperatures, thus making more difficult the exploitation of this technique for the deposition.

Usually evaporation is performed in high or ultrahigh vacuum (in the range $10^{-5} \dots 10^{-10}$ Torr), where the mean free path ℓ for the evaporant species is much larger than the substrate-source distance. This translates in an almost line of sight evaporation which prevents covering of edges perpendicular to the source, the latter also referred to as the lack of step coverage (Madou, 1997) (note that this property is at the basis of lift-off processes (Moreau, 1988) as well as of angle (shadow) evaporation technique using suspended masks (Dolan, 1977; Dolan and Dunsmuir, 1988)). Furthermore, vacuum evaporation is a low-energy process (implying a negligible damage to the substrate surface), where the typical energy of the evaporant material impinging on the substrate is of the order of 0.1 eV. Nevertheless, radiative heating can be high.

Resistive heating and *electron-beam* deposition are the two most common methods of evaporation. The former relies on direct thermal heating to evaporate the source material. This method is fairly simple, robust and economic but suffers from a limited maximum achievable temperature (of the order of 1800°C), which prevents the evaporation of refractory metals and several oxides. On the other side, electron-beam evaporation represents a crucial improvement over resistive heating. This method exploits a high-energy electron beam that is focused through a magnetic field on a localized region of the source material. A wide range of materials (including refractory metals and a wide choice of oxides) can be deposited owing to the generation of high temperatures (in excess of 3000°C) over a restricted area. Its main drawback relies on the generation of X-rays from the high-voltage electron beam which may damage sensitive substrates (such as semiconductors) (Moreau, 1988; Sze, 1985). Achievable deposition rates are up to several hundreds $\text{\AA}/\text{sec}$ (e.g., $0.5 \mu\text{m}/\text{min}$ for Al) (Madou, 1997).

2. Sputter deposition

The sputtering process has been known and used for over 150 years (Chapman and Mangano, 1988; Chapman, 1980; Rossmagel, 1998; Wasa and Hayakawa, 1992). It is a PVD method widely used nowadays for many applications, both in the electronic and mechanic industry fields as well as in the pure research environment. This process is based on the removal of material

from a solid target through its bombardment caused by incident positive ions emitted from a (rare) gas glow discharge. The transferred momentum of the ions leads to the expulsion of atoms from the target material, thereby enabling the deposition (condensation) of a film on the substrate surface. Sputter deposition is generally performed at energies in the range of 0.4 to 3 keV. Furthermore, the average energy of emitted ions from the target source is in the range 10...100 eV. At these energies bombarding ions can penetrate up to two atomic layers in the substrate thus leading to a great improvement of the adhesion of the sputtered film (Maissel and Glang, 1970; Wasa and Hayakawa, 1992). Normally, relatively high pressures (from 10^{-4} to 10^{-1} Torr) are maintained in the growth chamber during deposition. At these pressures the mean free path is short (of the order of 1 mm at 10^{-1} Torr) so that the material atoms reach the substrate surface with random incident angles. As a consequence, a very good step coverage can be achieved. Being essentially mechanical in nature, sputtering successfully allows the deposition of refractory metals (superconductors) like Nb, NbN, Ta, Mo and W at temperatures well below their melting points.

D. Thin film insulators

The roles of thin film insulators in solid state electronics are various. In particular, deposited films are often used as interlevel dielectrics for metals, to realize lithographic masking for diffusion and implantation processes, as well as for passivation and protective layers (Ghandhi, 1983; Nicollian and Brews, 1983; Sze, 1985). In addition they can be exploited as thin amorphous membranes on which micro- and nanostructured devices are realized (Clark *et al.*, 2005; Fisher *et al.*, 1999; Irwin *et al.*, 1996; Lanting *et al.*, 2005; Luukanen *et al.*, 2000; Nahum and Martinis, 1995) in light of their specific electric and thermal properties (Leivo and Pekola, 1998; Leoni *et al.*, 2003; Manninen *et al.*, 1997). In the following we discuss those insulators which are considered particularly relevant for microelectronic fabrication processing, i.e., silicon dioxide and silicon nitride.

Silicon dioxide (SiO_2) is one of the most exploited insulators in micro- and nanoelectronics based on Si, mainly due to the high quality of the SiO_2/Si interface. SiO_2 films can be grown on Si substrates by thermal oxidation using oxygen or steam. Thermal oxidation of Si is generally carried out in reactors at temperatures between 900°C and 1200°C . The resulting SiO_2 film is amorphous and characterized by good uniformity, lack of porosity and very good adhesion to the substrate. Some typical parameters of thermally grown silicon dioxide at 1000°C are a refractive index of 1.46, a breakdown strength larger than 10^7 V/cm , and a density of 2.2 g/cm^3 (Nguyen, 1988; Sze, 1985). An alternative way to deposit silicon dioxide layers is through CVD techniques (Nguyen, 1988; Reif, 1990). In particular PECVD

is considered an effective technique (Adams, 1986; Hess, 1984; Kaganowicz *et al.*, 1984) because of the low deposition temperature (SiO_2 is generally deposited in the temperature range 200°C ... 500°C). Silicon oxide can be deposited from silane (SiH_4) with O_2 , CO_2 , N_2O or CO (Adams *et al.*, 1981; Hollahan, 1974). In addition, plasma oxide film properties are strongly dependent on the growth conditions such as reactor configuration, RF power, frequency, substrate temperature, pressure and gas fluxes. Typical parameters for plasma-deposited silicon dioxide films at 450°C are a refractive index of 1.44...1.50, a breakdown strength of $2\text{...}8 \times 10^6\text{ V/cm}$, and a density of 2.1 g/cm^3 .

Silicon nitride is another insulating film that forms good interfaces with Si. It is nowadays successfully used as interlevel dielectric (Swan *et al.*, 1967), in multilayer resist systems (Suzuki *et al.*, 1982), as well as a protective coating as it provides an efficient barrier against moisture and alkali ions (e.g., Na) (Sze, 1985). PECVD is commonly used (Adams, 1986; Hess, 1984) because of the low deposition temperature (250°C ... 400°C) implying low mechanical stress. Silicon nitride is typically formed by reacting silane and ammonia (NH_3) or nitrogen in the glow discharge. As for SiO_2 , the properties of the final film strongly depend on the deposition conditions (Adams, 1986; Chow *et al.*, 1982; Dun *et al.*, 1981; Nguyen *et al.*, 1984). Typical parameters for plasma-deposited silicon nitride films at 300°C are a refractive index of 2.0...2.1, a density of $2.5\text{...}2.8\text{ g/cm}^3$, and a breakdown strength of $6 \times 10^6\text{ V/cm}$.

E. Lithography and etching techniques

Fabrication of thin film metallic circuits as well as semiconductor micro- and nanodevices requires the generation of suitable patterns through lithographic processes (Campbell, 2001; Jaeger, 2002; Plummer *et al.*, 2000). Lithography, indeed, is the method used to transfer such patterns onto a substrate (e.g., Si, GaAs, glass, etc.), thus defining those regions for subsequent etching removal or material addition.

In photolithography (Levinson and Arnold, 1997) a radiation-sensitive polymeric material (called *resist*) is spun on a substrate as a thin film. The image exposure is then transferred to the resist through a photomask, consisting normally of a glass plate having the desired pattern of clear and opaque areas in the form of a thin ($\sim 1000\text{ \AA}$) Cr layer. Two types of resists can be used in such a process, i.e., *positive* and *negative* resists (Colclaser, 1980; Moreau, 1988; Thompson *et al.*, 1994). In the former, the solubility of the exposed areas in a solvent called developer is enhanced, while in the latter the solubility is decreased. After exposure, the resist is developed and reproduces the desired pattern images for the subsequent processing. The radiation source for photolithography depends on the desired final resolution, although the latter is mainly limited by effects due to light

diffraction (Levinson and Arnold, 1997). In particular, high pressure Hg lamps (with a wavelength $\lambda = 365$ nm i-line or $\lambda = 436$ nm g-line) allow a line-width larger than $0.250 \mu\text{m}$, while in the range $130\ldots 250$ nm deep UV (DUV) sources like excimer lasers are necessary, such as KrF ($\lambda = 248$ nm) and ArF ($\lambda = 193$ nm).

Electron-beam lithography (Brewer, 1980; McCord and Rooks, 1997) represents an attractive technique for the fabrication of micro- and nanostructures (Kern *et al.*, 1984). This method exploits a focused electron beam (with energy in the range $10\ldots 100$ keV and diameter of $0.2\ldots 100$ nm) to expose a polymer-based electron-sensitive resist (such as polymethyl-methacrylate (PMMA)). Like in photolithography, the resist can be either positive or negative. Even if the wavelength of the impinging radiation beam can be smaller than 0.1 nm, the maximum achievable resolution is set by the electron scattering in the resist and backscattering from substrate (known as the "proximity effect" (Howard *et al.*, 1983; Jackel *et al.*, 1984; Jamoto and Shimizu, 1983; Kyser, 1983; Kyser and Viswanathan, 1975)), so that the resolution is generally larger than 10 nm (note, however, that resolutions as high as 2 nm have been achieved on some materials (Mochel *et al.*, 1983)).

In addition to lithographic procedures, etching of thin films or bulk substrates represents an important step for the fabrication of the final structure (Madou, 1997; Sze, 1985). Toward this end, insulating or conducting thin films are exploited as masking layers for subsequent material removal. Two crucial parameters of any etching process are *directionality* and *selectivity*. The former refers to the etch profile under the masking layer. In particular, for an *isotropic* etch, the etching rate is approximately the same in all directions, leading to a spherical profile under the mask. With *anisotropic* etch, the etching rate depends on the specific direction (e.g., a particular crystallographic plane) thus leading to straight profiles and sidewalls. Selectivity instead represents how well the etchant can differentiate between the masking layer and the layer that has to be removed. Moreover, etching techniques can be divided into wet (Ghandhi, 1983; Kendall and Shultz, 1997) and dry (Madou, 1997; Wasa and Hayakawa, 1992) categories. In wet etching, the substrate is placed in a liquid solution, usually a strong base or acid. The advantage of wet etching stems from its higher selectivity in comparison to dry methods. Wet etching is in general isotropic for most substrates, and various solutions that yield anisotropic etching are available for some materials. In dry etching, the substrate is exposed to a plasma in a reactor where ions can etch the substrate surface. The great advantage of dry etching with respect to wet etching resides in its higher anisotropy (that allows vertical etch walls), and smaller undercut (that enables smaller lines to be patterned with much higher resolution). Several materials (e.g., insulators, semiconductors as well as refractory metals) can be successfully dry etched, for which a variety of chemistries

and recipes are available (Cotler and Elta, 1990).

F. Tunnel barriers

1. Oxide barriers

Superconducting tunnel junctions represent key elements in a number of electronic applications (Solymar, 1972) that span from single electron transistors (Grabert and Devoret, 1992) to Josephson devices (Barone and Paternó, 1982), just to mention two relevant examples. In addition, they are crucial building blocks of superconducting microrefrigerators (Leivo *et al.*, 1996; Nahum *et al.*, 1994) as well as of ultrasensitive microbolometers (Castellano *et al.*, 1997; Nahum and Martinis, 1993). The simplest picture of a tunnel junction can be given assuming a rectangular barrier of height ϕ_I and width w . The electron transport across the barrier can be easily described within the Wentzel-Kramers-Brillouin (WKB) approximation. The main results of this analysis are (Simmons, 1963b) i) an exponential dependence of the zero-bias junction conductance (G_0) on the barrier width, $G_0 \propto \exp[-2w\sqrt{2m^*\phi_I/\hbar}]$, where m^* is the effective mass of electrons in the barrier; ii) a quadratic voltage (V) dependence of the conductance $G(V)$; iii) a weak insulating-like quadratic dependence of G on the temperature T . In general, image forces acting on the electrons tunneling through the barrier will reduce both its height and its effective thickness (Simmons, 1963a). Criteria i)-iii) require that the dominant process through the barrier is direct tunneling and can be used to extract the junction parameters in a realistic situation (Brinkman *et al.*, 1970; Simmons, 1963a). Among the above given criteria, i) seems a necessary, but not sufficient condition to establish that tunneling is the dominant transport mechanism (Rabson *et al.*, 2001; Zhang and Rabson, 2004) due to the possible presence of pinholes (i.e., small regions where the insulator thickness vanishes) in the barrier, and it is generally accepted that only criterion iii) could be safely used to rule out the presence of such pinholes in the barrier (Jönsson-Åkerman *et al.*, 2000) and assess the junction quality (for instance, a reduction of junction conductance of about 15% on cooling from 295 K to 4.2 K is believed to be a good practical indication of high-quality AlO_x barriers (Gloos *et al.*, 2003, 2000); see also Secs. III and IV). An important figure of merit of tunnel contacts is the junction specific resistance $R_c = R_J A$, where $R_J \equiv G_0^{-1}$ is the contact resistance and A its area. A route to decrease R_c is to reduce w or choose materials with lower effective barrier height.

Among the available barrier materials, aluminum oxide (AlO_x) is probably the most widespread insulator used to fabricate metallic tunnel junctions because it can be easily and reliably grown starting from an Al film. Its main parameters are a typical barrier height $\phi_I \approx 2$ eV, although values in the range $0.1\ldots 8.6$ eV have been re-

ported (Barner and Ruggiero, 1989; Gundlach and Hölz, 1971; Kadlec and Kadlec, 1975; Lau and Coleman, 1981) and a dielectric constant smaller than that of bulk Al_2O_3 (4.5...8.9 at 295 K (Bolz and Tuve, 1983)). Several methods are currently exploited to fabricate high-quality (i.e., highly uniform and pinhole-free) aluminum oxide barriers such as *in situ* vacuum natural oxidation (Matsuda *et al.*, 1999; Parkin *et al.*, 1999; Sun *et al.*, 2000; Tsuge and Mitsuzuka, 1997; Zhang *et al.*, 2001), oxidation in air (Miyazaki and Tezuka, 1995) and plasma oxidation (Gallagher *et al.*, 1997; Moodera *et al.*, 1995; Sun *et al.*, 1999) of a thin Al layer (typically below 2 nm), just to mention the most common techniques. The latter two methods lead in general to higher R_c values (of the order of several $\text{k}\Omega\mu\text{m}^2$ or larger) with respect to natural oxidation. The natural oxidation allows to achieve the desired R_c by simply changing the oxidation pressure and time (R_c also depends on the original thickness of the Al layer), and almost any R_c value can be produced by following such a procedure. Aluminum oxide junctions with R_c values as low as some tens of $\Omega\mu\text{m}^2$ or lower are currently realized with natural oxidation (Childress *et al.*, 2001; Deac *et al.*, 2004; Fujikata *et al.*, 2001; Liu *et al.*, 2003; Parkin *et al.*, 1999; Sun *et al.*, 2000; Zhang *et al.*, 2001). However, low- R_c junctions are more prone to defects or pinholes in the barrier that dramatically degrade their performance. Promising methods and materials have been proposed for the fabrication of oxidized barriers with R_c as low as some $\Omega\mu\text{m}^2$ among which we mention junctions made of ZrAlO_x (Liu *et al.*, 2003; Wang *et al.*, 2002) and HfAlO_x (Wang *et al.*, 2003).

2. Schottky barriers

The metal-semiconductor (NSm) junction is an issue that dates back more than 60 years (Schottky, 1939), but still nowadays represents a relevant topic both in the physics of semiconductors (Brennan, 1999; Lüth, 2001; Rhoderick and Williams, 1988; Sze, 1981, 1985) and in device applications (Millman and Grabel, 1987; Singh, 1994). The two most important types of NSm junctions are the Schottky barrier (SB), showing a *rectifying* diode-like I-V characteristics, and the *ohmic* contact, whose I-V is almost linear. Most of NSm junctions, with a few exceptions such as contacts with InAs, InSb and $\text{In}_x\text{Ga}_{1-x}\text{As}$ (for $x \geq 70\%$) (Kajiyama *et al.*, 1973), are affected by the presence of the SB that drastically affect their electric behavior. For most semiconductors (in the following we concentrate on *n*-type semiconductors but similar conclusions can be given for *p*-type ones), the SB height (ϕ_{SBn}) has a rather weak dependence upon the metal used for the contact; for instance, for metal/*n*-Si contacts $\phi_{SBn} = 0.7...0.85$ eV, while for metal/*n*-GaAs contacts $\phi_{SBn} = 0.7...0.9$ eV (Rhoderick and Williams, 1988; Singh, 1994). This fact is explained in terms of the Fermi-level pinning at the NSm interface (Bardeen, 1947; Heine, 1965; Mönch, 1990).

The current across a Schottky junction depends on a number of different mechanisms. In the limit where thermionic emission dominates the electric transport, the rectifying action of a biased NSm junction is described as $I(V) = I_s[\exp(eV/k_B T) - 1]$, where the detailed expression for the saturation current I_s depends on the assumptions made on carrier transport (Brennan, 1999; Sze, 1981, 1985). In such a case the junction specific resistance is $R_c \propto T^{-1}\exp(e\phi_{SBn}/k_B T)$, thus meaning that it can be lowered mainly by decreasing ϕ_{SBn} (typical R_c values at doping levels $N_D \leq 10^{17} \text{ cm}^{-3}$ for metal/*n*-Si contacts are of the order of $10^{11}...10^{13} \Omega\mu\text{m}^2$ almost independent of N_D). By contrast, tunneling across the SB can be the dominating transport mechanism if the semiconductor is heavily doped. In such a case $I(V) \propto \exp[-\alpha(\phi_{SBn} - V)/\sqrt{N_D}]$, with $\alpha = 2\hbar^{-1}\sqrt{m^*\epsilon}$ where m^* is the semiconductor effective mass and ϵ the dielectric permittivity, i.e., the junction is not rectifying and the current is proportional to V for small voltages. The contact is thus said to be ohmic and yields $R_c \propto \exp(\alpha\phi_{SBn}/\sqrt{N_D})$. This shows that R_c can be reduced up to a large extent by lowering the SB height and doping as heavily as possible (again, for metal/*n*-Si contacts and $N_D \geq 10^{19} \text{ cm}^{-3}$, R_c can be in the range $10^2...10^8 \Omega\mu\text{m}^2$). All this shows the advantage of using NSm contacts owing to the possibility of tuning the contact specific resistance over several orders of magnitude (from metallic-like to tunnel-like characteristics) through a careful choice of metal-semiconductor combinations and proper doping levels. This trick is commonly exploited to control the NSm interface resistance in current semiconductor technology, although heavy doping of the semiconductor just in proximity to the metal is often preferred (Giazotto *et al.*, 2001a,b; Kastalsky *et al.*, 1991; Shannon, 1976; Taboryski *et al.*, 1996).

VII. FUTURE PROSPECTS

Low temperature solid-state cooling is still at its infancy, although operation of a number of individual principles and techniques have been demonstrated to work successfully. Yet combinations of cascaded micro-refrigerators over wider temperature ranges employing several stages, or combinations of different refrigeration principles, e.g., fluidic coolers together with electronic coolers, do not exist. In principle, compact low-power refrigerators could be fabricated using micro-machined helium-based fluidic refrigerators, for instance based on Joule-Thomson process (Little, 1984), and these devices could then be directly precooling NIS-refrigerators with niobium ($T_c = 9$ K) as a superconductor. A lot of engineering effort is, however, needed to make this approach work in practise as a targeted micro-refrigerator.

The solid-state micro-circuits have already proven to yield new operation principles and previously unknown concepts have been discovered in cryogenic devices, as demonstrated throughout this review. We believe that

what was demonstrated here is just a presentation of a beginning of a new era in low temperature physics and instrumentation. As possible new classes of devices we could mention those utilizing thermodynamic Carnot cycles with electrons. Brownian heat engines with electrons are predicted to achieve efficiencies close to ideal (Humphrey *et al.*, 2002). It may be possible in the future to make use of other types of gated cycles where energy selective extraction of electrons is producing the refrigeration effect. As a conceivable example, a combination of Coulomb effects and superconducting energy gap could form the basis of operation of a refrigerator where cooling power would be proportional to the operating frequency of the gate cycle. Such a device would thus be principally different from the static electronic refrigerators presented in this review, where a DC bias is in charge of the redistribution of hot electrons.

At low temperatures, additional relaxation channels besides the electron-phonon scattering, such as coupling between electrons and photons, become important. More knowledge is needed on these mechanisms.

In Subs. V.C.7, we describe how the non-equilibrium shape of the distribution function sometimes leads to improved characteristics of the device. It would be interesting to see if such effects could be employed to improve also the properties of the radiation detectors or other practical devices.

The presently obvious application fields of electronic micro-refrigerators include astronomical detectors both in space as well as those based on the earth, materials characterization instrumentation, e.g., those devices employing ultra high resolution x-ray micro-analysis, and security instrumentation, e.g., concealed weapon search on the airports. It is, however, evident that once realized in a user-friendly and economic way, refrigeration becomes very important in high-tech based industry in a much broader perspective. Low temperature electronics and superconducting devices are often characterized by their undeniably unique possibilities, but they are often superior to the room temperature ones also in speed and power consumption. Therefore, mesoscopic on-spot refrigerators to attain the low temperatures forming the basis of these instruments are urgently needed.

Acknowledgments

We thank H. Courtois, R. Fazio, F. Hekking, M. Paalanen, F. Taddei and P. Virtanen for their insightful comments and for critically reading the manuscript. D. Anghel, A. Anthore, F. Beltram, M. Feigelman, E. Grossman, K. Irwin, M. Meschke, A. J. Miller, S. Nam, D. Schmidt, and J. Ullom are gratefully acknowledged for enlightening discussions. This work was supported by the Academy of Finland.

References

- Adams, A. C., 1983, in *VLSI Technology*, edited by S. M. Sze (McGraw-Hill, New York), p. 93.
- Adams, A. C., 1986, in *Reduced Temperature Processing for VLSI*, edited by R. Reif and G. R. Srinivasan (The Electrochemical Society, New Jersey), p. 111.
- Adams, A. C., F. B. Alexander, C. D. Capio, and T. E. Smith, 1981, *J. Electrochem. Soc.* **128**, 1545.
- Akerib, D. S., J. Alvaro-Dean, M. S. Armel, M. J. Attisha, L. Baudis, D. A. Bauer, A. I. Bolozdynya, P. L. Brink, R. Bunker, B. Cabrera, D. O. Caldwell, J. P. Castle, *et al.*, 2003, *Phys. Rev. D* **68**, 082002.
- Ali, S., L. D. Cooley, D. McCammon, K. L. Nelms, J. Peck, D. Prober, D. Swetz, P. T. Timbie, and D. van der Weide, 2003, *IEEE Trans. Appl. Superc.* **13**, 184.
- Altshuler, B. L., and A. G. Aronov, 1985, in *Electron-electron interactions in disordered systems*, edited by A. L. Efros and M. Pollak (Elsevier, Amsterdam), chapter 1, p. 1.
- Ambegaokar, V., and A. Baratoff, 1963, *Phys. Rev. Lett.* **1**, 486.
- Andreev, A. F., 1964a, *Zh. Eksp. Teor. Fiz.* **46**, 1823.
- Andreev, A. F., 1964b, *Sov. Phys. JETP* **19**, 1228.
- Andrews, D. H., 1938, 132.
- Andrews, D. H., 1941, *Phys. Rev.* **59**, 1045.
- Angelescu, D. E., M. C. Cross, and M. L. Roukes, 1998, *Superlattices Microstruct.* **23**, 673.
- Anghel, D. V., and L. Kuzmin, 2003, *Appl. Phys. Lett.* **82**, 295.
- Anghel, D. V., A. Luukanen, and J. P. Pekola, 2001, *Appl. Phys. Lett.* **78**, 556.
- Anghel, D. V., and M. Manninen, 1999, *Phys. Rev. B* **59**, 9854.
- Anghel, D. V., and J. P. Pekola, 2001, *J. Low Temp. Phys.* **123**, 197.
- Anghel, D. V., J. P. Pekola, M. M. Leivo, J. K. Suoknuuti, and M. Manninen, 1998, *Phys. Rev. Lett.* **81**, 2958.
- Anthore, A., F. Pierre, H. Pothier, and D. Esteve, 2003, *Phys. Rev. Lett.* **90**, 076806.
- Arthur, J. R., 1968, *J. Appl. Phys.* **39**, 4032.
- Arutyunov, K. Y., T. I. Suppala, J. K. Suoknuuti, and J. P. Pekola, 2000, *J. Appl. Phys.* **88**, 326.
- Ashcroft, N. W., and N. D. Mermin, 1976, *Solid State Physics* (Saunders College, Philadelphia).
- Aumentado, J., V. Chandrasekhar, J. Eom, P. M. Baldo, and L. E. Rehn, 1999, *Appl. Phys. Lett.* **75**, 3554.
- Averin, D. V., and K. K. Likharev, 1986, in *SQUID'85: Superconducting Quantum Interference Devices and Their Applications*, edited by H.-D. Hahlbohm and H. Lubbig (deGruyter, Berlin), p. 345.
- Badolato, A., F. Giazotto, M. Lazzarino, P. Pingue, F. Beltram, C. Lucheroni, and R. Fazio, 2000, *Phys. Rev. B* **62**, 9831.
- Bakker, S. J. M., E. van der Drift, T. M. Klapwijk, H. M. Jaeger, and S. Radelaar, 1994, *Phys. Rev. B* **49**, 13275.
- Balandin, A. A., and O. L. Lazarenkova, 2003, *Appl. Phys. Lett.* **82**, 415.
- Baranger, H. U., and P. A. Mello, 1994, *Phys. Rev. Lett.* **73**, 142.
- Bardas, A., and D. Averin, 1995, *Phys. Rev. B* **52**, 12873.
- Bardeen, J., 1947, *Phys. Rev.* **71**, 717.
- Barner, J. B., and S. T. Ruggiero, 1989, *Phys. Rev. B* **39**, 2060.

- Barone, A., and G. Paternó, 1982, *Physics and Applications of the Josephson Effect* (John Wiley & Sons, New York).
- Baselmans, J. J. A., 2002, *Controllable Josephson Junctions* (Ph. D. thesis, University of Groningen, The Netherlands).
- Baselmans, J. J. A., T. T. Heikkilä, B. J. van Wees, and T. M. Klapwijk, 2002a, Phys. Rev. Lett. **89**, 207002.
- Baselmans, J. J. A., A. F. Morpurgo, B. J. van Wees, and T. M. Klapwijk, 1999, Nature **397**, 43.
- Baselmans, J. J. A., B. J. van Wees, and T. M. Klapwijk, 2001a, Appl. Phys. Lett. **79**, 2940.
- Baselmans, J. J. A., B. J. van Wees, and T. M. Klapwijk, 2001b, Phys. Rev. B **63**, 094504.
- Baselmans, J. J. A., B. J. van Wees, and T. M. Klapwijk, 2002b, Phys. Rev. B **65**, 224513.
- Beenakker, C. W. J., 1992, Phys. Rev. B **46**, 12841.
- Belitz, D., 1987, Phys. Rev. B **36**, 2513.
- Belitz, D., and T. R. Kirkpatrick, 1994, Rev. Mod. Phys. **66**, 261.
- Belzig, W., F. K. Wilhelm, C. Bruder, G. Schön, and A. D. Zaikin, 1999, Superlatt. Microstruct. **25**, 1251.
- Bergsten, T., T. Claeson, and P. Delsing, 2001, Appl. Phys. Lett. **78**, 1264.
- Bezuglyi, E. V., E. N. Bratus', V. S. Shumeiko, G. Wendin, and H. Takayanagi, 2000, Phys. Rev. B **62**, 14439.
- Bezuglyi, E. V., and V. Vinokur, 2003, Phys. Rev. Lett. **91**, 137002.
- Bhushan, B., 2004, *Springer Handbook of Nanotechnology* (Springer, Berlin).
- Birk, H., M. J. M. de Jong, and C. Schönenberger, 1995, Phys. Rev. Lett. **75**, 1610.
- Blamire, M. G., E. C. G. Kirk, J. E. Evetts, and T. M. Klapwijk, 1991, Phys. Rev. Lett. **66**, 220.
- Blanter, Y., and M. Büttiker, 2000, Phys. Rep. **336**, 1.
- Blencowe, M. P., 1999, Phys. Rev. B **59**, 4992.
- Bolz, R. E., and G. L. Tuve, 1983, *Handbook of Tables for Applied Engineering Science* (CRC Press, Boca Raton).
- Booth, N., and D. J. Goldie, 1996, Supercond. Sci. Technol. **9**, 493.
- Bourgeois, O., S. E. Skipetrov, F. Ong, and J. Chaussy, 2005, Phys. Rev. Lett. **94**, 057007.
- Bravin, M., M. Bruckmayer, C. Bucci, S. Cooper, S. Giordano, F. von Feilitzsch, J. Höhne, J. Jochum, V. Jörgens, R. Keeling, H. Kraus, M. Loidl, *et al.*, 1999, Astroparticle Physics **12**, 107.
- Brener, N. E., J. M. Tyler, J. Callaway, D. Bagayoko, and G. L. Zhao, 2000, Phys. Rev. B **61**, 16582.
- Brennan, K. F., 1999, *The Physics of Semiconductors* (Cambridge University Press, Cambridge).
- Brewer, G., 1980, *Electron-Beam Technology in Microelectronic Fabrication* (Academic Press, San Diego).
- Brinkman, W. F., R. C. Dynes, and J. M. Rowell, 1970, J. Appl. Phys. **41**, 1915.
- Brown, E., 1984, J. Appl. Phys. **55**, 213.
- Bulaevskii, L. N., V. V. Kuzii, and A. A. Sobyenin, 1977, Pis'ma Zh. Eksp. Teor. Phys. **25**, 314.
- Buonomo, B., R. Leoni, M. G. Castellano, F. Mattioli, G. Torrioli, L. D. Gaspare, and F. Evangelisti, 2003, J. Appl. Phys. **94**, 7784.
- Campbell, S. A., 2001, *The Science, and Engineering of Microelectronic Fabrication* (Oxford University Press, New York).
- Camus, P., L. Bergé, L. Dumoulin, S. Marnieros, and J. P. Torre, 2000, Nuclear Instruments and Methods in Physics Research A **444**, 419.
- Cantile, M., L. Sorba, P. Faraci, S. Yildirim, G. Biasiol, G. Bratina, A. Franciosi, T. J. Miller, M. I. Nathan, and L. Tapfer, 1994a, J. Vac. Sci. Technol. B **12**, 2653.
- Cantile, M., L. Sorba, S. Yildirim, P. Faraci, G. Biasiol, A. Franciosi, T. J. Miller, and M. I. Nathan, 1994b, Appl. Phys. Lett. **64**, 988.
- Capasso, F., 1990, *Physics of Quantum Electron Devices* (Springer, Berlin).
- Castellano, M. G., R. Leoni, G. Torrioli, P. Carelli, A. Gerardino, and F. Melchiorri, 1997, IEEE Trans. Appl. Supercond. **7**, 3251.
- Chang, C. Y., Y. K. Fang, and S. M. Sze, 1971, Solid-State Electron. **14**, 541.
- Chang, L. L., and R. Ludeke, 1975, in *Epitaxial Growth, Part A*, edited by J. W. Mathews (Academic Press, San Diego), p. 37.
- Chapman, B., and S. Mangano, 1988, in *Handbook of Thin-Film Deposition Processes and Techniques*, edited by K. K. Schuegraf (Noyes Publications, Norwich), p. 291.
- Chapman, B. N., 1980, *Glow Discharge Processes: Sputtering & Plasma Etching* (John Wiley & Sons, New York).
- Charlat, P., H. Courtois, P. Gandit, D. Mailly, A. F. Volkov, and B. Pannetier, 1996, Phys. Rev. Lett. **77**, 4950.
- Chervenak, J., K. Irwin, E. Grossman, J. M. Martinis, and C. Reintsema, 1999, Appl. Phys. Lett. **74**, 4043.
- Chi, C. C., and J. Clarke, 1979, Phys. Rev. B **20**, 4465.
- Childress, J. R., M. M. Schwickert, R. E. Fontana, M. K. Ho, P. M. Rice, and B. A. Gurney, 2001, J. Appl. Phys. **89**, 7353.
- Cho, A. Y., 1970, J. Vac. Sci. Technol. **8**, S31.
- Cho, A. Y., 1979, J. Vac. Sci. Technol. **16**, 275.
- Cho, A. Y., and J. R. Arthur, 1975, Prog. Solid-State Chemistry **10**, 157.
- Chouvaev, D., L. Kuzmin, and M. Tarasov, 1999, Supercond. Sci. Technol. **12**, 985.
- Chow, R., W. A. Lanford, W. Ke-Ming, and R. S. Rosler, 1982, J. Appl. Phys. **53**, 5630.
- Clark, A. M., N. A. Miller, A. Williams, S. T. Ruggiero, G. C. Hilton, L. R. Vale, J. A. Beall, K. D. Irwin, and J. N. Ullom, 2005, Appl. Phys. Lett. **86**, 173508.
- Clark, A. M., A. Williams, S. T. Ruggiero, M. L. van den Berg, and J. N. Ullom, 2004, Appl. Phys. Lett. **84**, 625.
- Clarke, J., P. Richards, and N.-H. Yeh, 1977, Appl. Phys. Lett. **30**, 664.
- Cloughton, N. R., and C. J. Lambert, 1996, Phys. Rev. B **53**, 6605.
- Coey, J. M. D., A. E. Berkowitz, L. I. Balcells, F. F. Putris, and A. Barry, 1998, Phys. Rev. Lett. **80**, 3815.
- Coey, J. M. D., and S. Sanvito, 2004, J. Phys. D: Appl. Phys. **37**, 988.
- Colclaser, R. A., 1980, *Microelectronics: Processing, and Device Design* (John Wiley & Sons, New York).
- Costa, J. C., F. Williamson, T. J. Miller, K. Beyzavi, M. I. Nathan, D. S. L. Mui, S. Strite, and H. Morkoc, 1991, Appl. Phys. Lett. **58**, 382.
- Cotler, T. J., and M. E. Elta, 1990, IEEE Circuits & Devices Mag. **6**, 38.
- Cutler, M., and N. F. Mott, 1969, Phys. Rev. **181**, 1336.
- Czocharski, J., 1918, Z. Phys. Chem. **92**, 219.
- Davis, Q. V., J. L. Clarke, and R. G. T. Morris, 1964, Rev. Sci. Instrum. **35**, 561.
- De Franceschi, S., F. Beltram, C. Marinelli, L. Sorba, M. Lazarino, B. H. Müller, and A. Franciosi, 1998a, Appl. Phys. Lett. **72**, 1196.

- De Franceschi, S., F. Giazotto, F. Beltram, L. Sorba, M. Lazzarino, and A. Franciosi, 1998b, *Appl. Phys. Lett.* **73**, 3890.
- De Franceschi, S., F. Giazotto, F. Beltram, L. Sorba, M. Lazzarino, and A. Franciosi, 2000, *Phil. Mag. B* **80**, 817.
- de Korte, P. A. J., J. J. van Baar, N. H. R. Baars, F. E. Bakker, W. M. Bergmann Tiest, M. P. Bruijn, A. Germeau, H. F. C. Hoevers, M. Kiviranta, E. Krouwer, J. van der Kuur, M. P. Lubbers, *et al.*, 2004, in *Optical and Infrared Detectors for Astronomy*, edited by J. Garnett and J. Beletic (SPIE), volume 5501, pp. 167–176.
- Deac, A., O. Redon, R. C. Sousa, B. Dieny, J. P. Nozières, Z. Zhang, Y. Liu, and P. P. Freitas, 2004, *J. Appl. Phys.* **95**, 6792.
- Dedkov, Y. S., M. Fonine, C. Konig, U. Rudiger, G. Guntherodt, S. Senz, and D. Hesse, 2002, *Appl. Phys. Lett.* **80**, 4181.
- Deiker, S. W., W. Doriese, G. C. Hilton, K. D. Irwin, W. H. Rippard, J. N. Ullom, L. R. Vale, S. T. Ruggiero, A. Williams, and B. A. Young, 2004, *Appl. Phys. Lett.* **85**, 2137.
- Denlinger, D. W., E. N. Abarra, K. Allen, P. W. Rooney, M. T. Messer, S. K. Watson, and F. Hellman, 1994, *Rev. Sci. Instrum.* **65**, 946.
- Devyatov, I. A., M. Y. Kupriyanov, L. S. Kuzmin, A. A. Golubov, and M. Willander, 2000, *J. Exp. Theor. Phys.* **90**, 1050.
- Dikin, D. A., S. Jung, and V. Chandrasekhar, 2002a, *Phys. Rev. B* **65**, 012511.
- Dikin, D. A., S. Jung, and V. Chandrasekhar, 2002b, *Europhys. Lett.* **57**, 564.
- DiSalvo, F. J., 1999, *Science* **285**, 703.
- Dolan, G. J., 1977, *Appl. Phys. Lett.* **31**, 337.
- Dolan, G. J., and J. H. Dunsmuir, 1988, *Physica B* **152**, 7.
- Doriese, W. B., J. A. Beall, S. Deiker, W. D. Duncan, L. Ferreira, G. C. Hilton, K. D. Irwin, C. D. Reintsema, J. N. Ullom, L. R. Vale, and Y. Xu, 2004, *Appl. Phys. Lett.* **85**, 4762.
- Dubos, P., H. Courtois, B. Pannetier, F. K. Wilhelm, A. D. Zaikin, and G. Schön, 2001, *Phys. Rev. B* **63**, 064502.
- Dun, H., P. Pan, F. R. White, and R. W. Douse, 1981, *J. Electrochem. Soc.* **128**, 1556.
- Duncan, W., W. S. Holland, M. D. Audley, M. Cliffe, T. Hodson, B. D. Kelly, X. Gao, D. C. Gostick, M. MacIntosh, H. McGregor, T. Peacocke, K. D. Irwin, *et al.*, 2003, in *Proceedings of the SPIE, Volume 4855, Millimeter and Submillimeter Detectors for Astronomy*, edited by T. G. Phillips and J. Zmuidzinas (SPIE), pp. 19–29.
- Dynes, R. C., J. P. Garno, G. B. Hertel, and T. P. Orlando, 1984, *Phys. Rev. Lett.* **53**, 2437.
- Echternach, P. M., M. R. Thoman, C. M. Gould, and H. M. Bozler, 1992, *Phys. Rev. B* **46**, 10339.
- Edwards, H. L., Q. Niu, G. A. Georgakis, and A. L. de Lozanne, 1995, *Phys. Rev. B* **52**, 5714.
- Edwards, H. L., Q. Niu, and A. L. de Lozanne, 1993, *Appl. Phys. Lett.* **63**, 1815.
- Eom, J., C.-J. Chien, and V. Chandrasekhar, 1998, *Phys. Rev. Lett.* **81**, 437.
- Fan, X., G. Zeng, C. LaBounty, J. E. Bowers, E. Croke, C. C. Ahn, S. Huxtable, A. Majumdar, and A. Shakouri, 2001, *Appl. Phys. Lett.* **78**, 1580.
- Farhangfar, S., K. P. Hirvi, J. P. Kauppinen, J. P. Pekola, J. J. Toppari, D. V. Averin, and A. N. Korotkov, 1997, *J. Low Temp. Phys.* **108**, 191.
- Fee, M. G., 1993, *Appl. Phys. Lett.* **62**, 1161.
- Ferry, D. K., and S. M. Goodnick, 1997, *Transport in Nanostructures* (Cambridge University Press, Cambridge).
- Fisher, P. A., J. N. Ullom, and M. Nahum, 1995, *J. Low Temp. Phys.* **101**, 561.
- Fisher, P. A., J. N. Ullom, and M. Nahum, 1999, *Applied Physics Letters* **74**, 2705.
- Fleischmann, A., T. Daniyarov, H. Rotzinger, M. Linck, C. Enss, and G. M. Seidel, 2003, *Rev. Sci. Instrum.* **74**, 3947.
- Fominaya, F., T. Fournier, P. Gandit, and J. Chaussy, 1997, *Rev. Sci. Instrum.* **68**, 4191.
- Frank, B., and W. Krech, 1997, *Phys. Lett. A* **235**, 281.
- Fujikata, J., T. Ishi, S. Mori, K. Matsuda, K. Mori, H. Yokota, K. Hayashi, M. Nakada, A. Kamijo, and K. Ohashi, 2001, *J. Appl. Phys.* **89**, 7558.
- Fulton, T. A., and G. J. Dolan, 1987, *Phys. Rev. Lett.* **59**, 109.
- Gallagher, W. J., S. S. P. Parkin, Y. Lu, X. P. Bian, A. Marley, K. P. Roche, R. A. Altman, S. A. Rishton, C. Jahnes, T. M. Shaw, and G. Xiao, 1997, *J. Appl. Phys.* **81**, 3741.
- Gandhi, S. K., 1983, *VLSI Fabrication Principles* (John Wiley & Sons, New York).
- Giaever, I., and H. R. Zeller, 1968, *Phys. Rev. Lett.* **20**, 1504.
- Giazotto, F., M. Cecchini, P. Pingue, F. Beltram, M. Lazzarino, D. Orani, S. Rubini, and A. Franciosi, 2001a, *Appl. Phys. Lett.* **78**, 1772.
- Giazotto, F., T. T. Heikkilä, F. Taddei, R. Fazio, J. P. Pekola, and F. Beltram, 2004a, *J. Low. Temp. Phys.* **136**, 435.
- Giazotto, F., T. T. Heikkilä, F. Taddei, R. Fazio, J. P. Pekola, and F. Beltram, 2004b, *Phys. Rev. Lett.* **92**, 137001.
- Giazotto, F., and J. P. Pekola, 2005, *J. Appl. Phys.* **97**, 023908.
- Giazotto, F., P. Pingue, and F. Beltram, 2003a, *Mod. Phys. Lett.* **17**, 955.
- Giazotto, F., P. Pingue, F. Beltram, M. Lazzarino, D. Orani, S. Rubini, and A. Franciosi, 2001b, *Phys. Rev. Lett.* **87**, 216808.
- Giazotto, F., F. Taddei, R. Fazio, and F. Beltram, 2002, *Appl. Phys. Lett.* **80**, 3784.
- Giazotto, F., F. Taddei, R. Fazio, and F. Beltram, 2005, in *Realizing Controllable Quantum States*, edited by H. Takayanagi and J. Nitta (World Scientific, Singapore), p. 123.
- Giazotto, F., F. Taddei, T. T. Heikkilä, R. Fazio, and F. Beltram, 2003b, *Appl. Phys. Lett.* **83**, 2877.
- Gildemeister, J. M., A. T. Lee, and P. L. Richards, 1999, *Appl. Phys. Lett.* **74**, 868.
- Gloos, K., P. J. Koppinen, and J. P. Pekola, 2003, *J. Phys.: Condens. Matter* **15**, 1733.
- Gloos, K., R. S. Poikolainen, and J. P. Pekola, 2000, *Appl. Phys. Lett.* **77**, 2915.
- Goetz, A., 1939, *Phys. Rev.* **55**, 1270.
- Goldsmid, H. J., K. K. Gopinathan, D. N. Matthews, K. N. R. Taylor, and C. A. Baird, 1988, *J. of Phys. D* **21**, 344.
- Goldsmid, H. J., and A. S. Gray, 1979, *Cryogenics* **19**, 289.
- Goltsev, A. V., D. M. Rowe, V. L. Kuznetsov, L. A. Kuznetsova, and G. Min, 2003, *Appl. Phys. Lett.* **82**, 2272.
- Golubev, D., and L. Kuzmin, 2001, *J. Appl. Phys.* **89**, 6464.
- Golubev, D., and A. Vasenko, 2002, in *International Workshop on Superconducting Nano-Electronics Devices*, edited by J. P. Pekola, B. Ruggiero, and P. Silvestrini (Kluwer Academic/Plenum Publishers, New York), p. 165.
- Golubov, A. A., M. Y. Kupriyanov, and E. Il'ichev, 2004, *Rev. Mod. Phys.* **76**, 411.
- Golubov, A. A., F. K. Wilhelm, and A. D. Zaikin, 1997, *Phys.*

- Rev. B **55**, 1123.
- Golwala, S., J. Jochum, and B. Sadoulet, 1997, in *Proceedings of the 7th International Workshop on Low Temperature Detectors LTD-7* (MPI Physik, Munich, Germany), pp. 64–65.
- Göppert, G., Y. M. Galperin, B. L. Altshuler, and H. Grabert, 2002, Phys. Rev. B **66**, 195328.
- Göppert, G., and H. Grabert, 2001, Phys. Rev. B **64**, 033301.
- Göppert, G., and H. Grabert, 2003, Phys. Rev. B **68**, 193301.
- Grabert, H., and M. H. Devoret, 1992, *Single Charge Tunneling* (Plenum Press, New York).
- Grant, R. W., and J. R. Waldrop, 1988, Appl. Phys. Lett. **52**, 1794.
- Gray, K. E., 1978, Solid State Commun. **26**, 633.
- de Groot, R. A., F. M. Mueller, P. G. van Engen, and K. H. J. Buschow, 1983, Phys. Rev. Lett. **50**, 2024.
- Grossman, E. N., J. E. Sauvageau, and D. G. McDonald, 1991, Appl. Phys. Lett. **59**, 3225.
- Grove, A. S., 1967, *Physics and Technology of Semiconductor Devices* (Wiley, New York).
- Gundlach, K. H., and J. Hölz, 1971, Surf. Sci. **27**, 125.
- Harris, R. E., 1974, Phys. Rev. B **10**, 84.
- den Hartog, S. G., B. J. van Wees, T. M. Klapwijk, Y. V. Nazarov, and G. Borghs, 1997, Phys. Rev. B **56**, 13738.
- Harutyunyan, S. R., V. H. Vardanyan, A. S. Kuzanyan, V. R. Nikoghosyan, S. Kunii, K. S. Wood, and A. M. Gulian, 2003, Appl. Phys. Lett. **83**, 2142.
- Heikkilä, T. T., J. Särkkä, and F. K. Wilhelm, 2002, Phys. Rev. B **66**, 184513.
- Heikkilä, T. T., M. P. Stenberg, M. M. Salomaa, and C. J. Lambert, 2000, Physica B **284–8**, 1862.
- Heikkilä, T. T., T. Vänskä, and F. K. Wilhelm, 2003, Phys. Rev. B **67**, 100502.
- Heine, V., 1965, Phys. Rev. **138**, A1689.
- Heslinga, D. R., and T. M. Klapwijk, 1989, Appl. Phys. Lett. **54**, 1048.
- Heslinga, D. R., and T. M. Klapwijk, 1992, Solid State Commun. **84**, 739.
- Heslinga, D. R., and T. M. Klapwijk, 1993, Physica B **47**, 5157.
- Hess, D. W., 1984, J. Vac. Sci. Technol. **A2**, 244.
- Hicks, L. D., and M. S. Dresselhaus, 1993a, Phys. Rev. B **47**, 16631.
- Hicks, L. D., and M. S. Dresselhaus, 1993b, Phys. Rev. B **47**, 12727.
- Hicks, L. D., T. C. Harman, and M. S. Dresselhaus, 1993, Appl. Phys. Lett. **63**, 3230.
- Hicks, L. D., T. C. Harman, X. Sun, and M. S. Dresselhaus, 1996, Phys. Rev. B **53**, R10493.
- Hishinuma, Y., T. H. Geballe, B. Y. Mozyzhes, and T. W. Kenny, 2001, Appl. Phys. Lett. **78**, 2572.
- Hishinuma, Y., T. H. Geballe, B. Y. Mozyzhes, and T. W. Kenny, 2003, J. Appl. Phys. **94**, 4690.
- Hishinuma, Y., B. Y. Mozyzhes, T. H. Geballe, and T. W. Kenny, 2002, Appl. Phys. Lett. **81**, 4242.
- Hoovers, H., A. Bento, M. Bruijn, L. Gottardi, M. Korevaar, W. Mels, and P. Korte, 2000, Appl. Phys. Lett. **77**, 4422.
- Hollahan, J. R., 1974, J. Electrochem. Soc. **126**, 931.
- Holland, L., 1958, *Vacuum Deposition of Thin Films* (Chapman & Hall Ltd., London).
- Holland, W. S., W. Duncan, B. D. Kelly, K. D. Irwin, A. J. Walton, P. A. R. Ade, and E. I. Robson, 2003, in *Proceedings of the SPIE, Volume 4855, Millimeter and Submillimeter Detectors for Astronomy*, edited by T. G. Phillips and J. Zmuidzinas (SPIE), volume 4855, pp. 1–18.
- Holmes, W., J. M. Gildemeister, P. L. Richards, and V. Kotsubo, 1998, Applied Physics Letters **72**, 2250.
- Houzet, M., and F. Pistolesi, 2004, Phys. Rev. Lett. **92**, 107004.
- Howard, R. E., H. G. Craighead, L. D. Jackel, and P. M. Mankiewich, 1983, J. Vac. Sci. Technol. B **1**, 1101.
- Huang, J., F. Pierre, T. T. Heikkilä, F. K. Wilhelm, and N. O. Birge, 2002, Phys. Rev. B **66**, 020507.
- Huard, B., A. Anthore, F. Pierre, H. Pothier, N. O. Birge, and D. Esteve, 2004, Solid State Communications **131**, 599.
- Humphrey, T. E., R. Newbury, R. P. Taylor, and H. Linke, 2002, Phys. Rev. Lett. **89**, 116801.
- Hunt, C. L., J. Bock, P. Day, A. Goldin, A. Lange, H. LeDuc, A. Vayonakis, and J. Zmuidzinas, 2003, in *Millimeter and Submillimeter Detectors for Astronomy*, edited by T. G. Phillips and J. Zmuidzinas (SPIE), volume 4855, pp. 318–321.
- Hwang, T.-L., S. Schwarz, and D. Rutledge, 1979, Appl. Phys. Lett. **34**, 773.
- Irwin, K. D., 1995, Appl. Phys. Lett. **66**, 1998.
- Irwin, K. D., and G. C. Hilton, 2005, in *Cryogenic Particle Detection*, edited by C. Enss (Springer, Berlin, Heidelberg (in press)), volume 99 of *Topics Appl. Phys.*, ISBN 3540201130, p. 63.
- Irwin, K. D., G. C. Hilton, D. A. Wollman, and J. M. Martinis, 1996, Appl. Phys. Lett. **69**, 1945.
- Irwin, K. D., G. C. Hilton, D. A. Wollman, and J. M. Martinis, 1998, J. Appl. Phys. **83**, 3978.
- Irwin, K. D., S. W. Nam, B. Cabrera, B. Chugg, G. Park, R. P. Welty, and J. M. Martinis, 1995a, IEEE Trans. Appl. Superc. **5**, 2690.
- Irwin, K. D., S. W. Nam, B. Cabrera, B. Chugg, and B. A. Young, 1995b, Rev. Sci. Instrum. **66**, 5322.
- Jackel, L. D., R. E. Howard, P. M. Mankiewich, H. G. Craighead, and R. W. Epworth, 1984, Appl. Phys. Lett. **45**, 698.
- Jaeger, C. J., 2002, *Introduction to Microelectronic Fabrication* (Prentice Hall, New Jersey).
- Jamamoto, N., and R. Shimizu, 1983, J. Appl. Phys. **54**, 3855.
- Jensen, K. F., 1989, in *Microelectronics Processing: Chemical Engineering Aspects*, edited by D. W. Hess and K. F. Jensen (American Chemical Society, Washington), p. 199.
- Ji, Y., G. J. Strijkers, F. Y. Yang, C. L. Chien, J. M. Byers, A. Anguelouch, G. Xiao, and A. Gupta, 2001, Phys. Rev. Lett. **86**, 5585.
- Jiang, Z., and V. Chandrasekhar, 2004, [cond-mat/0408419].
- Jiang, Z., and V. Chandrasekhar, 2005a, [cond-mat/0501478].
- Jiang, Z., and V. Chandrasekhar, 2005b, Phys. Rev. Lett. **94**, 147002.
- Jiang, Z., H. Lim, V. Chandrasekhar, and J. Eom, 2003, Appl. Phys. Lett. **83**, 2190.
- Jochum, J., C. Mears, S. Golwala, B. Sadoulet, J. P. Castle, M. F. Cunningham, O. B. Drury, M. Frank, S. E. Labov, F. P. Lipschultz, H. Netel, and B. Neuhauser, 1998, J. Appl. Phys. **83**, 3217.
- Johnson, J., 1928, Phys. Rev. **32**, 97.
- de Jong, M. J. M., and C. W. J. Beenakker, 1994, Phys. Rev. B **49**, 16070.
- de Jong, M. J. M., and C. W. J. Beenakker, 1995, Phys. Rev. Lett. **74**, 1657.
- Jönsson-Åkerman, B., R. Escudero, C. Leighton, S. Kim, I. K. Schuller, and D. A. Rabson, 2000, Appl. Phys. Lett. **77**, 1870.
- Kadlec, J., and K. H. Kadlec, 1975, Solid State Commun. **16**,

- 621.
- Kaganowicz, G., V. S. Ban, and J. W. Robinson, 1984, *J. Vac. Sci. Technol.* **A2**, 1233.
- Kajiyama, K., Y. Mizushima, and S. Sakata, 1973, *Appl. Phys. Lett.* **23**, 458.
- Kaminski, A., and L. I. Glazman, 2001, *Phys. Rev. Lett.* **86**, 2400.
- Kämper, K. P., W. Schmitt, G. Güntherodt, R. J. Gambino, and R. Ruf, 1987, *Phys. Rev. Lett.* **59**, 2788.
- Kapitulnik, A., 1992, *Appl. Phys. Lett.* **60**, 180.
- Kaplan, S. B., C. C. Chi, D. N. Langenberg, J. J. Chang, S. Jafarey, and D. J. Scalapino, 1976, *Phys. Rev. B* **14**, 4854.
- Karasik, B. S., B. Delaet, W. R. McGrath, J. Wei, M. E. Gershenson, and A. V. Sergeev, 2003, *IEEE Trans. Appl. Superc.* **13**, 188.
- Karvonen, J. T., L. J. Taskinen, and I. J. Maasilta, 2005, *Phys. Rev. B* **72**, 012302.
- Kastalsky, A., A. W. Kleinsasser, L. H. Greene, R. Bhat, F. P. Milliken, and J. P. Harbison, 1991, *Phys. Rev. Lett.* **67**, 3026.
- Kautz, R. L., G. Zimmerli, and J. M. Martinis, 1993, *J. Appl. Phys.* **73**, 2386.
- Kelley, R. L., M. D. Audley, K. R. Boyce, S. R. Breon, R. Fujimoto, K. C. Gendreau, S. S. Holt, Y. Ishisaki, D. McCammon, T. Mihara, K. Mitsuda, S. H. Moseley, *et al.*, 1999, in *EUV, X-Ray, and Gamma-Ray Instrumentation for Astronomy X*, edited by O. Siegmund and K. Flanagan (SPIE), volume 3765, pp. 114–127.
- Kendall, D. L., and R. A. Shultz, 1997, in *Handbook of Microlithography, Micromachining, and Microfabrication*, edited by P. Rai-Choudhury (SPIE Optical Engineering Press, Bellingham), volume 2, p. 41.
- Kenyon, M., 2005, Personal communication.
- Kern, D. P., P. J. Coane, P. J. Houzgo, and T. H. P. Chang, 1984, *Solid State Technol.* **22**, 87.
- Kindermann, M., and S. Pilgram, 2004, *Phys. Rev. B* **69**, 155334.
- Kittel, C., 1996, *Introduction to Solid State Physics*, 7th ed. (John Wiley & Sons, New York).
- Kivinen, P., A. Savin, M. Zgirski, P. Törmä, J. Pekola, M. Prunnila, and J. Ahopelto, 2003, *J. Appl. Phys.* **94**, 3201.
- Klitsner, T., and R. O. Pohl, 1987, *Phys. Rev. B* **36**, 6551.
- Knoedler, C., 1983, *J. Appl. Phys.* **54**, 2773.
- Kobayashi, K. I., T. Kimura, H. Sawada, K. Terakura, and Y. Tokura, 1998, *Nature* **395**, 677.
- Koga, T., S. B. Cronin, M. S. Dresselhaus, J. L. Liu, and K. L. Wang, 2000, *Appl. Phys. Lett.* **77**, 1490.
- Koga, T., X. Sun, S. B. Cronin, and M. S. Dresselhaus, 1998, *Appl. Phys. Lett.* **73**, 2950.
- Koga, T., X. Sun, S. B. Cronin, and M. S. Dresselhaus, 1999, *Appl. Phys. Lett.* **75**, 2438.
- Kogan, V. R., V. V. Pavlovskii, and A. F. Volkov, 2002, *Europhys. Lett.* **59**, 875.
- Korotkov, A. N., and K. K. Likharev, 1999, *Appl. Phys. Lett.* **75**, 2491.
- de Korte, P. A. J., J. Beyer, S. Deiker, G. C. Hilton, and K. D. Irwin, 2003, *Rev. Sci. Instrum.* **74**, 3807.
- Koyanagi, K., S. Kasai, and H. Hasegawa, 1993, *Jpn. J. Appl. Phys.* **32**, 502.
- Kroha, J., and A. Zawadowski, 2002, *Phys. Rev. Lett.* **88**, 176803.
- Kuhn, T., D. V. Anghel, J. P. Pekola, M. Manninen, and Y. M. Galperin, 2004, *Phys. Rev. B* **70**, 125425.
- Kulik, I. O., and A. N. Omel'yanchuk, 1978, *Sov. J. Low Temp. Phys.* **4**, 142.
- Kutchinsky, J., R. Taboryski, T. Clausen, C. B. Sorensen, A. Kristensen, P. E. Lindelof, J. Bindlev Hansen, C. Schelde Jacobsen, and J. L. Skov, 1997, *Phys. Rev. Lett.* **78**, 931.
- Kutchinsky, J., R. Taboryski, C. B. Sorensen, J. Bindlev Hansen, and P. E. Lindelof, 1999, *Phys. Rev. Lett.* **83**, 4856.
- Kuzmin, L., 2004, in *Astronomical Structures and Mechanisms Technology*, edited by J. Antebi and D. Lemke (SPIE), volume 5498, pp. 349–361.
- Kyser, D. F., 1983, *J. Vac. Sci. Technol. B* **1**, 1391.
- Kyser, D. F., and N. S. Viswanathan, 1975, *J. Vac. Sci. Technol.* **12**, 1305.
- Lamarre, J.-M., J. L. Puget, M. Piat, P. A. R. Ade, A. E. Lange, A. Benoit, P. De Bernardis, F. R. Bouchet, J. J. Bock, F. X. Desert, R. J. Emery, M. Giard, *et al.*, 2003, in *IR Space Telescopes and Instruments*, edited by J. C. Mather (SPIE), volume 4850, pp. 730–739.
- Lambe, J., and R. C. Jaklevic, 1969, *Phys. Rev. Lett.* **22**, 1371.
- Lambert, C. J., and R. Raimondi, 1998, *J. Phys.: Condens. Matter* **10**, 901.
- Landauer, R., 1957, *IBM J. Res.* **1**, 223.
- Lanting, T. M., H.-M. Cho, J. Clarke, W. L. Holzapfel, A. T. Lee, M. Lueker, and P. L. Richards, 2005, *Appl. Phys. Lett.* **86**, 112511.
- Lau, J. C., and R. V. Coleman, 1981, *Phys. Rev. B* **24**, 2985.
- Leivo, M. M., A. J. Manninen, and J. P. Pekola, 1997, *Appl. Supercond.* **7-12**, 227.
- Leivo, M. M., and J. P. Pekola, 1998, *Applied Physics Letters* **72**, 1305.
- Leivo, M. M., J. P. Pekola, and D. V. Averin, 1996, *Appl. Phys. Lett.* **68**, 1996.
- Leoni, R., G. Arena, M. G. Castellano, and G. Torrioli, 1999, *J. Appl. Phys.* **85**, 3877.
- Leoni, R., B. Buonomo, M. G. Castellano, F. Mattioli, D. Simeone, G. Torrioli, and P. Carelli, 2003, *J. Appl. Phys.* **93**, 3572.
- Levinson, H. J., and W. H. Arnold, 1997, in *Handbook of Microlithography, Micromachining, and Microfabrication*, edited by P. Rai-Choudhury (SPIE Optical Engineering Press, Bellingham), volume 1, p. 11.
- Likharev, K. K., 1979, *Rev. Mod. Phys.* **51**, 101.
- Lindell, A., J. Mattila, P. Deo, M. Manninen, and J. Pekola, 2000, *Physica B* **284-288**, 1884.
- van der Linden, P. J. E. M., and K. Behnia, 2004, *Rev. Sci. Instrum.* **75**, 273.
- Little, W. A., 1984, *Rev. Sci. Instrum.* **55**, 661.
- Liu, Y., Z. Zhang, J. Wang, P. P. Freitas, and J. L. Martins, 2003, *J. Appl. Phys.* **93**, 8385.
- Lounasmaa, O. V., 1974, *Experimental Principles and Methods Below 1 K* (Academic Press, London).
- Lusher, C. P., J. Li, V. A. Maidanov, M. E. Digby, H. Dyball, A. Casey, J. Nyeki, V. V. Dmitriev, B. P. Cowan, and J. Saunders, 2001, *Meas. Sci. Technol.* **12**, 1.
- Lüth, H., 2001, *Solid Surfaces, Interfaces, and Thin Films* (Springer, Berlin).
- Luukanen, A., K. M. Kinnunen, A. K. Nuottajarvi, H. F. C. Hoevers, W. M. B. Tiest, and J. P. Pekola, 2003, *Phys. Rev. Lett.* **90**, 238306.
- Luukanen, A., M. M. Leivo, J. K. Suoknuuti, A. J. Manninen, and J. P. Pekola, 2000, *J. Low Temp. Phys.* **120**, 281.

- Luukanen, A., A. Miller, and E. Grossman, 2005, in *Passive Millimeter-Wave Imaging Technology VIII*, edited by R. Appleby and D. A. Wikner (SPIE), volume 5789, in press.
- Luukanen, A., and J. P. Pekola, 2003, *Appl. Phys. Lett.* **82**, 3970.
- Madou, M., 1997, *Fundamentals of Microfabrication* (CRC Press, Boca Raton).
- Magnée, P. H. C., N. van der Post, P. H. M. Kooistra, B. J. van Wees, and T. M. Klapwijk, 1994, *Phys. Rev. B* **50**, 4594.
- Mahan, G. D., 1994, *J. Appl. Phys.* **76**, 4362.
- Mahan, G. D., and L. M. Woods, 1998, *Phys. Rev. Lett.* **80**, 4016.
- Maissel, L. I., and R. Glang, 1970, *Handbook of Thin Film Technology* (McGraw-Hill, New York).
- Mal'shukov, A. G., and K. A. Chao, 2001, *Phys. Rev. Lett.* **86**, 5570.
- Manninen, A. J., M. M. Leivo, and J. P. Pekola, 1997, *Applied Physics Letters* **70**, 1885.
- Manninen, A. J., J. K. Suoknuuti, M. M. Leivo, and J. P. Pekola, 1999, *Appl. Phys. Lett.* **74**, 3020.
- Marinelli, C., L. Sorba, M. Lazzarino, D. Kumar, E. Pelucchi, B. H. Müller, D. Orani, S. Rubini, A. Franciosi, S. De Franceschi, and F. Beltram, 2000, *J. Vac. Sci. Technol. B* **18**, 2119.
- Marnieros, S., L. Berge, A. Juillard, and L. Dumoulin, 1999, *Physica B* **259-261**, 862.
- Marnieros, S., L. Berge, A. Juillard, and L. Dumoulin, 2000, *Phys. Rev. Lett.* **84**, 2469.
- Mather, J. C., 1982, *Appl. Opt.* **21**, 1125.
- Matsuda, K., A. Kamijo, T. Mitsuzuka, and H. Tsuge, 1999, *J. Appl. Phys.* **85**, 5261.
- Mauskopf, P. D., J. J. Bock, H. D. Castillo, W. L. Holzapfel, and A. E. Lange, 1997, *Appl. Opt.* **36**, 765.
- Mazin, I. I., 1999, *Phys. Rev. Lett.* **83**, 1427.
- Mazin, I. I., 2000, *Appl. Phys. Lett.* **77**, 3000.
- McCord, M. A., and M. J. Rooks, 1997, in *Handbook of Microlithography, Micromachining, and Microfabrication*, edited by P. Rai-Choudhury (SPIE Optical Engineering Press, Bellingham), volume 1, p. 139.
- Mees, J., M. Nahum, and P. L. Richards, 1991, *Appl. Phys. Lett.* **59**, 2329.
- Melton, R. G., J. L. Paterson, and S. B. Kaplan, 1981, *Phys. Rev. B* **21**, 1858.
- Meschke, M., J. Pekola, and H. Godfrin, 2005, submitted.
- Meschke, M., J. P. Pekola, F. Gay, R. E. Rapp, and H. Godfrin, 2004, *J. Low Temp. Phys.* **134**, 1119.
- Miller, A., S. Nam, J. Martinis, and A. Sergienko, 2003, *Appl. Phys. Lett.* **83**, 791.
- Millman, J., and A. Grabel, 1987, *Microelectronics*, (McGraw-Hill International Editions, New York), second edition.
- Min, G., and D. M. Rowe, 2000, *Appl. Phys. Lett.* **77**, 860.
- Miner, A., A. Majumdar, and U. Ghoshal, 1999, *Appl. Phys. Lett.* **75**, 1176.
- Miyazaki, T., and N. Tezuka, 1995, *J. Magn. Magn. Mater.* **139**, L231.
- Mochel, M., C. Humphreys, J. Eades, J. Mochel, and A. Peturd, 1983, *Appl. Phys. Lett.* **42**, 38.
- Mönch, W., 1990, *Rep. Prog. Phys.* **53**, 221.
- Moodera, J. S., L. R. Kinder, T. M. Wong, and R. Meservey, 1995, *Phys. Rev. Lett.* **74**, 3273.
- Moreau, W. M., 1988, *Semiconductor Lithography: Principles, Practices, and Materials* (Plenum Press, New York).
- Morpurgo, A. F., T. M. Klapwijk, and B. J. van Wees, 1998, *Appl. Phys. Lett.* **72**, 966.
- Moseley, S., J. Mather, and D. McCammon, 1984, *J. Appl. Phys.* **56**, 1257.
- Moussy, N., H. Courtois, and B. Pannetier, 2001, *Rev. Sci. Instrum.* **72**, 128.
- Myers, M. J., W. Holzapfel, A. T. Lee, R. O'Brient, P. L. Richards, and H. T. Tran, 2005, *Appl. Phys. Lett.* **86**.
- Nagaev, K. E., 1992, *Phys. Lett. A* **169**, 103.
- Nagaev, K. E., 1995, *Phys. Rev. B* **52**, 4740.
- Nagaev, K. E., and M. Buttiker, 2001, *Phys. Rev. B* **63**, 081301.
- Nahum, M., T. M. Eiles, and J. M. Martinis, 1994, *Appl. Phys. Lett.* **65**, 3123.
- Nahum, M., and J. M. Martinis, 1993, *Appl. Phys. Lett.* **63**, 3075.
- Nahum, M., and J. M. Martinis, 1995, *Appl. Phys. Lett.* **66**, 3203.
- Nahum, M., J. M. Martinis, and S. Castles, 1993, *J. Low Temp. Phys.* **93**, 733.
- Nam, S., A. Miller, and D. Rosenberg, 2004, *Nucl. Instrum. Meth. Phys. Res. A* **520**, 523.
- NASA, 2005, Constellation-X, <http://constellation.gsfc.nasa.gov/>.
- Nazarov, Y. V., 1994, *Phys. Rev. Lett.* **73**, 134.
- Nazarov, Y. V., 1999, *Superlatt. Microstruct.* **25**, 1221.
- Nazarov, Y. V. (ed.), 2003, *Quantum Noise in Mesoscopic Systems* (Kluwer).
- Nazarov, Y. V., and D. A. Bagrets, 2002, *Phys. Rev. Lett.* **88**, 196801.
- Nazarov, Y. V., and T. H. Stoof, 1996, *Phys. Rev. Lett.* **76**, 823.
- Neikirk, D. P., W. W. Lam, and D. B. Rutledge, 1983, *Int. J. Infrared Milli.* **5**, 245.
- Neikirk, D. P., and D. B. Rutledge, 1984, *Appl. Phys. Lett.* **44**, 153.
- Neugebauer, C. A., and M. B. Webb, 1962, *J. Appl. Phys.* **33**, 74.
- Neurohr, K., T. Schäpers, J. Malindretos, S. Lachenmann, A. I. Braginski, H. Lüth, M. Behet, G. Borghs, and A. A. Golubov, 1999, *Phys. Rev. B* **59**, 11197.
- Nevirkovets, I. P., 1997, *Phys. Rev. B* **56**, 832.
- Nguyen, C., H. Kroemer, and E. L. Hu, 1992, *Phys. Rev. Lett.* **69**, 2847.
- Nguyen, V. S., 1988, in *Handbook of Thin-Film Deposition Processes, and Techniques*, edited by K. K. Schuegraf (Noyes Publications, Norwich), p. 112.
- Nguyen, V. S., P. Pan, and S. Burton, 1984, *J. Electrochem. Soc.* **131**, 2348.
- Nicollian, E. H., and J. R. Brews, 1983, *MOS Physics and Technology* (Wiley, New York).
- Nitta, J., T. Akazaki, and H. Takayanagi, 1994, *Phys. Rev. B* **49**, 3659.
- Nolas, G., J. Sharp, and H. Goldsmid, 2001, *Thermoelectrics: basic principles and new material developments.*, volume 45 of *Springer Series in Materials Science* (Springer, Berlin).
- Nolas, G. S., and H. J. Goldsmid, 1999, *J. Appl. Phys.* **85**, 4066.
- Nyquist, H., 1928, *Phys. Rev.* **32**, 110.
- Parker, J. S., S. M. Watts, P. G. Ivanov, and P. Xiong, 2002, *Phys. Rev. Lett.* **88**, 196601.
- Parkin, S. S. P., K. P. Roche, M. G. Samant, P. M. Rice, R. B. Beyers, R. E. Scheurlein, E. J. O'Sullivan, S. L. Brown,

- J. Bucchigano, D. W. Abraham, Y. Lu, M. Rooks, *et al.*, 1999, *J. Appl. Phys.* **85**, 5828.
- Parmenter, R. H., 1961, *Phys. Rev. Lett.* **7**, 274.
- Parsons, A., I. A. Sosnin, and V. T. Petrashov, 2003a, *Physica E* **18**, 316.
- Parsons, A., I. A. Sosnin, and V. T. Petrashov, 2003b, *Phys. Rev. B* **67**, 140502.
- Pekola, J., J. Suoknuuti, J. Kauppinen, M. Weiss, P. Linden, and A. Jansen, 2002, *J. Low Temp. Phys.* **128**, 263.
- Pekola, J. P., 2005, *Nature* **435**, 889.
- Pekola, J. P., D. V. Anghel, T. I. Suppula, J. K. Suoknuuti, A. J. Manninen, and M. Manninen, 2000a, *Appl. Phys. Lett.* **76**, 2782.
- Pekola, J. P., T. T. Heikkilä, A. M. Savin, J. T. Flyktman, F. Giazotto, and F. W. J. Hekking, 2004a, *Phys. Rev. Lett.* **92**, 056804.
- Pekola, J. P., K. P. Hirvi, J. P. Kauppinen, and M. A. Paalanen, 1994, *Phys. Rev. Lett.* **73**, 2903.
- Pekola, J. P., A. J. Manninen, M. M. Leivo, K. Arutyunov, J. K. Suoknuuti, T. I. Suppula, and B. Collaudin, 2000b, *Physica B* **280**, 485.
- Pekola, J. P., R. Schoelkopf, and J. N. Ullom, 2004b, *Phys. Today* **57**, 41.
- Pekola, J. P., J. J. Toppari, J. P. Kauppinen, K. M. Kinnunen, A. J. Manninen, and A. G. M. Jansen, 1998, *J. Appl. Phys.* **83**, 5582.
- Peltier, J., 1834, *Annales de chimie* **LVI**, 371.
- Phelan, P., V. Chiriach, and T.-Y. Lee, 2002, *IEEE Transactions on Components and Packaging Technologies* **25**, 356.
- Pierre, F., A. Anthore, H. Pothier, C. Urbina, and D. Esteve, 2001, *Phys. Rev. Lett.* **86**, 1078.
- Pierre, F., H. Pothier, D. Esteve, and M. H. Devoret, 2000, *J. Low Temp. Phys.* **118**, 437.
- Pistoletti, F., G. Bignon, and F. W. J. Hekking, 2004, *Phys. Rev. B* **69**, 214518.
- Plummer, J. D., M. D. Deal, and P. B. Griffin, 2000, *Silicon VLSI Technology* (Prentice Hall, New Jersey).
- Pobell, F., 1996, *Matter and Methods at Low Temperatures* (Springer, Berlin), 2nd edition.
- Poirier, W., D. Mailly, and M. Sanquer, 1997, *Phys. Rev. Lett.* **79**, 2105.
- Pothier, H., S. Guéron, N. O. Birge, D. Esteve, and M. H. Devoret, 1997a, *Z. Phys. B* **104**, 178.
- Pothier, H., S. Guéron, N. O. Birge, D. Esteve, and M. H. Devoret, 1997b, *Phys. Rev. Lett.* **79**, 3490.
- Pothier, H., S. Guéron, D. Esteve, and M. H. Devoret, 1994, *Phys. Rev. Lett.* **73**, 2488.
- Pruunila, M., J. Ahopelto, A. Savin, P. Kivinen, J. Pekola, and A. Manninen, 2002, *Physica E* **13**, 773.
- Pruunila, M., P. Kivinen, A. Savin, P. Torma, and J. Ahopelto, 2005, *Phys. Rev. Lett.* **95**, 206602.
- Purcell, S. T., V. T. Binh, N. Garcia, M. E. Lin, R. P. Andres, and R. Reif, 1994, *Phys. Rev. B* **49**, 17259.
- Quinn, T. J., 1983, *Temperature* (Academic Press, London).
- Rabson, D. A., B. J. Jönsson-Åkerman, A. H. Romero, R. Escudero, C. Leighton, S. Kim, and I. K. Schuller, 2001, *J. Appl. Phys.* **89**, 2786.
- Rammer, J., 1998, *Quantum transport theory* (Perseus books, Reading, Massachusetts).
- Rammer, J., and A. Schmid, 1986, *Phys. Rev. B* **34**, 1352.
- Rammer, J., and H. Smith, 1986, *Rev. Mod. Phys.* **58**, 323.
- Rego, L. G. C., and G. Kirczenow, 1998, *Phys. Rev. Lett.* **81**, 232.
- Reif, R., 1990, in *Handbook of Plasma Processing Technology*, edited by S. M. Rossnagel, J. J. Cuomo, and W. D. Westwood (Noyes Publications, Norwich), p. 260.
- Reintsema, C. D., J. Beyer, S. W. Nam, S. Deiker, G. C. Hilton, K. Irwin, J. Martinis, J. Ullom, and L. R. Vale, 2003, *Rev. Sci. Instrum.* **74**, 4500.
- Rhoderick, E. H., and R. H. Williams, 1988, *Metal-Semiconductor Contacts* (Oxford University, New York), 2 edition.
- Richards, P. L., 1994, *J. Appl. Phys.* **76**, 1.
- Richter, A., 2000, *Adv. Solid State Phys.* **40**, 321.
- Rollin, B. V., 1961, *Proc. Phys. Soc.* **77**, 1102.
- Rontani, M., and L. J. Sham, 2000, *Appl. Phys. Lett.* **77**, 3033.
- Rossnagel, S. M., 1998, in *Handbook of Vacuum Science and Technology*, edited by D. M. Hoffman, B. Singh, and J. H. Thomas III (Academic Press, San Diego), p. 609.
- Roukes, M. L., M. R. Freeman, R. S. Germain, R. C. Richardson, and M. B. Ketchen, 1985, *Phys. Rev. Lett.* **55**, 422.
- Rowe, D. M., and C. M. Bhandari, 1983, *Modern thermoelectrics* (Reston Publ. Co., Reston, VA), ISBN 0-8359-4593-6.
- Rowell, J. M., and D. C. Tsui, 1976, *Phys. Rev. B* **14**, 2456.
- Sales, B. C., 2002, *Science* **295**, 1248.
- Savin, A. M., and J. P. Pekola, 2005, unpublished.
- Savin, A. M., J. P. Pekola, J. T. Flyktman, A. Anthore, and F. Giazotto, 2004, *Appl. Phys. Lett.* **84**, 4179.
- Savin, A. M., M. Prunnila, J. Ahopelto, P. Kivinen, P. Törmä, and J. P. Pekola, 2003, *Physica B* **329-333**, 1481.
- Savin, A. M., M. Prunnila, P. P. Kivinen, J. P. Pekola, J. Ahopelto, and A. J. Manninen, 2001, *Appl. Phys. Lett.* **79**, 1471.
- Schönefeld, J., C. Enss, A. Fleischmann, J. Sollner, K. Horst, J. S. Adams, Y. H. Kim, G. M. Seidel, and S. R. Bandler, 2000, *Nuclear Instruments and Methods in Physics Research A* **444**, 211.
- Schäpers, T., V. A. Guzenko, R. P. Müller, A. A. Golubov, A. Brinkman, G. Crecelius, A. Kaluza, and H. Lüth, 2003a, *Phys. Rev. B* **67**, 014522.
- Schäpers, T., J. Malindretos, K. Neurohr, S. Lachenmann, A. van der Hart, G. Crecelius, H. Hardtdegen, H. Lüth, and A. A. Golubov, 1998, *Appl. Phys. Lett.* **73**, 2348.
- Schäpers, T., R. P. Müller, and A. Kaluza, 2003b, *Phys. Rev. B* **67**, 060502.
- Schep, K. M., and G. E. W. Bauer, 1997, *Phys. Rev. Lett.* **78**, 3015.
- Schmid, A., and G. Schön, 1975, *J. Low Temp. Phys.* **20**, 207.
- Schmidt, D. R., R. J. Schoelkopf, and A. N. Cleland, 2004a, *Phys. Rev. Lett.* **93**, 045901.
- Schmidt, D. R., C. S. Yung, and A. N. Cleland, 2003, *Appl. Phys. Lett.* **83**, 1002.
- Schmidt, D. R., C. S. Yung, and A. N. Cleland, 2004b, *Phys. Rev. B* **69**, 140301.
- Schottky, W., 1918, *Ann. Phys.* **57**, 541.
- Schottky, W., 1939, *Z. Physik* **113**, 367.
- Schwab, K., E. A. Henriksen, J. M. Worlock, and M. L. Roukes, 2000, *Nature* **404**, 974.
- Schwartz, K., 1986, *J. Phys. F* **16**, L211.
- Sergeev, A., and V. Mitin, 2000, *Phys. Rev. B* **61**, 6041.
- Sergeev, A., M. Y. Reizer, and V. Mitin, 2005, *Phys. Rev. Lett.* **94**, 136602.
- Seviour, R., and A. F. Volkov, 2000a, *Phys. Rev. B* **61**, R9273.
- Seviour, R., and A. F. Volkov, 2000b, *Phys. Rev. B* **62**, 6116.
- Shaikhaidarov, R., A. F. Volkov, H. Takayanagi, V. T. Petrashov, and P. Delsing, 2000, *Phys. Rev. B* **62**, R14649.

- Shakouri, A., and J. E. Bowers, 1997, *Appl. Phys. Lett.* **71**, 1234.
- Shakouri, A., C. LaBounty, J. Piprek, P. Abraham, and J. E. Bowers, 1999, *Appl. Phys. Lett.* **74**, 88.
- Shannon, J. M., 1976, *Solid State Electron.* **19**, 537.
- Simmons, J. G., 1963a, *J. Appl. Phys.* **34**, 1793.
- Simmons, J. G., 1963b, *J. Appl. Phys.* **35**, 2655.
- Singh, J., 1994, *Semiconductor Devices: An Introduction* (McGraw-Hill International Editions, New York).
- Smith, H., and H. H. Jensen, 1989, *Transport phenomena* (Oxford University Press, New York).
- Sofo, J. O., and G. D. Mahan, 1994, *Phys. Rev. B* **49**, 4565.
- Solymar, L., 1972, *Superconductive Tunneling, and Applications* (Wiley Interscience, New York).
- Spietz, L., K. W. Lehnert, I. Siddiqi, and R. J. Schoelkopf, 2003, *Science* **300**, 1929.
- Steinbach, A. H., J. M. Martinis, and M. H. Devoret, 1996, *Phys. Rev. Lett.* **76**, 3806.
- Stubbs, H. E., and R. G. Phillips, 1960, *Rev. Sci. Instrum.* **31**, 115.
- Sukhorukov, E. V., and D. Loss, 1999, *Phys. Rev. B* **59**, 13054.
- Sun, J. J., K. Shimazawa, N. Kasahara, K. Sato, S. Saruki, T. Kagami, O. Redon, S. Araki, H. Morita, and M. Matsuzaki, 2000, *Appl. Phys. Lett.* **76**, 2424.
- Sun, J. J., V. Soares, and P. P. Freitas, 1999, *Appl. Phys. Lett.* **74**, 448.
- Suoknuuti, J., J. Kauppinen, and J. Pekola, 2001, unpublished.
- Suzuki, K., J. Matsin, and T. Torikai, 1982, *J. Vac. Sci. Technol.* **20**, 191.
- Svidzinsky, A. A., 2002, *Phys. Rev. B* **65**, 144504.
- Swan, R. G. G., R. Mehta, and J. Cauge, 1967, *J. Electrochem. Soc.* **114**, 713.
- Sze, S. M., 1981, *Physics of Semiconductor Devices* (John Wiley & Sons, New York).
- Sze, S. M., 1985, *Semiconductor Devices: Physics, and Technology* (John Wiley & Sons, New York).
- Taboryski, R., T. Clausen, J. Bindslev Hansen, J. L. Skov, J. Kutchinsky, C. B. Sørensen, and P. E. Lindelof, 1996, *Appl. Phys. Lett.* **69**, 656.
- Tarasov, M. A., L. S. Kuzmin, M. Y. Fominskii, I. E. Agulo, and A. S. Kalabukhov, 2003, *JETP Lett.* **11**, 714.
- The European Space Agency, 2005, X-ray Evolving Universe Spectrometer, <http://www.rssd.esa.int/index.php?project=XEUS>.
- Thompson, L. F., C. G. Wilson, and M. J. Bowden, 1994, *Introduction to Microlithography* (American Chemical Society, Washington, DC).
- Thonhauser, T., G. D. Mahan, L. Zikatanov, and J. Roe, 2004, *Appl. Phys. Lett.* **85**, 3247.
- Timp, G., 1999, *Nanotechnology* (Springer, New York).
- Tinkham, M., 1996, *Introduction to Superconductivity* (McGraw-Hill, New York), 2nd edition.
- Tsuge, H., and T. Mitsuzuka, 1997, *Appl. Phys. Lett.* **71**, 3296.
- Ujsaghy, O., A. Jakovac, and A. Zawadowski, 2004, *Phys. Rev. Lett.* **93**, 256805.
- Ullom, J. N., W. B. Doriese, G. C. Hilton, J. A. Beall, S. Deiker, W. D. Duncan, L. Ferreira, K. D. Irwin, C. D. Reintsema, and L. R. Vale, 2004, *Appl. Phys. Lett.* **84**, 4206.
- Ullom, J. N., and P. A. Fisher, 2000, *Physica B* **284-8**, 2036.
- Upadhyay, S. K., A. Palanisami, R. N. Louie, and R. A. Buhrman, 1998, *Phys. Rev. Lett.* **81**, 3247.
- Usadel, K. D., 1970, *Phys. Rev. Lett.* **25**, 507.
- van den Berg, M. L., D. T. Chow, A. Loshak, M. F. Cunningham, T. W. Barbee, M. A. Frank, and S. E. Labov, 2000, in *X-Ray and Gamma-Ray Instrumentation for Astronomy XI*, edited by K. A. Flanagan and O. Siegmund (SPIE), volume 4140, pp. 436-444.
- Vavilov, M. G., L. I. Glazman, and A. I. Larkin, 2003, *Phys. Rev. B* **68**, 075119.
- Vinet, M., C. Chapelier, and F. Lefloch, 2001, *Phys. Rev. B* **63**, 165420.
- Virtanen, P., and T. T. Heikkilä, 2004a, *J. Low Temp. Phys.* **136**, 401.
- Virtanen, P., and T. T. Heikkilä, 2004b, *Phys. Rev. Lett.* **92**, 177004.
- Voellmer, G. M., C. A. Allen, M. J. Amato, S. R. Babu, A. E. Bartels, D. J. Benford, R. J. Derro, C. D. Dowell, D. A. Harper, M. D. Jhabvala, S. H. Moseley, T. Rennick, et al., 2003, in *Proceedings of the SPIE, Millimeter and Submillimeter Detectors for Astronomy*, edited by T. G. Phillips and J. Zmuidzinas (SPIE), volume 4855, pp. 63-72.
- Volkov, A. F., 1995, *Phys. Rev. Lett.* **74**, 4730.
- Volkov, A. F., and V. V. Pavlovskii, 1996, *JETP Lett.* **64**, 670.
- Volkov, A. F., and H. Takayanagi, 1997, *Phys. Rev. B* **56**, 11184.
- Voutilainen, J., T. T. Heikkilä, and N. B. Kopnin, 2005, *Phys. Rev. B* **72**, 054505.
- Vystavkin, A. N., D. V. Shuvaev, L. S. Kuzmin, and M. A. Tarasov, 1999, *JETP* **88**, 598.
- Wang, J., P. P. Freitas, E. Snoeck, X. Battle, and J. Cuadra, 2002, *J. Appl. Phys.* **91**, 7463.
- Wang, J., Y. Liu, P. P. Freitas, E. Snoeck, and J. Martins, 2003, *J. Appl. Phys.* **93**, 8367.
- Wasa, K., and S. Hayakawa, 1992, *Handbook of Sputter Deposition Technology* (Noyes Publications, Westwood).
- van Wees, B. J., K.-M. H. Lenssen, and C. J. P. M. Harmans, 1991, *Phys. Rev. B* **44**, 470.
- van Wees, B. J., P. de Vries, P. H. C. Magnee, and T. M. Klapwijk, 1992, *Phys. Rev. Lett.* **69**, 510.
- Weht, R., and W. E. Pickett, 1999, *Phys. Rev. B* **60**, 11006.
- Wellstood, F. C., C. Urbina, and J. Clarke, 1989, *Appl. Phys. Lett.* **54**, 2599.
- Wellstood, F. C., C. Urbina, and J. Clarke, 1994, *Phys. Rev. B* **49**, 5942.
- Wilhelm, F. K., G. Schön, and A. D. Zaikin, 1998, *Phys. Rev. Lett.* **81**, 1682.
- Wilhelm, F. K., A. D. Zaikin, and G. Schön, 1997, *J. Low Temp. Phys.* **106**, 305.
- Wilson, C. M., L. Frunzio, and D. E. Prober, 2001, *Phys. Rev. Lett.* **87**, 067004.
- Wollman, D. A., K. D. Irwin, G. C. Hilton, L. L. Dulcie, D. E. Newbury, and J. M. Martinis, 1997, *Journal of Microscopy* **188**, 196.
- Woodcraft, A. L., R. V. Sudiwala, E. Wakui, R. S. Bhatia, J. J. Bock, and A. D. Turner, 2000, *Physica B* **284-288**, 1968.
- Xiong, P., G. Xiao, and R. B. Laibowitz, 1993, *Phys. Rev. Lett.* **71**, 1907.
- Yip, S.-K., 1998, *Phys. Rev. B* **58**, 5803.
- Yoon, J., J. Clarke, J. M. Gildemeister, A. T. Lee, M. J. Myers, P. L. Richards, and J. T. Skidmore, 2001, *Appl. Phys. Lett.* **78**, 371.

- Yu, P. Y., and M. Cardona, 2001, *Fundamentals of Semiconductors* (Springer, Berlin).
- Zaikin, A. D., and G. F. Zharkov, 1981, Sov. J. Low Temp. Phys. **7**, 184.
- Zaitsev, A. V., 1992, JETP Lett. **55**, 45.
- Zeller, R. C., and R. O. Pohl, 1971, Phys. Rev. B **4**, 2029.
- Zhang, J., N. G. Anderson, and K. M. Lau, 2003, Appl. Phys. Lett. **83**, 374.
- Zhang, Z. G., P. P. Freitas, A. R. Ramos, N. P. Barradas, and J. C. Soares, 2001, Appl. Phys. Lett. **79**, 2219.
- Zhang, Z.-S., and D. A. Rabson, 2004, J. Appl. Phys. **95**, 557.
- Zhao, E., T. Lofwander, and J. A. Sauls, 2003, Phys. Rev. Lett. **91**, 077003.
- Zhao, E., T. Lofwander, and J. A. Sauls, 2004, Phys. Rev. B **69**, 134503.
- Zhou, R., D. Dagel, and Y. H. Lo, 1999, Appl. Phys. Lett. **74**, 1767.
- van der Ziel, A., 1986, *Noise in Solid State Devices and Circuits* (Wiley, NewYork).